The Dissertation Committee for Ariane Laura Beck
certifies that this is the approved version of the following dissertation:

Wide Band Gap Avalanche Photodiodes for Ultraviolet Single Photon Detection

Committee:

Joe C. Campbell, Supervisor

Archie Holmes, Jr.

Jack C. Lee

Lynn Loo

Dean P. Neikirk

Wide Band Gap Avalanche Photodiodes for Ultraviolet Single Photon Detection

by

Ariane Laura Beck, B.S.; M.S.

Dissertation

Presented to the Faculty of the Graduate School of

The University of Texas at Austin

In Partial Fulfillment

Of the Requirements

for the Degree of

Doctor of Philosophy

The University of Texas at Austin
May 2006

to eric

for his unconditional love and acceptance

for constantly renewing my faith in humanity

Acknowledgements

First, I must thank Dr. Joe Campbell for giving a freshman the chance to work in a graduate student lab. This early exposure to graduate school and the research environment gave me the experience and confidence that I needed to pursue graduate study. As a graduate student, I appreciate his high standards of excellence in research and the freedom and time to find my own way. I also very much appreciate his funding my undergraduate research assistants, who were a wonderful part of my graduate school experience.

I also must thank Dr. John Carrano. He was my mentor during my time as an undergraduate in Joe’s group. He trained me in clean room technique and taught me how to be a scientist. He trusted me with my own part of the project and stepped up my responsibilities as I grew as an engineer. The experience I gained from working with him has been invaluable to me.

I would like to thank my committee members Dr. Jack Lee, Dr. Archie Holmes, Jr., Dr. Dean Neikirk, and Dr. Lynn Loo. Dr. Lee has known me since my freshman year as an undergraduate. He helped me overcome test anxiety and prevented me from flunking the electronic circuits course. Without him, I would not be an engineer today. Dr. Holmes has been a constant source of support during my graduate studies. He has always been there to answer all of my questions and offer encouragement.

I would also like to thank Professor Jerry Woodall and his students at Yale for providing the concept and material for the GaP research.

Next, I must thank my group members. Shuling Wang and Gauri Karve have been wonderful friends. Shuling helped push me early on and stepped in as a senior

student when I didn’t have one. Gauri trained me in single photon counting measurements. I want to thank the other UV group members John Carrano, Ting Li, Bo Yang, Chuck Collins, Xiangyi Guo, and Handin Liu for all their hard work. I also want to thank the other members of Campbell’s group: Geoff Kinsey, Jeremy Schaub, Feng Ma, Xiaoguang Zheng, Ning Duan, Zhihong Huang, Ning Tan, Xiaowei Li, and Ning Li.

My undergraduate research assistants have been a wonderful part of my graduate school experience. I learned so much from teaching them and from trying to answer all of their questions. Their enthusiasm continually renewed my enthusiasm. They did excellent work and saved me a lot of time with their hard work processing devices in the clean room. Thanks to Aruna Ghatak-roy, Jennifer Ming, Charlie Kim, Helen Kim, and Renessa Kennelly.

The staff at MER has been absolutely wonderful. Terry Mattord has been a good friend, constantly encouraging, and always ready to help and offer any advice on how to make things to work. Carol Assadourian, Joyce Kokes, Amy Pinkston, and Jeannie Toll have been wonderful friends and so supportive and encouraging, in addition to their usual job functions. William Fordyce and James Hitzfelder have also been wonderfully encouraging and always ready to take my complaints on clean room safety issues. William (Jesse) James, Bill Ostler, Dean Zeeman, and Brenda Francis did/do a great job keeping the clean room up and running and are vitally important to all of us graduate students. I also want to thank Steve Moore and Cheryl Ragland in purchasing for always being so patient and quick to get the paperwork handled.

I want to thank Dr. John Cogdell. He was my undergraduate advisor and helped me get my undergraduate research assistantship in Joe’s group. I never took a class from him and yet his efforts have had such an impact on my academic career.

I want to thank the Women in Engineering Program at UT for all their amazing work. Tricia Berry, Danielle Seabold, Susan Masson, Katie Kizziar, and Sher Marie Croft, ya’ll are wonderful. I really appreciate all ya’lls hard work. The programs and seminars ya’ll have put together have been really helpful, and I have so enjoyed having the opportunity to work with future engineers. It’s been so much fun!

I have to thank Melanie Gullick in the Graduate Student Office. She works hard, is always ready to help (even when we students procrastinate), and always has a smile on her face.

Of course I must thank all of my professors and teachers along the way. Teachers seldom get the credit they deserve, so I'm going to list them here. My math and science teachers really made a difference: Ms. Moses (1st), Ms. Zucker (2nd), Ms. Jackson (3rd), Ms. Thompson (4th), Ms. Ellis (5th and 6th), Mr. Bullock (6th), Mrs. Bond (7th), Ms. Powers (7th), Mr. Menaugh (8th), Ms. Beaman (8th), Mr. Snow (9th), Ms. Stohlman (9th), Ms. Sula (10th), Mr. Armenta (10th and 11th), Mr. Ortman (12th), and Mr. Wentz (11th and 12th). And yes that was from memory.

I knew I wanted to be a scientist early on, but it takes a lot of people to prepare one for such a task and keep them from getting distracted along the way. I want to thank all of these math and science teachers for preparing me, believing in me, and encouraging me. I especially want to thank Mr. Wentz who taught me Physics, AP Chem., and science research. I also want to thank Ms. Henderson (12th, mentorship) and my mentor T.K. Lewis. The experience I got in that class directly led to my undergraduate research experience, which has meant so much. I also must thank Mrs. Carden, my eighth grade history teacher. She is an incredible human being who always went the extra mile with every student. She took the time to get to know each and every one of us and made sure all of us at every ability level experienced success and self worth. And a big thanks to my English teachers at Blue Valley Northwest HS: Ms. Brecheisen (9th), Ms. Thompson (10th), Mr. Pribyl (11th), and Ms. Paugh (12th). They were tough, but they taught us to write, edit, and organize our thoughts in order to make an argument. They produced better writers than most colleges. This dissertation surely would not have been what it is without them.

Of course, I have to thank my family. Daddy, thank you for your love of science and your unceasing persistence. Mommy, thank you for the academic ability, love of reading, and curiosity about nearly everything. Thank you for teaching me to think logically and throwing me in the pool every summer to teach me not to quit. Ali, thanks for being my sister and always bragging about me (even though you called me a geek).

Eric, thanks for being you, loving me, and supporting me through the PhD process with enduring patience. Spouses should get a diploma too. Thanks for editing my dissertation and keeping me calm and focused throughout the process.

Wide Band Gap Avalanche Photodiodes for Ultraviolet Single Photon Detection

Publication No._______

Ariane Laura Beck, Ph.D.
The University of Texas at Austin, 2006

Supervisor: Joe C. Campbell

Avalanche photodiodes (APDs) suitable for detecting ultra-weak signals in biological agent detection and non-line-of-sight communication require single photon detection. GaP APDs were the first devices studied in the pursuit of that goal, followed by SiC APDs.

Both p-i-n, recessed window p-i-n, and Schottky GaP structures were implemented using thin device layers. The results showed sub-picoamp dark current, UV photoresponse, and high gains. The peak quantum efficiency at 440nm indicated Γ-valley absorption, and the Schottky device confirmed UV detection enhancement. These results indicated that GaP APDs could achieve strong photoresponse below 290nm; however, SiC APDs outperformed GaP APDs in every area.

Linear-mode characterization of 4H-SiC APDs demonstrated sub-picoamp unity-gain dark current and high gains ($>10^6$) for p-n junction and p-i-n structures, which included 260nm i-region and 480nm i-region structures. Fabrication and characterization techniques were discussed and included beveled edge formation and two-dimensional raster scan measurements of gain uniformity. Raster scans of the mesa area revealed edge breakdown, contact field crowding, and material non-uniformity. A sidewall bevel angle $<10^\circ$ suppressed edge breakdown, and a ring contact geometry alleviated contact field crowding. Decreasing the device diameter diminished non-uniformity resulting from doping density variations in the p-n junction structure.

A room temperature set-up was established for gated and passive quenching of single photon counting APDs. Functionality and selection of the gate capacitance, transient canceling cables, and average photon number were discussed.

Improved gain uniformity allowed the first successful demonstration of gated quenching single photon counting SiC APDs. The peak single photon detection efficiency (SPDE) at 325nm was 6.9%. The SPDE was 3.2% at a 13MHz dark count rate.

Both p-i-n structures attained a dark count rate of 24-28kHz at 3% SPDE and 325nm, which was a three order reduction in dark count rate compared to p-n junction devices at the same SPDE. Gated quenching of the 260nm i-region APD achieved detection efficiencies greater than 9%. Smaller diameter p-i-n devices experienced increased spatial non-uniformity that resulted in higher dark count rates and lower detection efficiencies. Additionally, passive quenching measurements of a 260nm i-region APD indicated potential for high SPDE at 266nm in SiC APDs.

Table of Contents

List of Tables

List of Figures

Chapter 1
Introduction

1.1 Motivation

Detection of ultraviolet (UV) wavelengths is important in medical, military, and environmental applications, including biological agent detection and non-line-of-sight (NLOS) communications.[1-2] Our primary focus is providing compact, rugged, and inexpensive UV detectors for biological agent detection and NLOS communication systems. Currently, these systems use photomultiplier tubes (PMTs), but their cost, size, and fragility are not suitable for large volume field deployment. However, semiconductor technologies can meet all of these requirements.

The primary requirements for UV detector performance in these systems are low dark current, high gain, and solar-blind operation. The low dark current and high gain are essential for detecting the weak signals, often on the order of a few photons, in both of these systems. Solar-blind operation requires a cut-off in detection for wavelengths longer than 290nm. This is called solar-blind because atmospheric absorption attenuates solar radiation below 290nm by six orders of magnitude. Thus, a detector that can only see wavelengths shorter than 290nm is blind to solar radiation. This characteristic is particularly important for NLOS communications, since a low solar background is essential for achieving a high signal-to-noise-ratio.

1.2 Applications

1.2.1 Biological Agent Detection

Biological agent detection systems utilize the fluorescence of biological compounds to determine the presence of biological agents. This type of system is called detect-to-warn since it is only capable of determining the presence of a biological agent, but not identifying specific agents. The components of the system include a chamber that traps a sample of air, a UV laser (266nm emission) that excites the sample, and three photodetectors, as shown in Figure 1.1. The first detector collects UV (300-400nm) signals primarily from tryptophan fluorescence, the second detects visible (400–600nm) fluorescence from NADH and flavin compounds, and the third senses scattered light from the 266nm excitation wavelength. Each of these detectors must detect only in the specified range, in order to avoid overlap that would obscure the collected data. Our research focus is on the third detector, which must operate as "solar-blind." Though the detectors in this system are not usually exposed to sun-light, the spectral response must not overlap with the spectral response of the 300-400nm detector.[1]

Low light level scattering from biological agents requires sensitive devices with high gain, in order to be "seen" by the readout circuitry. Use in the field requires small, rugged devices. Additionally, the elimination of filters and large power supplies required by PMTs will reduce both cost and size.

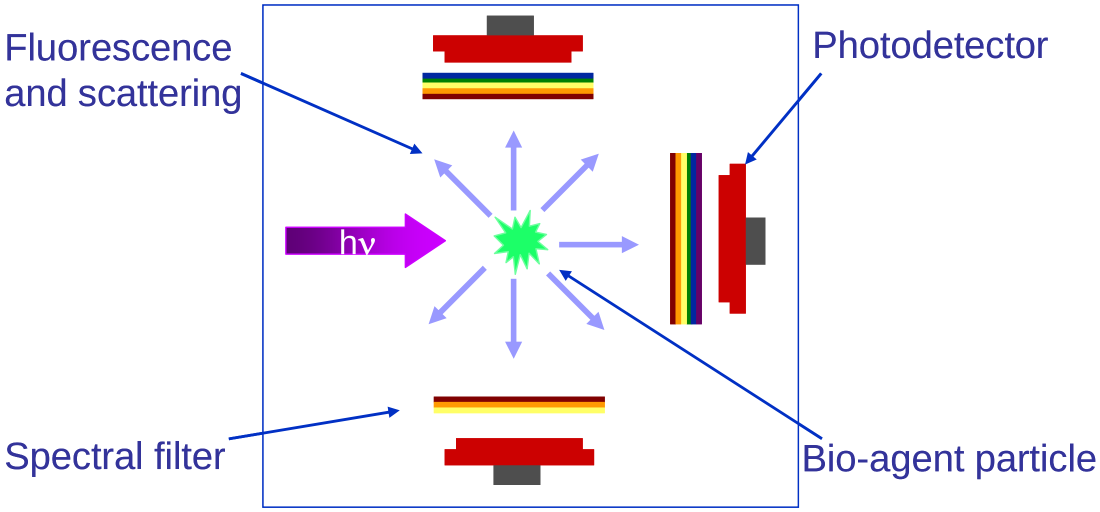

Figure 1.1 Schematic of detect-to-warn biological agent detection system.

1.2.2 Non-Line-of-Sight Communication

Non-line-of-sight communication exploits molecular, or Rayleigh, scattering in order to provide both transmission and extinction of the communication signal. Typical extinction lengths are approximately 1km, which reduces the likelihood of eavesdroppers. A transmitter emits a UV signal that scatters outward from the transmitter producing a cone shaped area with carriers of the communication signal, as shown in Figure 1.2. A receiver, with a wide field of view, has a cone shaped area of reception. If the transmitter and receiver are placed within a few hundred meters of each other, the cones will overlap. This allows the transmitter and receiver to "see" each other without being placed in direct alignment. This type of technology is very valuable for short-range covert field operations in urban environments or wooded areas where line-of-sight communication is impractical. By operating in the deep UV, the communications links are able to reduce solar background radiation. Currently, the system uses multi-channel plate (MCP)

PMTs, which provide a large active area and low dark count rate (<10Hz). Thus, the development of arrays with low dark count rates will be essential for replacing PMTs in this application.

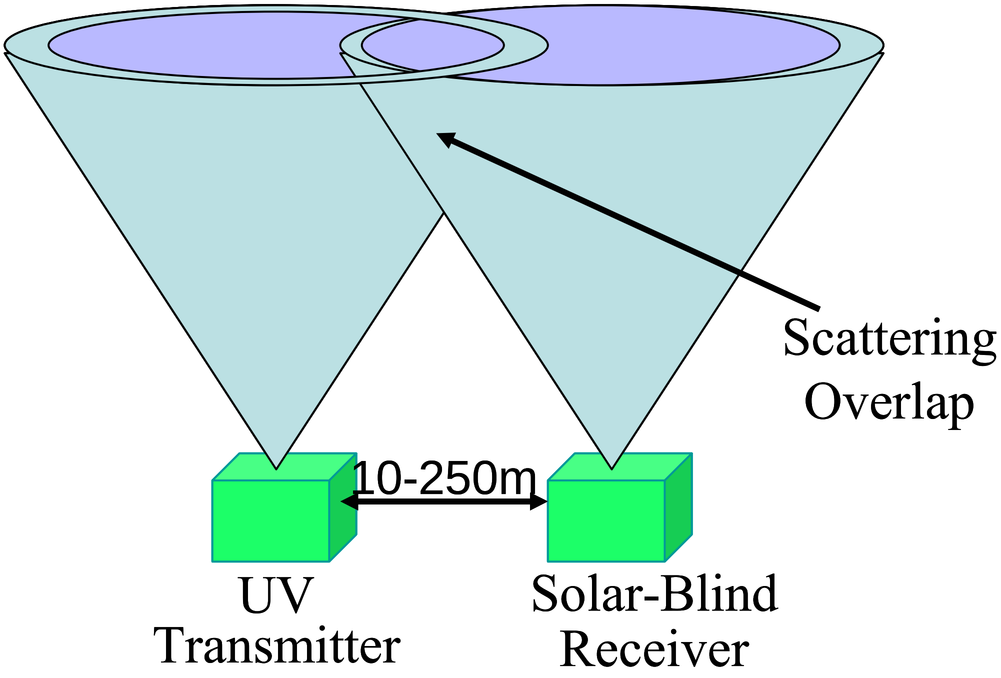

Figure 1.2 Schematic of non-line-of-sight communication link.

1.3 Candidates

Currently, photomultiplier tubes are used in both of the above systems due to their high responsivity, high internal gain ($>10^6$), low dark current, low dark count rate (10-100Hz), and large detection area. However, they are large and fragile, require high bias voltages, and have only 10% quantum efficiency (QE) in the UV. Additionally, expensive filters are required to block out the broadband response of PMTs, which further reduce the QE. Semiconductor technologies satisfy the requirements of small, rugged, and inexpensive, as well as having a lower voltage requirement. However, the dark current and dark count rates are much higher, and the gain and QE requirements are met to varying degrees by the four main semiconductor candidates, which include UV-enhanced Si, AlGaN/GaN, GaP, and SiC photodiodes.

UV-enhanced Si avalanche photodiodes (APDs) are a contender on account of their mature material system, easy integration, and low cost. Additionally, Si has a low impact ionization ratio, which is an indicator of strong single photon counting performance.[3] Higher dark currents (nA) require either cooling or a very small device active area in order to achieve low dark count rates. Si detectors demonstrated dark count levels of 200Hz at room temperature, but the active area was only 10μm in diameter.[4,5] Additionally, Si APDs require expensive filters to operate as solar-blind detectors, due to their high visible response, that reduce the UV efficiency. Si photodetectors have only demonstrated photon counting operation down to 400nm.[6]

AlGaN/GaN devices are very attractive for 266nm applications, due to their solar-blind cutoff (<290nm), but high defect densities ($\sim 10^9 cm^{-2}$), localized microplasma breakdown, and premature edge breakdown preclude avalanche gain.[7-9] In AlGaN photodiodes, the aluminum ratio can be tailored such that the spectral response is solar-blind without incorporating filters.[10] This a very valuable characteristic since it reduces both system cost and complexity. Unfortunately, AlGaN APDs do not exist, and there have been only three reports of GaN APDs.[7-9] McIntosh et al. characterized these GaN APDs as single photon detectors at 325nm and achieved a 13.5% single photon detection efficiency (SPDE) at a 400kHz dark count rate for a 37μm-diameter APD.[9,11] However, this is the only report of GaN Geiger-mode APDs, presumably due to low yield and poor stability. Thus, we shifted our attention to GaP which has low dark current, reasonable dark count rates (<100kHz)[12], high yield, and low cost.

GaP is rarely looked at for UV photodetection due to its indirect band gap of 2.26eV (550nm).[13,14] However, GaP has much higher absorption coefficients at shorter wavelengths.[15] This attribute can be exploited by using absorption layers thinner than the absorption length necessary for photoresponse at longer wavelengths, corresponding to the indirect band gap. This allows the Γ−valley energy gap of 2.78eV (445nm) to dominate the photoresponse, creating a quasi-direct band gap semiconductor. Additionally, GaP has low cost and high yield, which makes arrays for NLOS communication feasible. But as the reader will see (Chapter 4), the strong response at visible wavelengths, particularly the peak response at 440nm, will require filters for UV operation. These filters also attenuate the UV response, which is already low, making these devices more useful for applications in the 400-500nm range. Consequently, we began investigating SiC APDs, which have a peak QE at least two times that of our best GaP devices in the UV.

Silicon carbide has many advantageous material qualities for realizing high gain, low noise, and low dark current UV APDs, including a wide band gap, a low impact-ionization-coefficient ratio ($\alpha/\beta \sim 0.1$), and high quantum efficiency.[15-17] 4H-SiC has a band gap of 3.2eV, which results in visible-blind (λ<400nm) performance and a three order rejection ratio of visible to UV light.[18] Since both biological agent detection and non-line-of-site communication require high sensitivities at extremely low intensities, on the order of single to tens of photons, efforts began to achieve single photon detection using SiC APDs. Models of avalanche probability indicate that SiC APDs have potential to outperform Si detectors[19], and low dark current levels indicate potential for low dark count rates. The downside of SiC is that the cost is much higher and the material quality is poorer than Si. SiC material quality has achieved thickness uniformity of approximately 1% and doping uniformity of 6-10%, which generates spatial gain non-uniformity, particularly at high breakdown fields.[20-21] Recent reports of SiC single photon counting APDs have low detection efficiencies (1-3%) and high dark count rates (650kHz – 14MHz).[22-23] However, the study of SiC single photon counting APDs is in its infancy and has much potential.

1.4 Organization

The focus of my research began as a search for a high gain and low dark current linear-mode APD. As the project progressed, the focus moved to UV single photon detection using APDs in Geiger-mode. Chapter 1 seeks to explain the motivation and applications for this focus, as well as provide a succinct discussion of the technologies available to satisfy these requirements. Chapter 2 briefly discusses the impact ionization mechanism in linear-mode APDs and how it relates to Geiger-mode performance. Chapter 3 reviews the basics of passive and gated quenching Geiger-mode measurement techniques. Chapter 4 takes a short reprieve from photon counting to show the results of the GaP APD study. Chapter 5 reviews processing and characterization techniques used for 4H-SiC photodiodes and includes the linear-mode characterization of 4H-SiC p-n junction and p-i-n APDs. Chapter 6 examines the gain non-uniformity resulting from edge breakdown, contact field crowding, and material variation in 4H-SiC APDs using a two-dimensional raster scan technique. Chapter 7 presents the initial results on p-n junction APDs as Geiger-mode single photon counting detectors, and Chapter 8 investigates performance improvements attained by using p-i-n APDs for single photon counting. Chapter 9 summarizes the results of this dissertation research and lists suggestions for the continued study of single photon counting SiC APDs.

Chapter 2
Avalanche Photodiodes in Geiger-Mode

In order to understand the operation of avalanche photodiodes in Geiger-mode, the linear-mode behavior and the avalanche process must be discussed. The basic structure of a p-i-n homojunction photodiode is shown in Figure 2.1. Absorption of incident photons can occur in one of three regions of this device structure, which generates electron-hole pairs as shown in the band diagram in Figure 2.1. When absorption occurs in the neutral p- and n- regions minority carriers are generated and must diffuse to the i-region in order to contribute to the photocurrent, since the electric field in the neutral regions is small. Both electrons and holes generated in the i-region contribute to the photocurrent, due to the electric field.

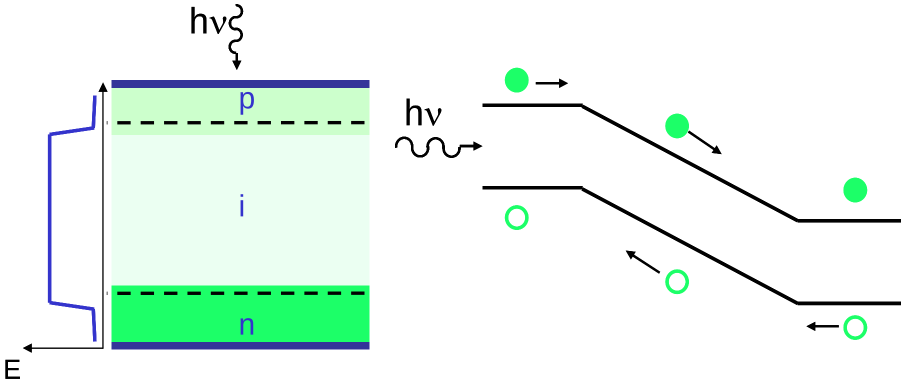

Figure 2.1 (a) Device layer structure with corresponding electric field. The dashed lines represent the depletion width extension into the p- and n- regions. (b) Band diagram representing the current contribution from photoabsorption of incident carriers in the three device layers.

2.1 Linear-mode

As the reverse bias across the p-i-n diode is increased, the field strength in the i-region increases and energizes the carriers. Eventually the carrier energy reaches the threshold energy, E_{th}, for impact ionization. Carriers having energy near threshold can impact a valence band electron giving up energy to excite the valence band electron to the conduction band. This impact ionization process generates a secondary electron-hole pair. The original carrier and the secondary electron and hole travel in the high field, eventually reaching the threshold energy, impact ionizing, and generating more electron-hole pairs as illustrated in Figure 2.2. This process of impact ionization generates multiple electron-hole pairs, creating an avalanche of carriers. Photodiodes that operate at fields greater than the threshold field achieve internal gain, called multiplication gain, and are known as avalanche photodiodes or APDs.[1]

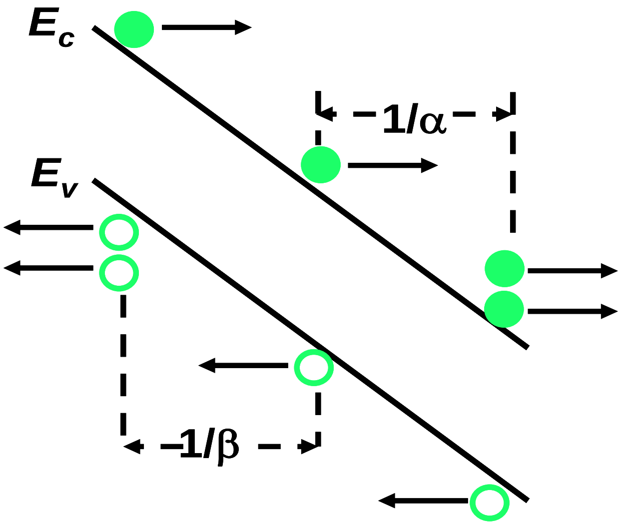

Figure 2.2 Band diagram of the i-region of an APD under high reverse bias illustrating the impact ionization process.

Important parameters for characterizing the avalanche process include α, β, and their ratio k. The average distance a carrier must travel to gain the energy necessary for impact ionization is 1/α for electrons and 1/β for holes. The excess noise of an APD originates from the statistical nature of impact ionization events. The ratio of ionization coefficients for electrons and holes strongly influences the excess noise factor, F(M), where M is the multiplication gain. The ratio k=β/α should be minimized for electron-initiated gain and maximized for hole-initiated gain. This is because the avalanche process is more deterministic and faster for a single-carrier type, or single-carrier injection, which leads to lower noise and higher speed APDs.[2-3] Figure 2.3(a) shows the progression of the avalanche process for single-carrier injection, while Figure 2.3(b) shows the development of an avalanche in which both carriers contribute to the gain through impact ionization. The single-carrier avalanche is a parallel process and grows

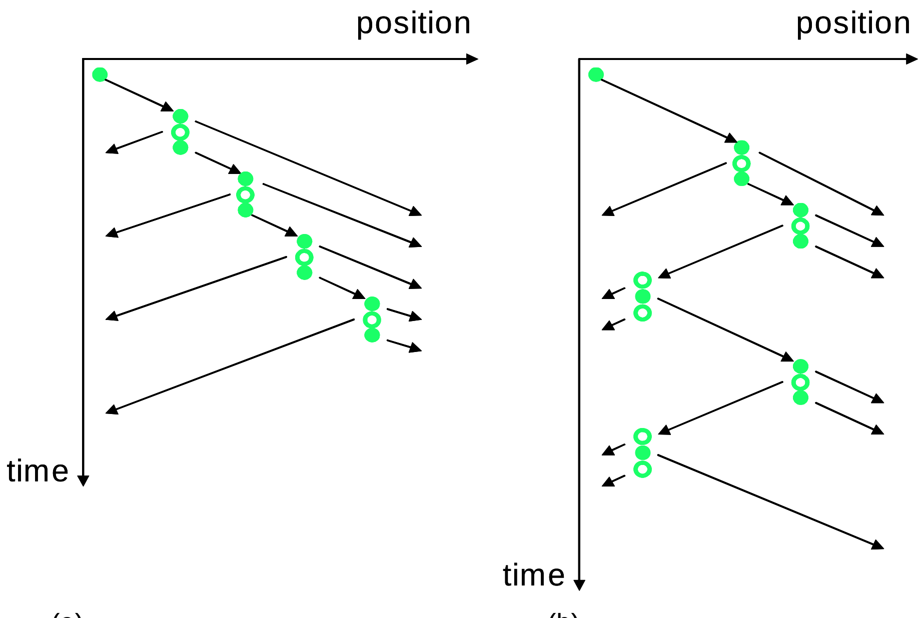

(a) (b)

Figure 2.3 (a) Single-carrier avalanche and (b) mixed-carrier avalanche.

much more quickly than the mixed-carrier avalanche that must travel back and forth across the high field region. In this situation, one carrier failing to impact ionize can terminate the avalanche or significantly alter the gain.[4]

2.2 Geiger-mode

As the APD bias voltage continues to increase, the field will surpass the breakdown field, which can produce a self-sustaining avalanche. Any carrier injected into the high field region has a certain probability (called the avalanche or breakdown probability) of generating a self-sustaining avalanche pulse. Figure 2.4 show the current-voltage characteristic of an APD biased above the breakdown voltage. Any carrier entering the high field region, photo-generated or dark, can produce a steady-state current. In the absence of a carrier, or if the carrier fails to initiate a self-sustaining pulse, the current stays low. This mode of operation is known as Geiger-mode, due to similarities with Geiger-Muller counters, and allows the APD to behave as a bi-stable device. Since the avalanche response in Geiger-mode is self-sustaining, a single photon can initiate an avalanche that grows to a detectable level.

Just as quantum efficiency and dark current are important performance metrics for linear-mode APDs, single photon detection efficiency and dark count probability are important metrics for Geiger-mode APDs. The single photon detection efficiency (SPDE) is the product of the unity-gain external quantum efficiency (η) and the avalanche probability. The avalanche probability is dependent on a number of parameters

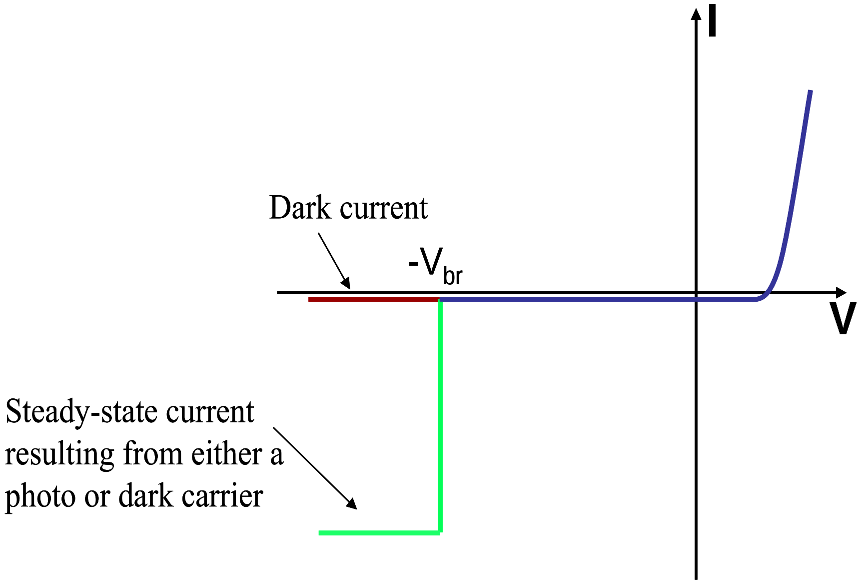

Figure 2.4 IV characteristic of an APD operating in Geiger-mode.

including the excess bias, ionization coefficients (α and β), k, carrier generation location, and the thickness of the active region. The excess voltage is the difference between the applied voltage and the breakdown voltage and is often represented as the excess bias ratio ($\Delta V/V_{Br}$). A sharp increase in the avalanche probability as a function of excess bias ratio is preferable, since this will lead to a sharper increase in the SPDE with voltage.[5-6]

In general, a low value of k indicates a steeper rise in avalanche probability with excess bias ratio, due to the benefits of single-carrier injection discussed above and illustrated in Figure 2.3(a). However, Ng et al.[7] modeled the rise in the avalanche probability as function of excess voltage and determined that SiC has a steeper rise than Si, despite Si having a lower k. They found that this resulted from the steeper rise of the impact ionization coefficients with field strength. Additionally, they established that materials with low k values have a slower rise in the avalanche probability with excess bias voltage under mixed-carrier injection conditions.

Wang et al.[6] determined that the avalanche probability for photo-generated carriers is also affected by the carrier generation location. Under single-carrier injection, minority carriers generated within a diffusion length of the active region have the highest avalanche probability, though the probability differs for hole and electron avalanche probabilities according to their impact ionization coefficients. Additionally, structures designed with a thicker i-region have higher avalanche probabilities, due to an increased number of higher order avalanche events.

The dark count probability is a function of both the avalanche probability and the number of dark carriers present during the detection time. Thus, the number of dark carriers will increase with avalanche probability, which increases with the excess voltage. Additionally, any multiplied dark current in the active region during the time the applied voltage is above the breakdown voltage can give rise to a self-sustaining avalanche event. The avalanche pulses resulting from dark carriers cannot be differentiated from avalanche pulses resulting from photo-generated carriers. Furthermore, once a self- sustaining avalanche has begun, no other carriers can be detected until the avalanche is quenched. Thus, the dark current must be minimized.

2.3 Conclusion

The basic principles governing the behavior of avalanche photodetectors have been addressed. Concepts linking the processes of avalanche gain to Geiger-mode operation were also discussed. Geiger-mode was established as the bi-stable operation of an APD. The parameters affecting the avalanche probability were outlined, including the effects of excess bias, ionization coefficients (α and β), k, carrier generation location, and the thickness of the active region. The connections between the basic linear-mode parameters were related to their Geiger-mode counterparts.

Chapter 3
Single Photon Counting Measurements

Avalanche photodiodes can operate as single photon counting avalanche photodiodes (SPADs) using a number of measurement techniques. In Geiger-mode operation, the APD must be brought above the device breakdown voltage, so that the avalanche probability is greater than zero. Any carrier, either photo-generated or dark, that enters the high field region of the device can generate a self-sustaining avalanche pulse with a probability equal to the avalanche probability corresponding to the bias voltage. The self-sustaining avalanche pulse continues until quenched, i.e. the bias voltage drops below the breakdown voltage.

The three most common quenching techniques are active, passive, and gated. Cova et al. developed active quenching, which utilizes feedback circuitry to improve the timing response of the SPAD.[1]

In passive quenching an APD is dc biased above the breakdown voltage. A large load resistor quenches the avalanche pulse in response to the high current level of the pulse and resets the SPAD bias. This is the simplest scheme and will be discussed in the next section. Alternatively, in gated passive quenching the device is dc biased below the breakdown voltage and an ac pulse biases the APD above the breakdown voltage. This technique has the advantage of limiting the time that the device is biased above breakdown, which reduces both the opportunity for dark carriers to initiate an avalanche pulse and the stress on the device caused by continuously maintaining a high field. In this case, the falling edge of the ac pulse quenches the avalanche. Section 3.2 will discuss gated quenching in more detail.

3.1 Passive Quenching

The set-up requirements for passive quenching are the simplest of the above-mentioned techniques. A dc bias, V_{DC}, is applied to the device through a large load resistor, R_L, as shown in Figure 3.1. The APD output is measured across a 50Ω resistor, R_s, and collected by a comparator. The discriminator threshold set by the comparator determines if the output of the APD constitutes an avalanche pulse. Figure 3.1 shows an example of the APD output and the resulting comparator output for a given discriminator threshold.

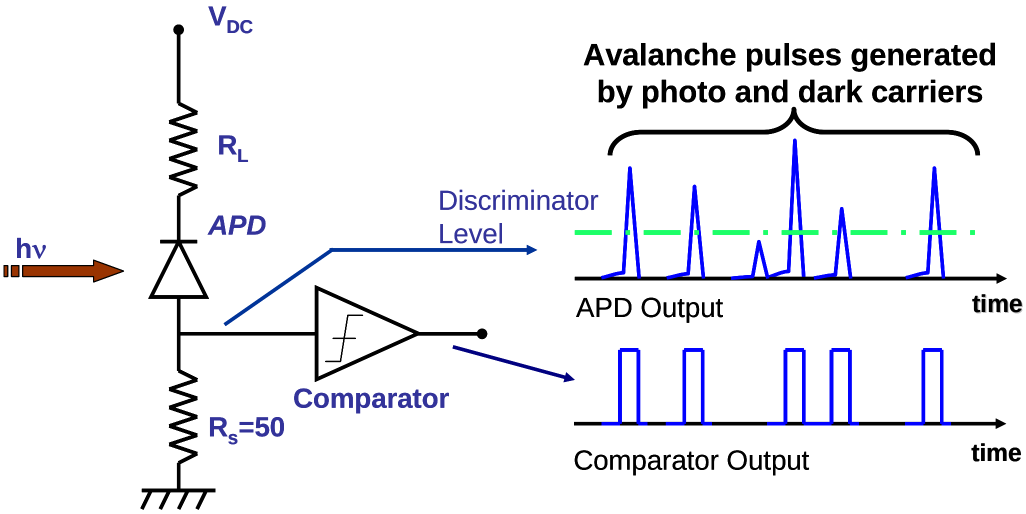

Figure 3.1 Circuit diagram for passive quenching, along with APD and comparator output.

In the case of an avalanche event, a current, I_D, will flow through the APD, which will increase the voltage drop across the load by $I_D \cdot R_L$. The dc bias across the APD will drop by the same voltage, thus the load resistor must be large enough to induce a voltage drop sufficient to bring the APD bias below breakdown and quench the avalanche pulse. The APD bias will then recover to the V_{DC} level, or recharge, with a time constant equal to the product of the load resistor and the sum of the device capacitance and stray capacitance, which is typically on the order of microseconds. Since the APD is biased well above the breakdown voltage, it is possible that the APD will trigger again after the bias voltage reaches the breakdown voltage level, but before it recovers to the original V_{DC} level. Since the avalanche probability increases with excess bias (Chapter 2) the probability that a carrier will trigger another avalanche before the voltage fully recovers increases as the bias voltage approaches V_{DC}. Because these subsequent pulses tend to be smaller, they are less likely to trigger an avalanche. They can, however, restart the voltage recovery time. Both of these effects of subsequent pulses reduce the photon detection efficiency, thus a quick recharge time is favorable for passive quenching.

Related to this phenomenon is the dead time, which is the time during which the device cannot detect a carrier. A carrier cannot be detected if it arrives during the avalanche pulse of a previous carrier or if it arrives too early during the recharge time. Thus the dead time is dependent on both the recharge time and the discriminator threshold level, and limits the maximum count rate. Gated quenching eliminates this problem, since the falling edge of the ac pulse acts to quench the avalanche event, rather than a resistor, and there is no recharge time.

3.2 Gated Quenching

In gated quenching, the APD is dc biased below the breakdown voltage, and an ac bias pulse brings the total APD bias above the breakdown voltage. The falling edge of the ac pulse quenches the avalanche pulse. The pulse length only needs to be long enough to allow the avalanche pulse to reach the discriminator level. Thus, increasing the device speed reduces the necessary ac pulse duration, which should also reduce the dark count rate, since the multiplied dark current in the device will be minimized. Additionally, the ac pulse off-time can be set to allow traps to empty, in order to mitigate afterpulsing.[1] For a short ac pulse width, on the order of a few nanoseconds, only one carrier per ac pulse can trigger an avalanche event, thus the maximum count rate is the repetition rate of the ac bias.

Figure 3.2 shows a block diagram of the apparatus that was used to take the measurements. The set-up was a room temperature variation on the set-up designed by Gauri Karve.[2] The dc bias is applied across a load resistor R_L, while the ac bias is applied through the gate capacitor, C_g (Section 3.2.1). The output pulse of the APD drops across 50Ω to the photon counter, which contains the detection gate and the discriminator, and outputs the resulting number of counts, N_D. The dark count probability for the gated quenching set-up can be calculated as

$$P_D = \frac{N_D}{f \cdot t} \tag{3.1}$$

where N_D is the total number of dark counts per measurment, f is the repition rate of the ac and gate pulses, and t is the integration time, which is typically one second. The dark count rate can be calculated by dividing the dark probability by the gate length, yielding the number of dark counts per one second. The total count rate can be similarly calaculated, by repeating the measurements with the laser shutter open and replacing P_D and N_D in (3.1) with the total count probability P_T and the total number of counts N_T. Thus the total number of the counts and total count probability include both photo and dark counts. The experimental single photon detection efficiency, SPDE, is related to the dark count and total count probabilities according to[2-3]

$$\text{SPDE} = \left(\frac{1}{n}\right)\cdot\ln\left(\frac{1 - P_D}{1 - P_T}\right) \tag{3.2}$$

From (3.2), SPDE is maximized when P_D is minimized and P_T is maximized. The detection gate, which is synchronized to the ac pulse via an external trigger, should be as long as or longer than the ac pulse, in order to maximize the total counts. Ideally, a photon source with an external trigger would be used, such that the ac pulse, detection gate, and photon arrival time could all be synchronized, as shown in Figure 3.3. Unfortunately, short pulse width, low power UV lasers operating below 350nm are not widely available. Those that are, do not have an external trigger feature. The set-up in Figure 3.2 utilizes a HeCd cw laser. The photon number for a cw laser is calibrated to the average number of photons per gate, instead of the average number of photons per pulse. Additionally, a cw laser cannot be synchronized to the ac bias, so some photon detection efficiency will be lost due to photons that arrive shortly before the ac pulse, after the ac

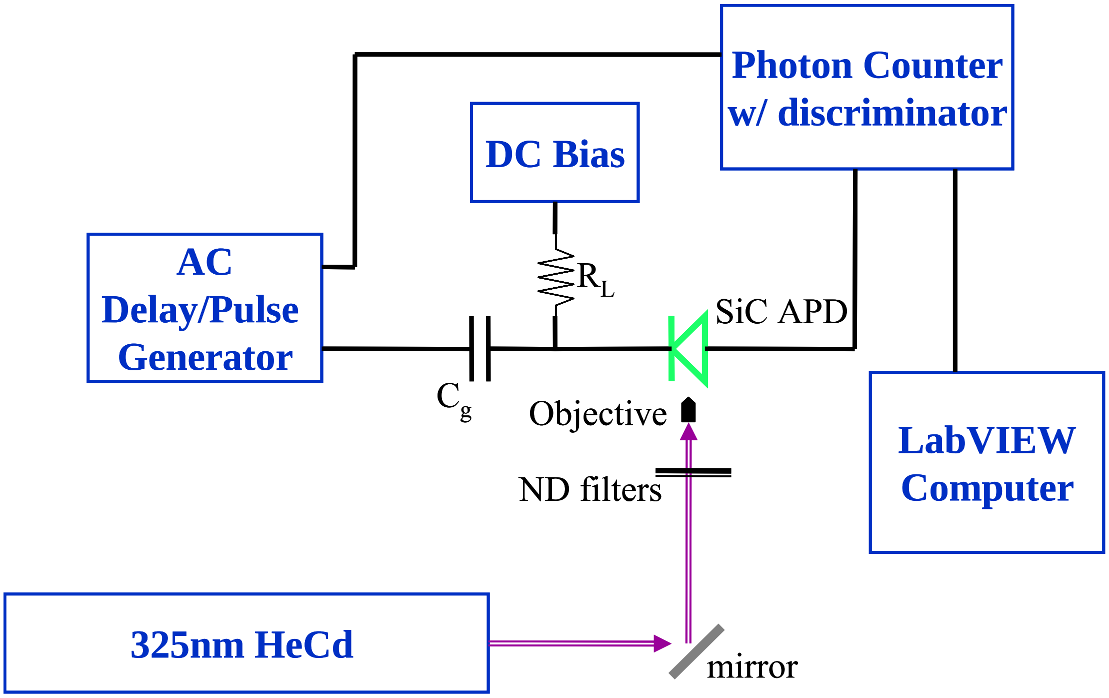

Figure 3.2 Block diagram of gated quenching single photon counting apparatus.

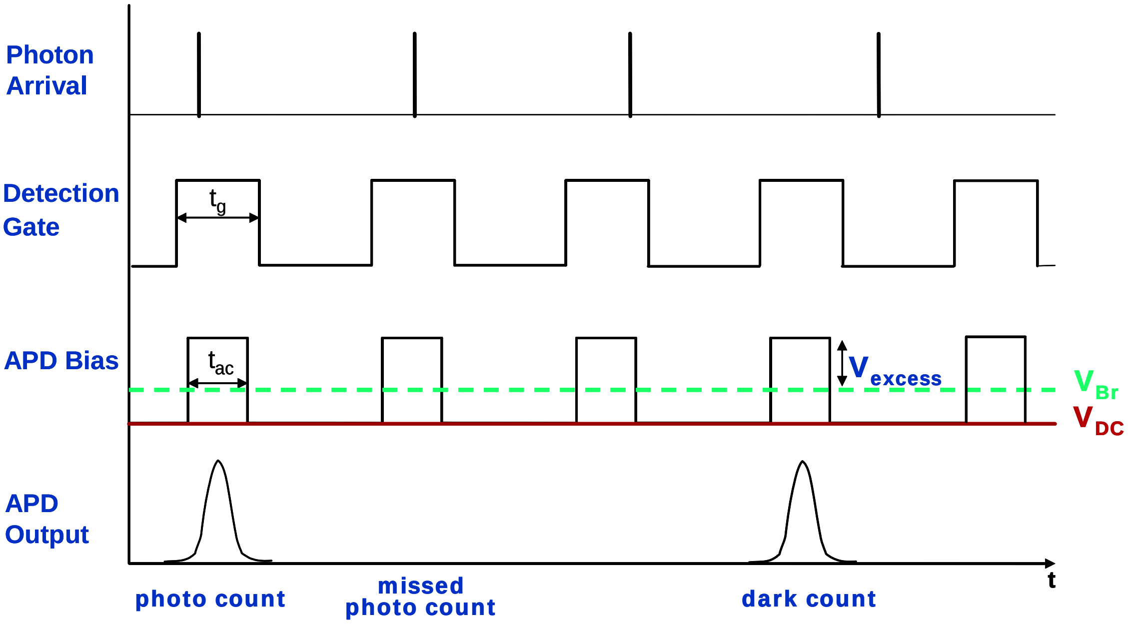

Figure 3.3 Timing diagram of gated quenching experiment that shows the arrival time of photons with the detection gate and bias pulse and the resulting APD output. Scenarios for photo count, dark count, and missed count are also shown.

pulse, or too late during the ac pulse to generate an avalanche pulse greater than the discriminator threshold.

The two configurations shown in Figure 3.4 used a 266nm Nd:YAG laser with a 7.5kHz repetition rate. Both set-ups used a 50/50 beam splitter at the source, with one beam going to the SiC APD under test and the other to a Si photodetector. The output of the Si detector triggered the ac pulse generator, which then triggered the photon counter. The cable delays and the pulse generator and photon counter insertion delays introduce an approximately 35-40ns lag between the optical and electrical paths. This leaves the two choices shown in Figure 3.4: either delay the bias pulse until there is another laser pulse or delay the laser pulse from reaching the APD until the first triggered bias pulse arrives.

Delaying the ac pulse for one cycle of the laser output required a 133μs delay in the electrical path, corresponding to the 7.5kHz repetition rate of the laser, as shown in Figure 3.4(a). However, the delay generator triggered with the Si detector could only produce a 129μs delay, such that the next trigger pulse did not arrive before the previous pulse fired. Thus a 3μs passive delay in conjunction with the cable delay provided the additional 4μs. Since the first triggered ac pulse was delayed until the second laser pulse, any discrepancy in the laser repetition rate propagated throughout the measurement. The ensuing mismatch in the synchronization of the ac pulse, detection gate, and photon arrival resulted in poor performance.

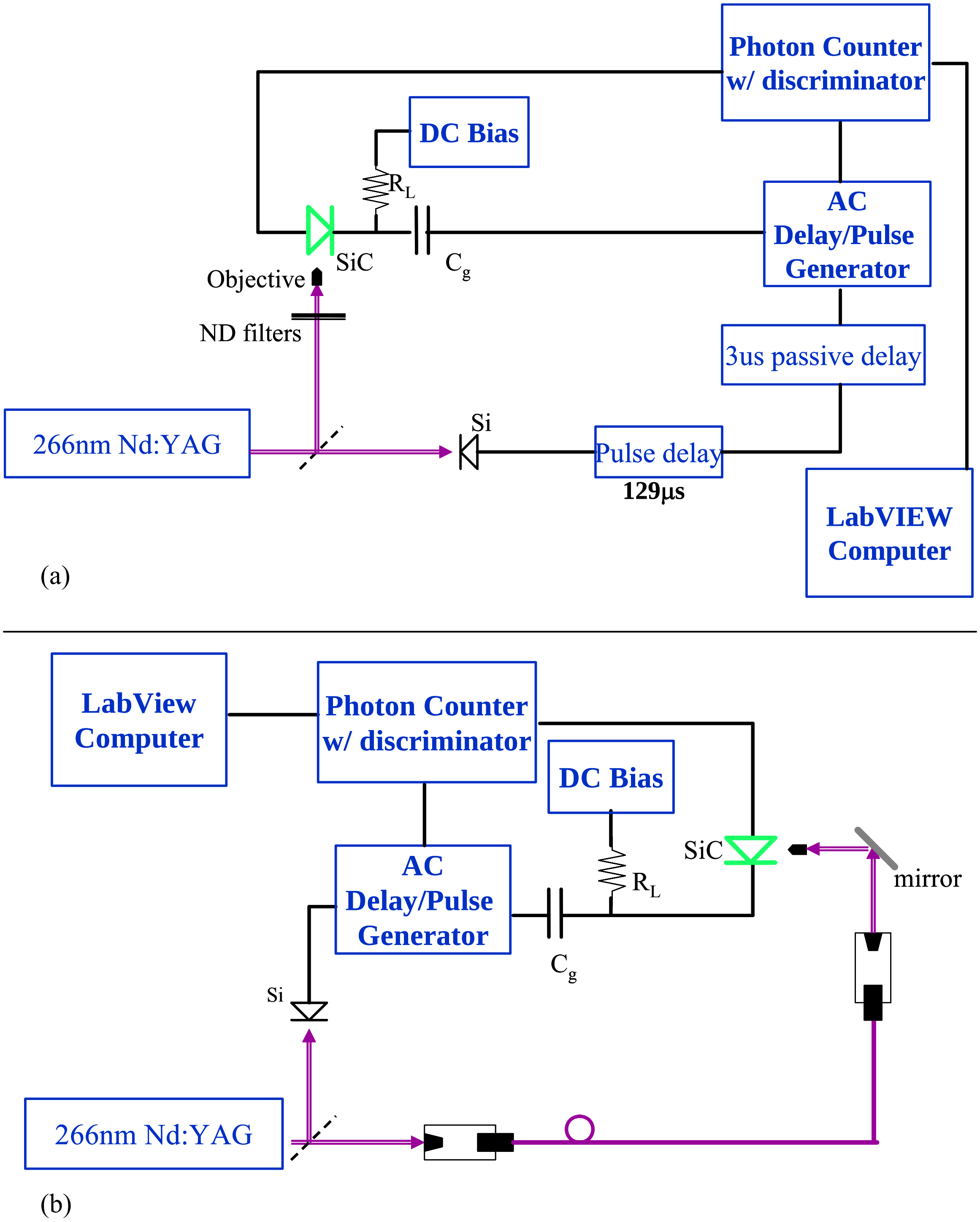

Figure 3.4 Block diagram of the (a) ac pulse delayed and the (b) laser pulse delayed set-up for a 266nm laser.

The second solution used a long optical fiber in order to delay the laser pulse until the ac pulse had time to reach the APD and trigger the detection gate, as shown in Figure 3.4(b). In order to delay the optical signal, approximately 9 meters of fiber were used. However, losses due to free-space-fiber coupling, fiber-to-fiber coupling, and attenuation of UV light through the fiber resulted in a pulse power too low for beam alignment to the device. Thus, the 266nm laser was only successfully used in passive quenching measurements.

3.2.1 Selecting C_g

The dc bias is applied across a load resistor R_L, while the ac bias is applied through the gate capacitor, C_g. Ideally, the total bias across the APD is $V_{DC} + V_{AC}$, and the excess bias, $V_E = V_{DC} + V_{AC} - V_{Br}$. However, this is only the case if the value of the gate capacitor is selected to maximize the actual applied voltage, V_a, according to the capacitive voltage divider.

$$V_a = V_{AC} \cdot \frac{C_g}{C_g + C_d + C_s} \tag{3.3}$$

where C_d is the device junction capacitance, and C_s is the stray capacitance. Typically, the sum $C_d + C_s$ is approximately 10pF, thus a gate capacitance greater than 10nF will drop more than 99.9% of the pulse height across the APD. Cova et al. discuss the distortion of the circuitry on the pulse shape in detail in Reference [1].

Initial measurements were taken using a 100nF capacitor to ensure that the ac pulse reached full height. However, the unity-gain dark current in the APD IV characteristics increased by two orders of magnitude. This was determined to result from the leakage current of the capacitor through a ground loop created by the transient canceling cables (Section 3.2.2). Figure 3.5 shows the leakage current of four different capacitors. The 100nF, 4.7nF, and 470pF capacitors all had 50V rating. The 560pF capacitor had a 500V rating and was selected on the assumption that a capacitor with a higher dc voltage rating would have a lower leakage current. From (3.3), approximately 98% of the ac pulse height should drop across the diode when either the 470pF or 560pF capacitors are used. The leakage current of both of these capacitors is comparable to the leakage current of a typical SiC APD.

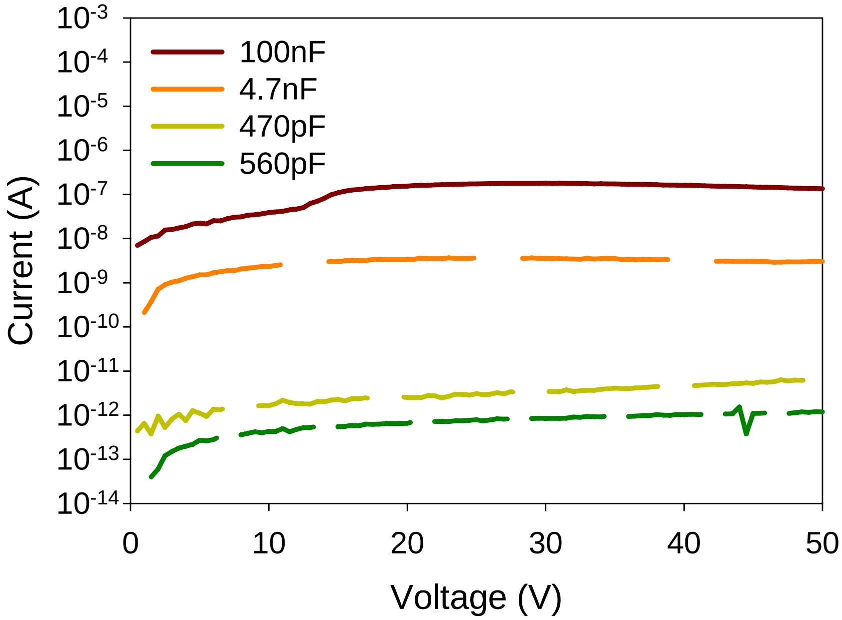

Figure 3.5 Capacitance leakage current for 100nF, 4.7nF, 470pF, and 560pF capacitors.

3.2.2 Transient Canceling Cables

The fast rise and fall time of the ac bias pulse generates capacitive transient behavior at the APD output, which obscures the avalanche signal pulse. Bethune et al.

developed a transient canceling technique using matched cables at the ac input and the APD output, as shown in Figure 3.6(a).[4] The cable at the ac pulse input is shorted, so that the signal reflected through the cable is inverted and delayed by the round trip transit time. The cable at the output is left open, so that the signal reflection is noninverted and delayed by the round trip transit time of the cable. The cables are connected using SMA T-connectors. If the cables are matched, the inverted and noninverted pulses cancel leaving only the signal, as illustrated in the timing diagram in Figure 3.6(b).

The applied ac voltage splits at node 1. One part of the signal travels to the APD, referred to as split 1, while the other travels down the shorted cable, referred to as split 2. Split 1 travels to the APD, which generates a signal consisting of the transient and the avalanche pulse. When that signal arrives at node 2, it splits again. Part of the pulse arrives at the output at time t = 0, as shown on the "AC split 1" line in Figure 3.6(b), while the other part of the pulse travels down the open cable. This part is reflected and arrives at the output with time delay T, which is the round trip travel time of the cables. Both of these signals carry both the transient and the avalanche pulse and appear on the AC split 1 line.

Split 2 travels down the shorted cable and arrives at the APD inverted with delay T. Split 2 contains no avalanche pulse response, since it is inverted and takes the APD further below breakdown. However, it generates a capacitive transient, and the signal splits at node 2. The first part of the signal arrives at the output with no further delay, while the second part travels down the open cable. This portion of the signal finally arrives at the output with a delay of 2T, as shown on the "AC split 2" line in Figure 3.6(b). When the two portions of the signal are put back together, the noninverted and inverted transient signals both arriving at time T cancel out, leaving only the avalanche signal portion of the noninverted signal at time T. The noninverted transient at time t = 0 and the inverted transient at 2T are ignored since the detection gate is synchronized to the signal at T.

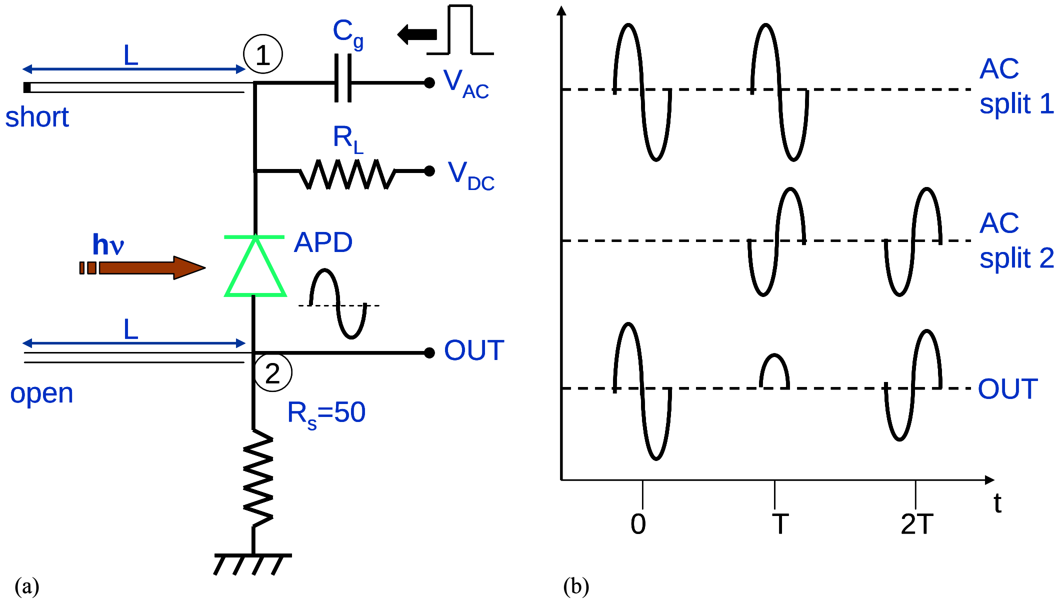

(a) (b)

Figure 3.6 (a) Gated quenching circuit with capacitive transient canceling cables and (b) timing diagram of the resulting ac signals, where t is the round trip travel time through a cable of length L.

In Figure 3.7, the detection gate scan from time t = 0 to time 2T shows the signal that passes the discriminator threshold as a function of time. The scan confirms the presence of the transients and the center avalanche response, and reveals two additional peripheral peaks at t = 10ns and t = 35ns. These pulses result from ringing in the capacitive transient and the reflection of that ringing with a delay equal to the round trip travel time of the open cable. Figure 3.8(a) shows the capacitive transient in a SiC APD without the transient canceling cables, where the peak separation was approximately 10ns. Figure 3.8(b) shows the result of implementing the transient canceling cable technique using cables with a 24ns round trip transit time for a total of 48ns between the transients. The 50ns spread in the transients results from the inverted pulse triggering on the rising edge. The cable length was chosen such that the signal peak in the center would be sufficiently delayed from the peripheral peak at t = 10ns.

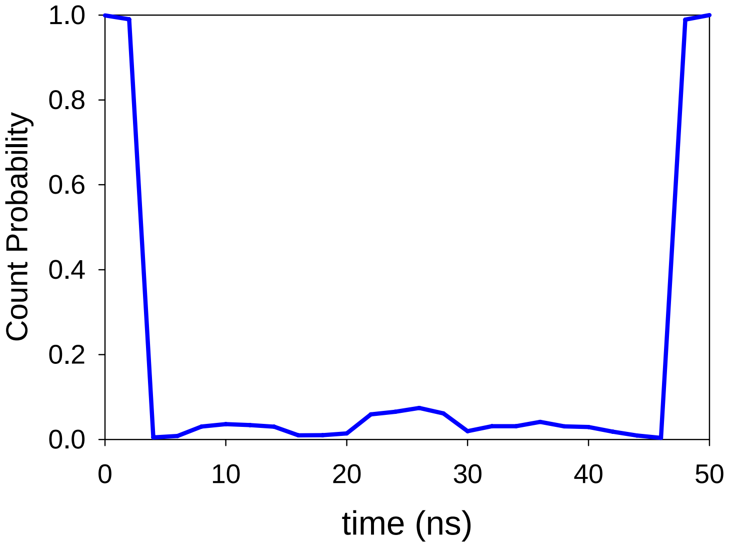

Figure 3.7 Detection gate scan showing capacitive transients at t = 0 and t = 50. The avalanche pulse is in the center at t = 0.

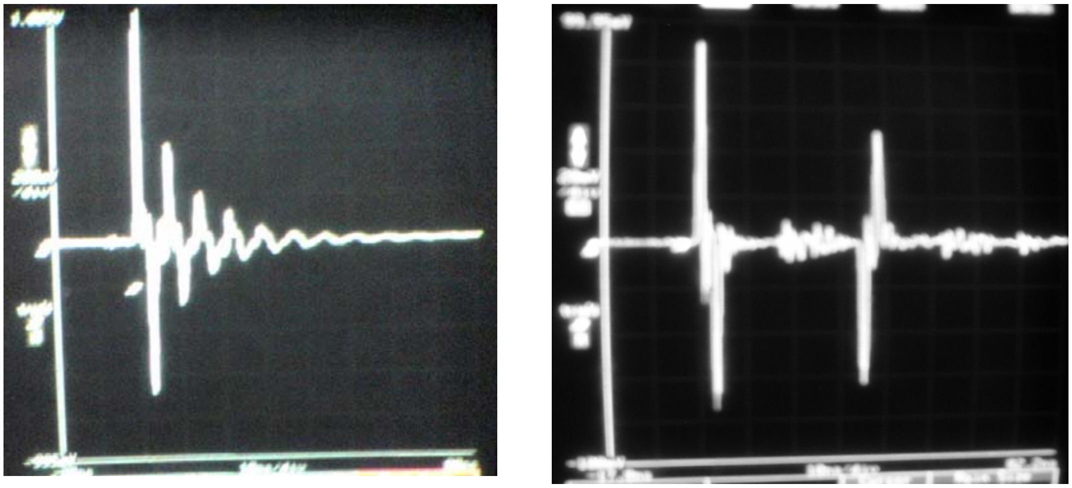
(a)
(b)

Figure 3.8 (a) Capacitive transient in a SiC APD without the transient canceling cables and (b) the signal resulting from implementing the transient canceling cable technique.

3.2.3 Average Photon Number

The distribution of photons in a laser pulse is Poissonian, thus each photon is random and independent of the others.[5] At the single photon level, this beam must be attenuated to a level below one photon per pulse, or one photon per gate pulse for a continuous source. The average number of photons per pulse is nbar. Thus, if nbar = 0.1, there is a 10% probability that a given pulse contains a photon. So, if the repetition rate, f, of the ac pulse is 10kHz, a one second integration time allows for maximum of 10^4 photon counts. However, nbar only represents the average number, thus there is a certain probability that more than one photon will arrive during a single pulse. Figure 3.9 shows the probability that a pulse will contain a certain number of photons for a given average photon number, following Poisson statistics. If the average photon number per pulse is 1, there is a 10% likelihood that three photons will arrive during a single pulse. Therefore, in order to adhere to a rigorous definition of single photon counting the average photon number must be kept less than 1 photon per pulse.

The average number of photons reaching the detector in a single pulse can be calculated according to:

$$\bar{n} = \frac{P_d}{h \cdot \nu \cdot f} \tag{3.4}$$

where P_d is the optical power reaching the APD, h is Plank’s constant, υ is the optical frequency, and f is the laser repetition rate. For a cw laser, f is the reciprocal of the gate width. The optical power P_d can be calculated by dividing the photocurrent by the responsivity at the optical wavelength and accounting for the attenuation of the optical filters.

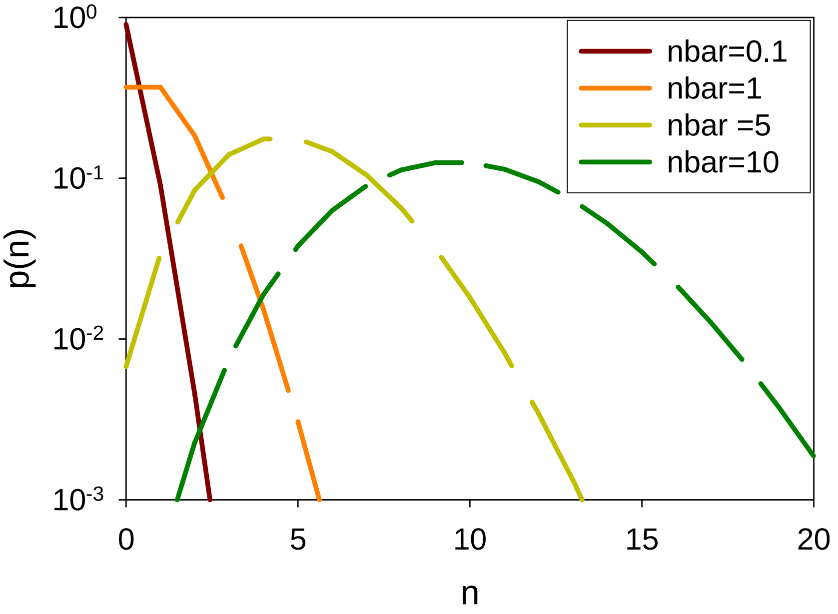

Figure 3.9 Poissonian statistics showing the probability that a pulse will contain a certain number of photons for given average photon number.

3.3 Conclusion

Techniques for both passive and gated passive quenching were discussed, including the role of the bias circuitry. The set-ups described here used both pulsed and cw laser sources. Pulsed sources in general are preferable, since the photon arrival can be synchronized with the ac bias and detection gate. However, this option is not yet available for low power UV lasers, with a short pulse width and kHz level repetition rate, thus the 266nm laser is best used in passive quenching.

Functionality and selection of the gate capacitance, transient canceling cable length, and average photon number were also discussed. Both the gate capacitance and cable length should be selected to suit the device parameters, including junction capacitance, leakage current, and transient response.

Chapter 4
Gallium Phosphide Photodetectors

Gallium phosphide (GaP), though most commonly used in emitters, has potential for use in both ultraviolet and blue light detection applications from 250nm to 500nm. The primary application for which these devices were investigated was biological agent detection, which requires three different detector wavelength ranges. The first collects UV signals primarily from tryptophan (~330nm); the second detects visible (400–600nm) fluorescence from NADH and flavin compounds; and the third senses scattered light at the excitation wavelength (266nm).[1]

As discussed in Chapter 1, photomultiplier tubes (PMTs) currently fill this niche, but they are less than ideal for portable, rugged systems. The first semiconductor material system we researched for this application was GaN/AlGaN.[2-4] Because it is a ternary compound semiconductor, the absorption characteristics and cutoff wavelength of AlGaN can be tailored to the desired solar-blind wavelength range. However, due to the high defect densities ($\sim 10^9 cm^{-2}$), GaN/AlGaN devices often exhibited catastrophic premature microplasma breakdown, prompting us to change course and investigate GaP photodetectors. SiC devices, with a visible-blind cutoff (<380nm), have achieved low noise and high gain, but their high cost and high breakdown field ($\sim 4x10^6 V/cm$)[5] justify the study of GaP devices. Chronologically, this research precedes our SiC research, thus I will save comparisons in favor of SiC detectors for the concluding remarks of this chapter.

GaP has an indirect band gap of 2.26eV, corresponding to a wavelength of 550nm, thus it is often overlooked for UV applications. However, GaP has much higher absorption coefficients at shorter wavelengths.[6] This attribute can be exploited by using absorption layers thinner than the absorption length necessary for photoresponse at longer wavelengths, corresponding to the indirect band gap. This allows the $\Gamma-$valley energy gap of 2.78eV to dominate the photoresponse, creating a quasi-direct band gap semiconductor. Figure 4.1 illustrates this point by showing the power absorption of three key wavelengths for GaP UV detectors. The power absorption was calculated according to $P_d/P_o = e^{-\alpha d}$, where P_d is the power at depth d from the incident surface, P_o is the incident power, and α is the absorption coefficient. From this figure we can see that within a micron of the surface virtually no light corresponding to the indirect band gap (550nm) is absorbed, while over 60% of light at the direct band gap (440nm) transition is absorbed. At the UV wavelength of interest (290nm) 99% of the light is absorbed within 50nm of the surface. Schottky photodiodes have utilized this increased absorption at shorter wavelengths, where device operation occurs near the surface of the device. Though some UV GaP Schottky photodiodes are already on the market,[7] none report gain. Gain is necessary for many UV applications, as well as for being a competitive alternative to PMTs.

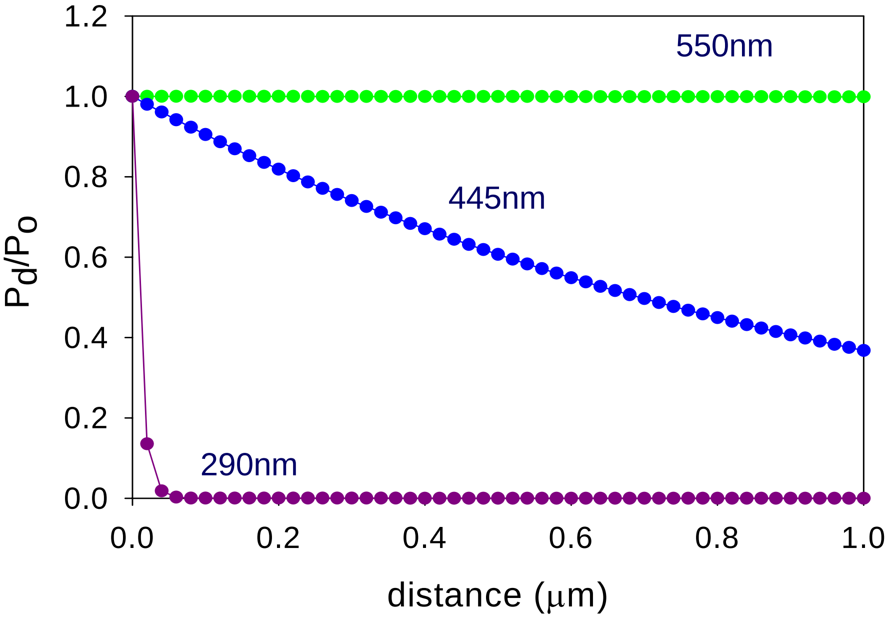

Figure 4.1 Power absorption of light from the incident surface for (•) 550nm, corresponding to the 2.26eV indirect band gap of GaP, (○) 445nm, corresponding to the direct 2.78eV band gap, and (▲) 290nm, corresponding to the solar-blind cutoff wavelength.

Section 4.1 of this chapter will discuss the results of the first characterization of GaP APDs that employ thin device layers in order to utilize the high absorption coefficients of GaP at short wavelengths. These devices have attained high gain and low dark current, but the UV quantum efficiency (QE) remains low. Thus Section 4.2 will discuss a Schottky p-i-n structure that enhances the UV QE.

4.1 GaP Avalanche Photodiodes

4.1.1 Material Structure and Device Fabrication

Two device structures were processed and characterized for our initial study. Both devices were from the same wafer and consisted of a p-i-n structure grown on a thin semi-insulating layer on an n-type GaP substrate, as shown in Figure 4.2. The thickness of the p, i, and n layers were 300nm, 300nm and 500nm, respectively. The dopant concentration was $2x10^{18}$ cm^3 for the n-type layer, and the p-layer was graded from $2x10^{18}$ cm^3 at the p-i interface to $2x10^{19}$ cm^3 at the top surface.

Device fabrication employed standard photolithography for all three mask layers. An etchant consisting of equal parts HNO_3:HCl:H_2O defined the mesas.[8] Next a SiO_2 passivation layer was deposited via plasma enhanced chemical vapor deposition (PECVD). Contacts were then formed on the devices using electron-beam evaporation and a standard lift-off process. The n-type contacts consisting of AuGe/Ni/Au were evaporated onto the device followed by a 30 second anneal at 430°C. Finally, Ni/Au p-type contacts were deposited to yield a device with the cross section shown in Figure 4.2(a), which will be referred to as the standard device. Figure 4.2(b) shows the device cross section of additional devices fabricated using a recessed window structure that reduced the p-type layer by 700Å in the window.[9]

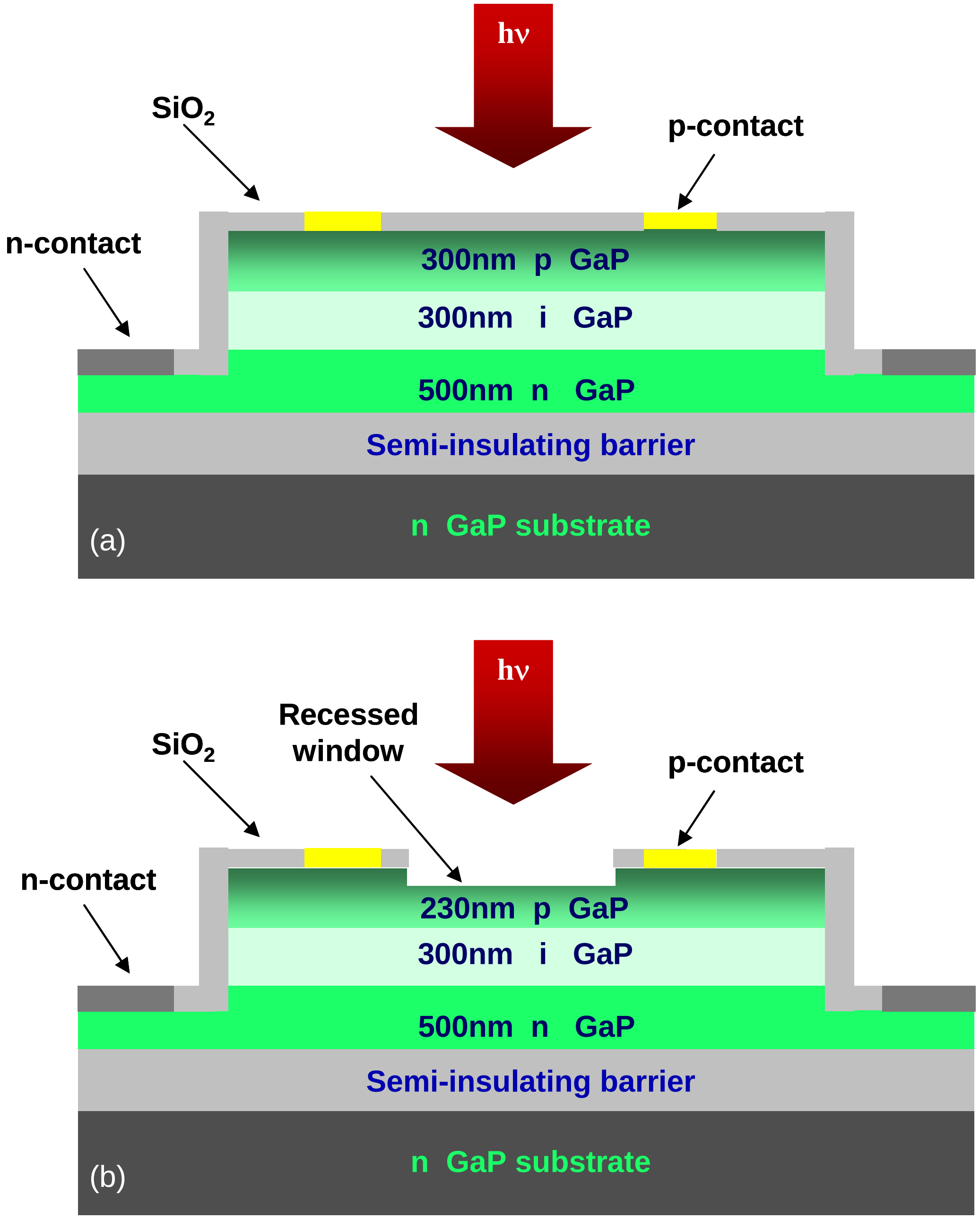

Figure 4.2 Cross-section of (a) standard and (b) recessed window GaP APDs.

4.1.2 Current-Voltage Characteristics

The photoresponse measurements for both devices utilized a broadband UV lamp and an HP4145 parameter analyzer. Figure 4.3 shows the current – voltage (IV) characteristics for both standard and recessed window devices, which demonstrated identical IV characteristics. At unity-gain (~10V) both devices demonstrated low dark currents (<1pA) uniformly across the sample. Devices ranging from 80μm to 250μm in diameter exhibited low dark current densities, <1nA/cm^2, at unity-gain, which were comparable to previous reports of dark current in GaP devices.[10] The dark current and photoresponse remained flat with little dependence on bias voltage prior to the onset of avalanche multiplication. The breakdown voltage was ~21V, corresponding to an electric field of approximately 500kV·cm^{-1}. Both devices showed gains on the order of 10^4.

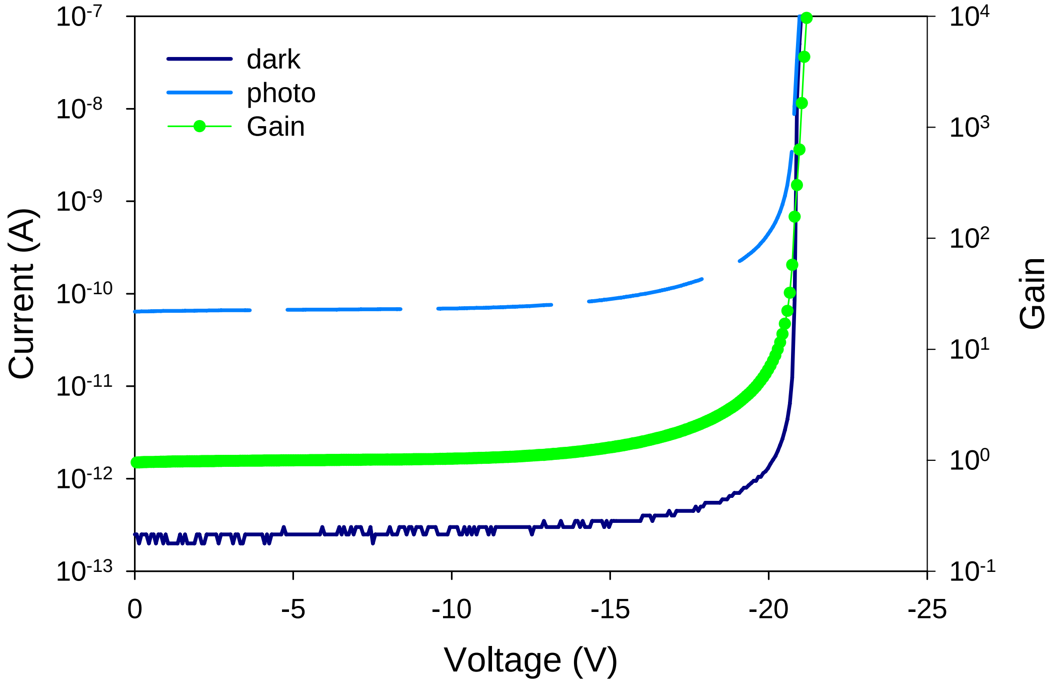

Figure 4.3 IV characteristic for an 80μm-diameter device. IV curves were the same for both standard and recessed window APDs.

4.1.3 Experimental Quantum Efficiency

Figure 4.4 shows the spectral response, for both photodiodes at unity-gain, measured with a xenon lamp source, a monochromator, and a SRS SR850 lock-in amplifier. The peak quantum efficiency for both the standard and recessed window GaP APDs at a wavelength of ~440nm confirmed that the strongest absorption occurred at wavelengths corresponding to the Γ-valley band gap, as intended by using thin device layers. The non-recessed window device had a peak quantum efficiency of only 20% and a spectral range extending from 350nm to 475nm.

In GaP, shorter wavelengths have a higher absorption coefficient and consequently a shorter absorption length. Therefore, increased quantum efficiency in the UV spectrum hinges on these carriers reaching the active region prior to recombination. Also, by shortening the overall thickness of the device, absorption at longer wavelengths was reduced. It follows that additional reduction of the p-region thickness would further increase the quantum efficiency in the ultraviolet range, thus a recessed window structure was implemented.

The recessed window device had a recess depth of ~700Å. The spectral response demonstrated an improved peak quantum efficiency of 38% occurring at ~440nm, as well as enhanced quantum efficiency at wavelengths below 350nm, the lower spectral range limit of the standard devices. Due to the low UV quantum efficiency (~5%) even after employing the recessed window, a Schottky p-i-n device structure was studied.[11] The results of this study will be discussed in Section 4.2. It is worth mentioning here that an additional device structure was studied that had a portion of the top p-layer etched away.

Two samples were processed with 100Å and 1000Å etched from the top surface. The processing for this type of device was much simpler than for the recessed window structure because it eliminated the alignment challenges of the recessed window process. Unfortunately, the lateral resistance of the thinned p-layer was too high, resulting in an approximately 5% decrease in the QE compared to the standard structure, with no improvement in the UV portion of the spectrum.

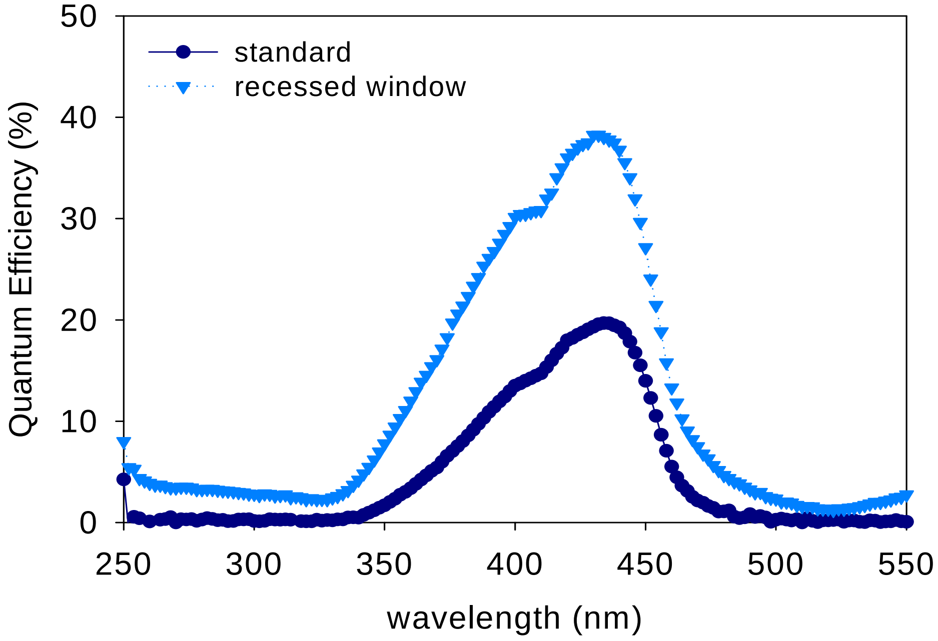

Figure 4.4 Quantum efficiency of a standard GaP APD and a recessed window GaP APD measured at unity-gain.

4.1.4 Modeled Quantum Efficiency

The external quantum efficiency was modeled using the same approach as in References [12-13]. In a p-i-n photodiode structure, photons can be absorbed in each of three layers, contributing to the photocurrent. Photo-generated electrons, or photoelectrons, resulting from photon absorption in the neutral p-layer diffuse to the active region according to equation (4.1)

$$\eta_p = \frac{\alpha \cdot L_e}{\alpha^2 \cdot \left(L_e\right)^2 - 1} \cdot \left[\frac{\alpha \cdot L_e + \gamma - e^{-\alpha \cdot x_p} \cdot \left(\gamma \cdot \cosh\left(\frac{x_p}{L_e}\right) + \sinh\left(\frac{x_p}{L_e}\right) \right)}{\gamma \cdot \sinh\left(\frac{x_p}{L_e}\right) + \cosh\left(\frac{x_p}{L_e}\right)} - \alpha \cdot L_e \cdot e^{-\alpha \cdot x_p} \right] \tag{4.1}$$

where α is the absorption coefficient, L_e is the electron diffusion length, x_p is the thickness of the neutral p-region, $\gamma = s \cdot L_e / D_e$, s is the surface recombination velocity, and D_e is the electron diffusion coefficient. Equation (4.2) describes the drift current contribution from both electrons and holes generated from photon absorption in the active region, which includes the i-region and the depletion region.

$$\eta_d = e^{-\alpha \cdot x_p} \cdot \left(1 - e^{-\alpha \cdot x_d}\right) \tag{4.2}$$

where x_d is the sum of the thickness of the depletion and i- regions. At unity-gain, the calculated depletion width was ~70nm. Finally, photons absorbed in the n-region contribute holes generated within a diffusion length of the active region, expressed by equation (4.3).

$$\eta_n = \frac{\alpha \cdot L_h \cdot e^{-\alpha \cdot \left(x_p + x_d\right)}}{\alpha^2 \cdot \left(L_h\right)^2 - 1} \cdot \left(\alpha \cdot L_h - \coth\left(\frac{x_n}{L_h}\right) - \frac{e^{-\alpha \cdot x_n}}{\sinh\left(\frac{x_n}{L_h}\right)} \right) \tag{4.3}$$

where L_h is the hole diffusion length and x_n is the thickness of the neutral n-region. The total quantum efficiency, η_t, is the sum of (4.1), (4.2), and (4.3) multiplied by T the optical transmittance through the incident surface.

$$\eta_t = \left(\eta_p + \eta_d + \eta_n\right)\cdot T \tag{4.4}$$

The optical and electrical constants were taken from Reference [6], with the exception of the electron diffusion length, L_e, reported as 0.85-2μm in Reference [14]. The electron and hole diffusion lengths, surface recombination velocity and transmittance were used as fitting parameters. The surface recombination velocity, reported as $4\cdot10^6$cm/s in Reference [6], had a much greater effect on the short wavelength efficiency, which varied by as much as 35% from $s = 0.4\cdot10^6$cm/s to $4\cdot10^7$cm/s, than on the peak efficiency, which varied less than 10% over the same range of s.

Varying the electron diffusion length had the greatest effect on the QE at both short wavelengths and the peak wavelength. The peak efficiency dropped more than 20% for a one order of magnitude reduction in the electron diffusion length. Reducing the diffusion length too much resulted in a premature short wavelength cutoff. Hole diffusion lengths longer than 300nm resulted in the neutral n-region contribution dipping below zero. The hole diffusion length was set to 50nm. This unusual behavior in the n-region may be attributable to the semi-insulating barrier. Figure 4.5 shows the result of this model, using an effective electron diffusion length of 70nm, to fit the short wavelength cutoff and reduce the overall efficiency to levels similar to those measured, and a surface recombination velocity of 10^7cm/s, to reduce the efficiency below 1% for

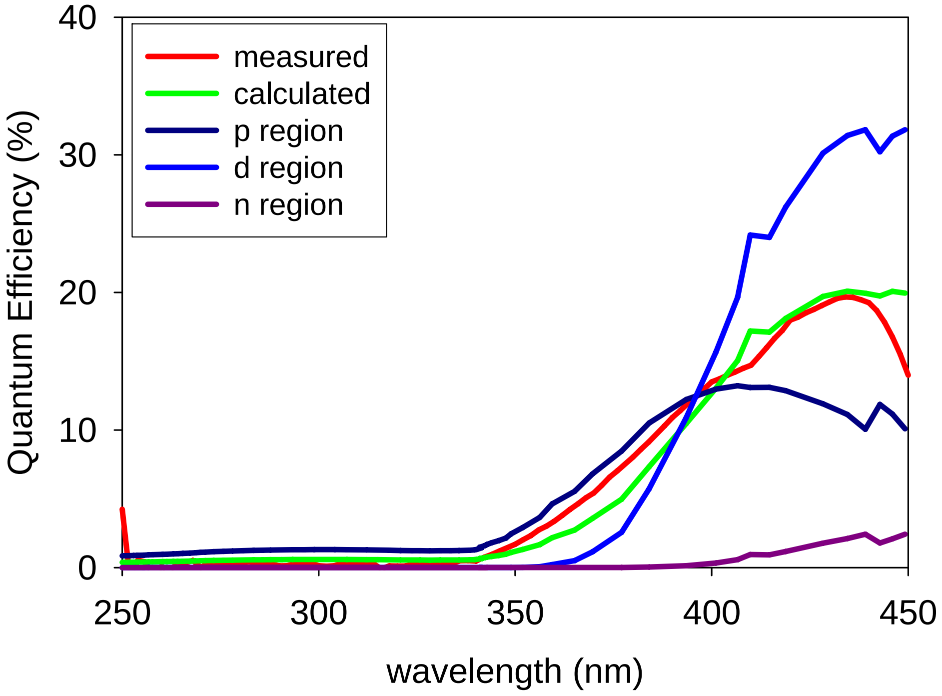

Figure 4.5 Modeled and calculated external quantum efficiency for the standard GaP APD at unity-gain. The calculated efficiency is the sum of the p-, d-, and n- region efficiencies.

wavelengths less than 350nm. We attribute the shorter effective diffusion length to surface band-bending.[12,15] The model correctly predicts the notch around 400nm, the short wavelength cutoff at ~350nm, and the peak efficiency at 440nm, but the only way to approach the magnitude of the measured efficiency was to reduce the transmittance to 45%. This transmittance is lower than expected, even for an un-optimized anti-reflection coating.

The calculated quantum efficiency for the recessed window device, shown in Figure 4.6, started with the same values for all the constants and variables except for x_p which was reduced by the 700Å etch depth of the window. The best fit to the measured

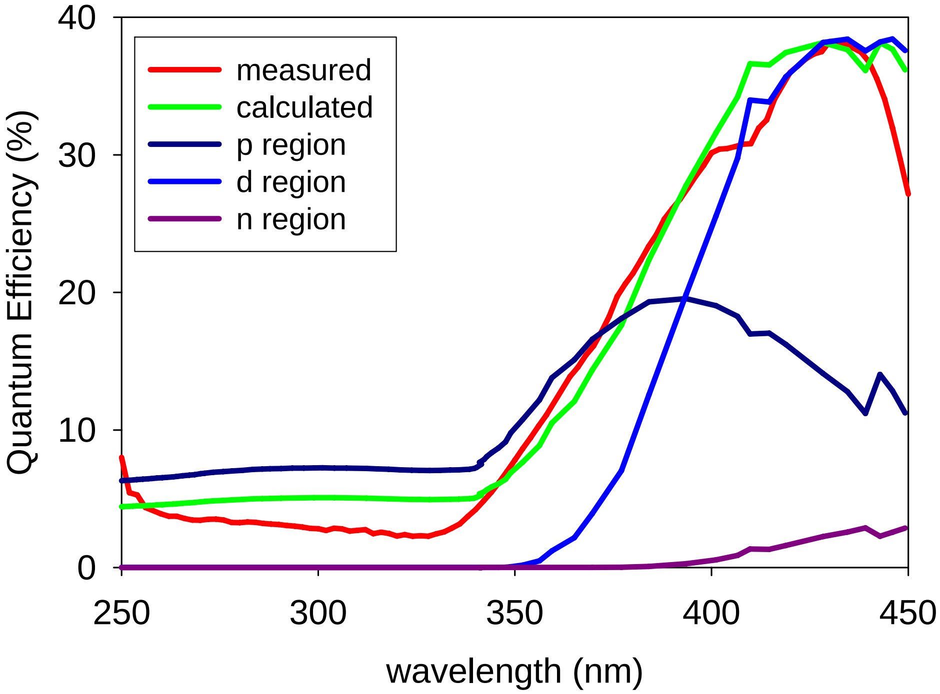

Figure 4.6 Modeled and calculated external quantum efficiency for the recessed window GaP APD at unity-gain. The calculated efficiency is the sum of the p-, d-, and n- region efficiencies.

data was obtained using a surface recombination velocity of $1.5 \cdot 10^6$cm/s and a transmittance of 70%, which was the expected transmission for bare GaP. Further reduction of the p-region indicated that a deeper recess may be able to increase the QE more than five times.

4.1.5 Avalanche Noise

The excess noise of an APD originates from the statistical nature of impact ionization events. The ratio of ionization coefficients for electrons and holes, α and β, respectively, strongly influence the excess noise factor, F. The ratio $k=\beta/\alpha$ should be minimized for electron-initiated gain and maximized for hole-initiated gain. The equation governing this behavior is:

$$F_n = M_n \cdot \left[1 - (1 - k) \cdot \left(\frac{M_n - 1}{M_n} \right)^2 \right] \tag{4.5}$$

for electron-initiated gain, where M_n is the electron multiplication factor, and

$$F_h = M_h \cdot \left[1 - (1 - k) \cdot \left(\frac{M_h - 1}{M_h} \right)^2 \right] \tag{4.6}$$

for hole-initiated gain, where M_h is the hole multiplication factor.[16]

The excess noise factor, F(M), of the standard GaP devices was measured using an HP8970B noise figure meter with a standard noise source and an Argon laser (351, 363nm). Using (4.5) yielded an effective k value of 0.4 for the standard GaP APDs, as shown in Figure 4.7.

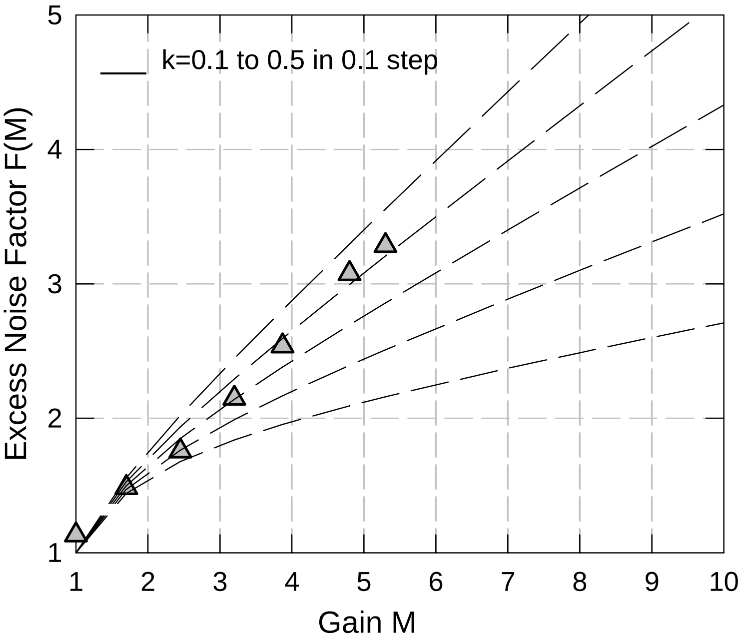

Figure 4.7 Excess noise factor versus gain for the standard GaP APD: UV(351, 363nm), RT.

Bulk GaP has been reported to have equal ionization coefficients for holes and electrons, which yields an effective k value of 1.[6] The much lower excess noise achieved in the GaP APDs was attributed to the short UV absorption length, which resulted in single-carrier injection at the measurement wavelength. This was confirmed by examining the power absorption of 363nm light, according to $P_d/P_o=e^{-\alpha d}$, where P_d is the power at a depth of d in the device, P_o is the incident power, and α is the absorption coefficient obtained from Reference [6]. $P_d/P_o= 1.8*10^{-3}$ and $3.4*10^{-6}$ at the p-i and i-n interfaces, respectively. Additionally, the dead length effect in these devices played a much more significant role in the short i-region than in bulk material. This dead length effect reduced the high gain tail of the gain distribution, thus reducing the excess noise.[17]

4.1.6 Speed

The normalized pulse response data of the standard GaP APD, shown in Figure 4.8a, indicated that the device speed was RC limited, as evidenced by the exponential tail. The speed response was taken using a 266nm Nd:YAG laser with a 500ps pulse width and a 7.5kHz period. The device speed was measured at unity-gain, as well as at gains of 5, 15, and 30. The gain was determined from the dc response and confirmed to match the gain acquired from the ac response obtained from the Fast Fourier Transform (FFT) of the pulse response. A device capacitance of 12.25pF resulted from a 240μm-diameter GaP APD, which agreed well with the calculated capacitance of 12.2pF. The device measured was larger than desirable for speed measurements, due to the constraints of the probe geometry, which had a large pitch. The large capacitance thus contributed to an RC limitation of ~250MHz. Taking the Fast-Fourier Transform (FFT) of the time response, shown in Figure 4.8(b), resulted in a frequency of f_{3dB} ~210MHz, at unity-gain. The bandwidth slowly decreases with gain, reaching a 110 MHz at a gain of 30, thus at high gains the device became transit time limited.

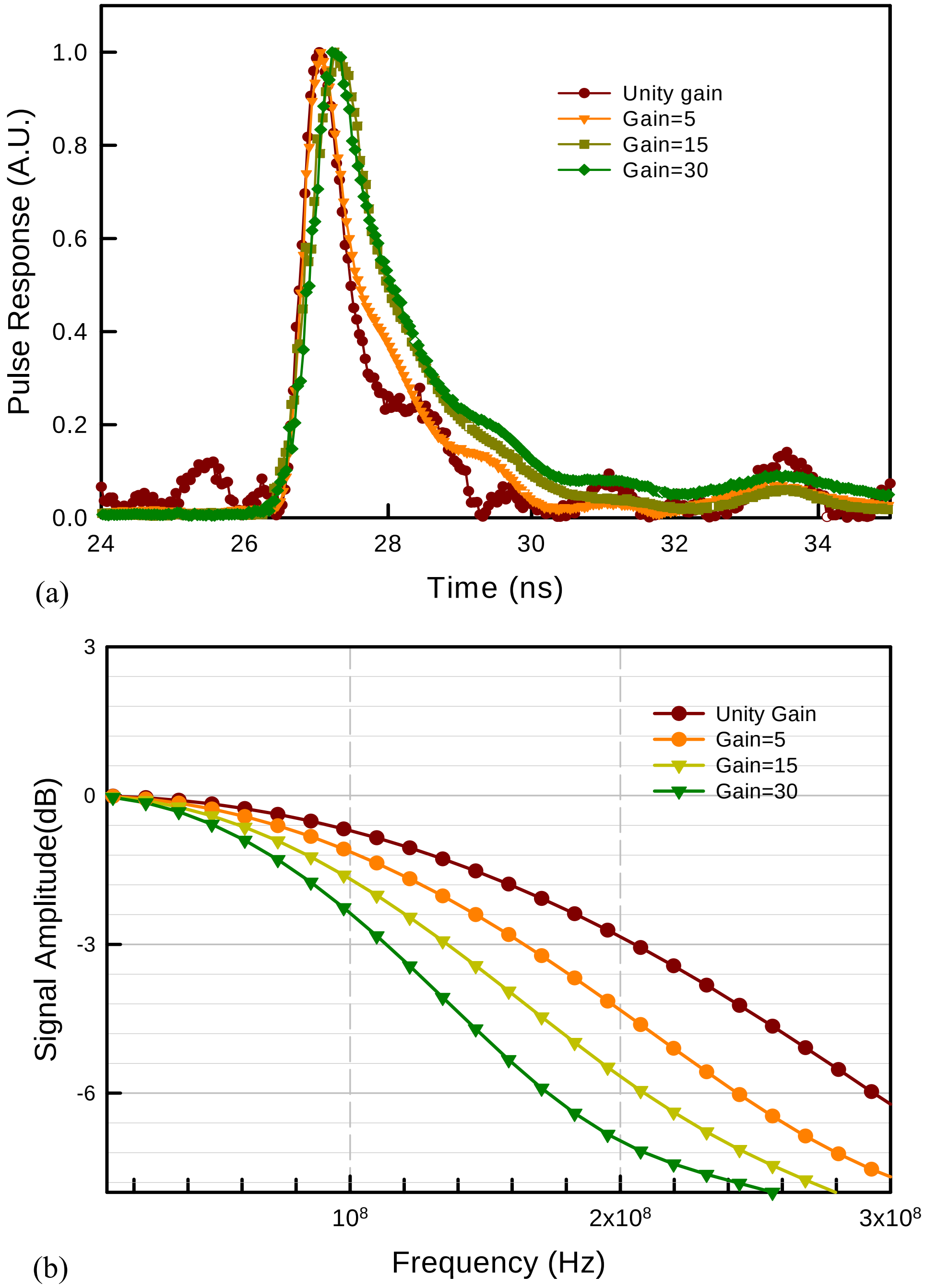

Figure 4.8 (a) Normalized time domain speed response and (b) bandwidth of GaP APDs.

4.2 Schottky p-i-n GaP Photodiode

4.2.1 Material Structure and Device Fabrication

The low UV quantum efficiency (~5%) in the recessed window devices prompted the study of two Schottky devices.[18] These devices consisted of an n-type substrate with a thin semi-insulating buffer layer, followed by an n-i-p-i structure. The layer thicknesses were 1000nm, 100nm, 50nm, and 250nm, respectively, with a doping concentration of $1\text{x}10^{18}$ cm^3 for both the n- and p- layers. Processing of the first device utilized the same procedure as the standard devices in Section 4.1.1. The second device varied only in that it had a thin, semitransparent metal contact covering the mesa, as shown in Figure 4.9.[18-19] The Schottky contacts were Ti/Au, and the thin metal was 100Å Au. Only the unity-gain quantum efficiency characteristics of the Schottky devices will be discussed, since these devices did not perform as APDs, which we attribute to higher defect densities.

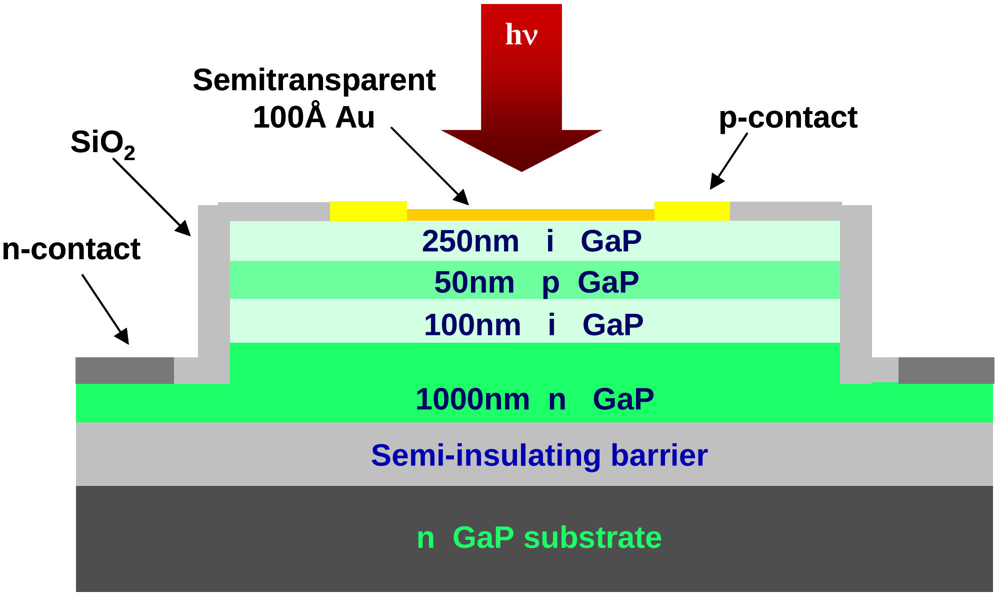

Figure 4.9 Cross-section of a Schottky p-i-n GaP photodiode with 100Å Au semitransparent contact.

4.2.2 Quantum Efficiency

The top i-layer in the Schottky p-i-n structure was designed to create a field at the absorption surface of the device in order to sweep the UV photons absorbed near the surface to the active region. This field should be high enough to mitigate the effects of surface recombination velocity, discussed in Section 4.1.4, but not so high as to initiate impact ionization. Figure 4.10 shows the calculated field profile for this structure.

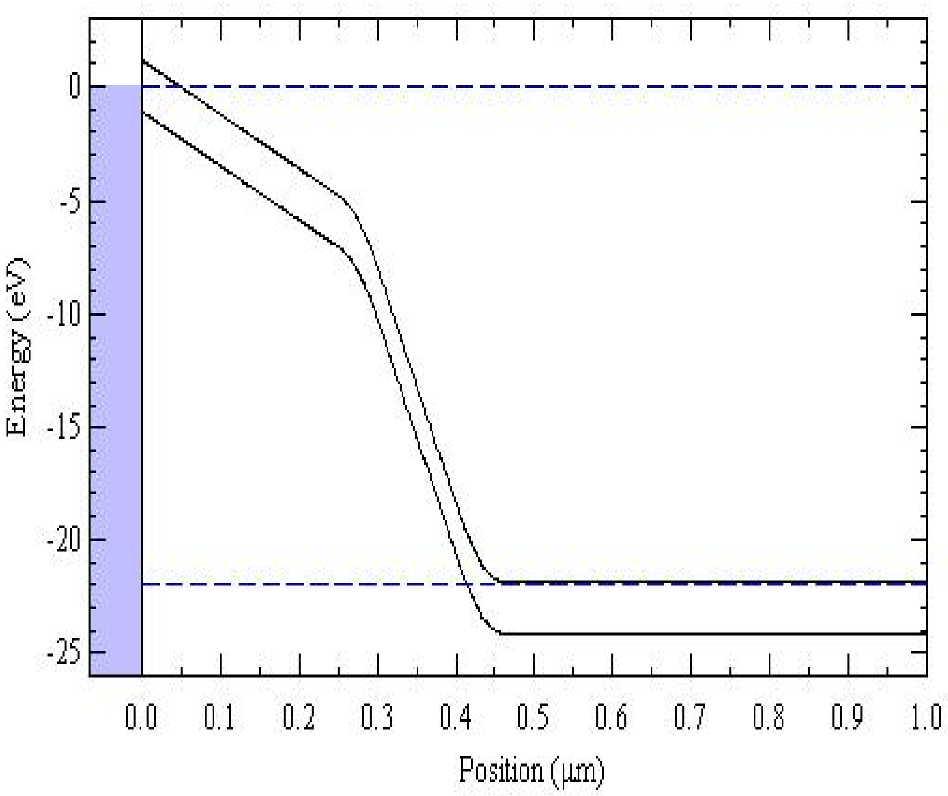

Figure 4.10 Electric field profile of Schottky p-i-n GaP photodiode calculated with Band Profiler.

The Schottky devices fabricated without using the semitransparent contact exhibited quantum efficiency characteristics, shown in Figure 4.11, nearly identical to the standard APD. The quantum efficiency of the devices with a semitransparent metal contact demonstrated almost 15% quantum efficiency below 300nm, a flat peak response of ~16% from 362nm to 425nm, and a cut off wavelength of 450nm. This improved quantum efficiency in the sub-290nm wavelength range was attributed to the semitransparent contact spreading the electric field across the device mesa, allowing more efficient collection of higher energy photons.[19]

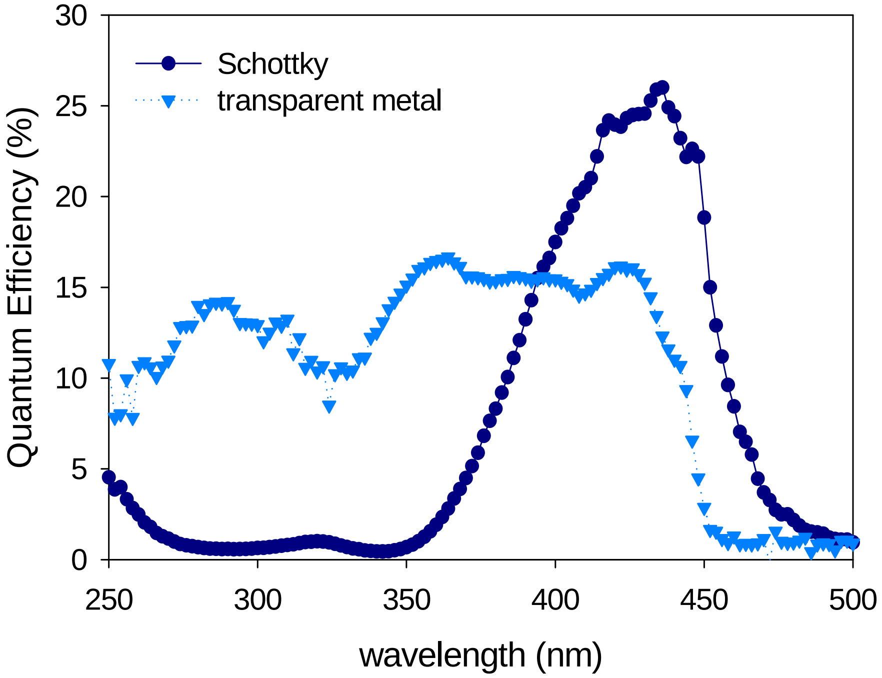

Figure 4.11 Quantum efficiency of a standard Schottky p-i-n photodiode and a Schottky p-i-n photodiode with a semitransparent metal contact, measured at unity-gain.

4.3 Conclusion

Both p-i-n and recessed window p-i-n structures, as well as a Schottky structure, were implemented using GaP avalanche photodiodes with thin device layers. The results showed low dark current, good quantum efficiency, and high gain up to 10^4, with good uniformity across the wafer. The peak quantum efficiency at 440nm indicated Γ-valley absorption, rather than band edge absorption. The recess window device structure confirmed the enhancement of UV detection via reduction of the p-layer thickness. Additionally, the Schottky structure demonstrated potential for enhanced UV detection, when employing a thin semitransparent contact.

Though these results indicated that successful implementation of the Schottky structure with avalanche breakdown could achieve a device with both high gain and strong QE performance below 290nm, SiC APDs outperformed GaP APDs in every performance area as illustrated in Table 4.1. The strong response of these devices in the 350nm-450nm range would be best suited for detecting NADH fluorescence in the biological agent detection system.

Table 4.1 Basic parameter comparison of GaP and SiC.

	Unity Dark Current	Gain	QE	Visible QE	Noise (k)
GaP	0.5pA	10^4	14%	Peak response	0.4
SiC	0.1pA	10^6	50%	Visible-blind cutoff	0.12

Chapter 5

Processing and Characterization of 4H-SiC Avalanche Photodiodes

The avalanche photodiodes (APDs) used for the experiments in the remaining chapters were all fabricated from one of the three wafer structures grown by Cree, Inc., as shown in Figure 5.1. The first structure was a basic p-n junction structure, consisting of a thin 100nm p^+-cap layer, a 200nm p-layer, and a 2μm n-layer grown on an n^+ 4H-SiC substrate. Secondary ion mass spectroscopy (SIMS), by Evans Analytical Group, indicated doping levels of $4x10^{19}cm^{-3}$, $1.5x10^{18}cm^{-3}$, and $2.5x10^{18}cm^{-3}$ for the p^+-, p-, and n- layers, respectively, as shown in Figure 5.2(a).

Figure 5.1 Wafer structures used for SiC APDs, including (a) p-n junction, (b) p-i-n with a 260nm i-region, referred to as PIN260, and (c) p-i-n with a 480nm i-region, referred to as PIN480.

The second and third samples had p$^-$ active regions with thicknesses of 260nm and 480nm, which will be referred to as PIN260 and PIN480, respectively. PIN260 consisted of an 80nm p$^+$-cap layer, 250nm p-layer, 260nm p$^-$-layer, and a 2μm n-layer grown on an n$^+$ 4H-SiC substrate. SIMS analysis revealed doping densities 1x10^{19}cm^{-3}, 2.4x10^{18}cm^{-3}, 1x10^{16}cm^{-3}, and 4x10^{18}cm^{-3} for the p$^+$, p, p$^-$, and n layers, respectively, as shown in Figure 5.2(b). Finally, the third structure had a 200nm p$^+$-cap layer, 225nm p-layer, 480nm p$^-$-layer, and a 2μm n-layer grown on an n$^+$ 4H-SiC substrate, with doping densities of 1.5x10^{19}cm^{-3}, 1.5x10^{18}cm^{-3}, 1x10^{16}cm^{-3}, and 4.8x10^{18}cm^{-3}, respectively, as shown in Figure 5.2(c).

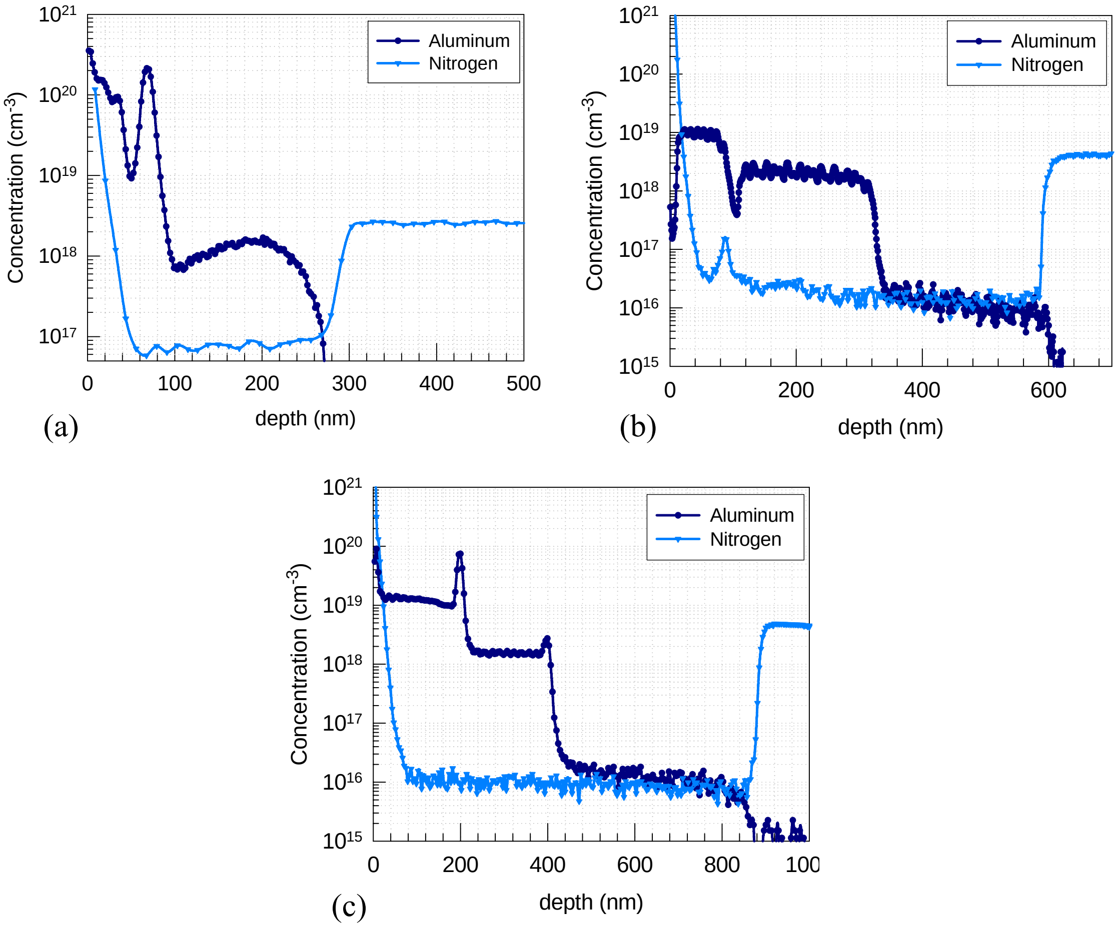

Figure 5.2 SIMS analyses of doping densities for SiC (a) p-n junction, (b) PIN260, and (c) PIN480 APDs.

Devices from all three wafers followed the same basic process. Reactive ion etching (RIE) defined the mesas. Initially, the mesas had a vertical side wall, but premature edge breakdown (Chapter 6) prompted the implementation of beveled edges.[1] Approximately 2000Å of SiO_2 was deposited as a passivation and antireflection layer using plasma enhanced chemical vapor deposition (PECVD). Both n- and p- contacts were deposited via e-beam evaporation and defined by a standard lift-off process. The metals used for both contacts were determined using the transfer length method (TLM), which will be discussed in Section 5.1.2. Finally, Ti/Au probe pads were deposited on samples to be used in photon counting experiments. Further details of the device fabrication procedure are outlined in the Appendix.

5.1 Processing Techniques

5.1.1 Beveled Edge Mesa Formation

Standard unbeveled mesas were masked using a 5µm-thick AZ4330 photoresist mask spun at 4krpm for 40 seconds and baked in an oven at 120ºC for 30 minutes. Lithography for the etching of a beveled mesa sample employed an 8µm-thick photoresist mask using either AZ4620 spun at 4krpm for 40 seconds or AZ 4330 spun at 3krpm for 30 seconds. After developing, a hotplate bake at 140ºC for 3 minutes pulled in the edges of the photoresist creating a rounded dome profile as shown in Figure 5.3(a). AZ4330 resulted in a shallower angle than AZ4620. According to a process developed by Yan et al.[2], the bevel angle of the photoresist decreases with both higher bake temperatures and

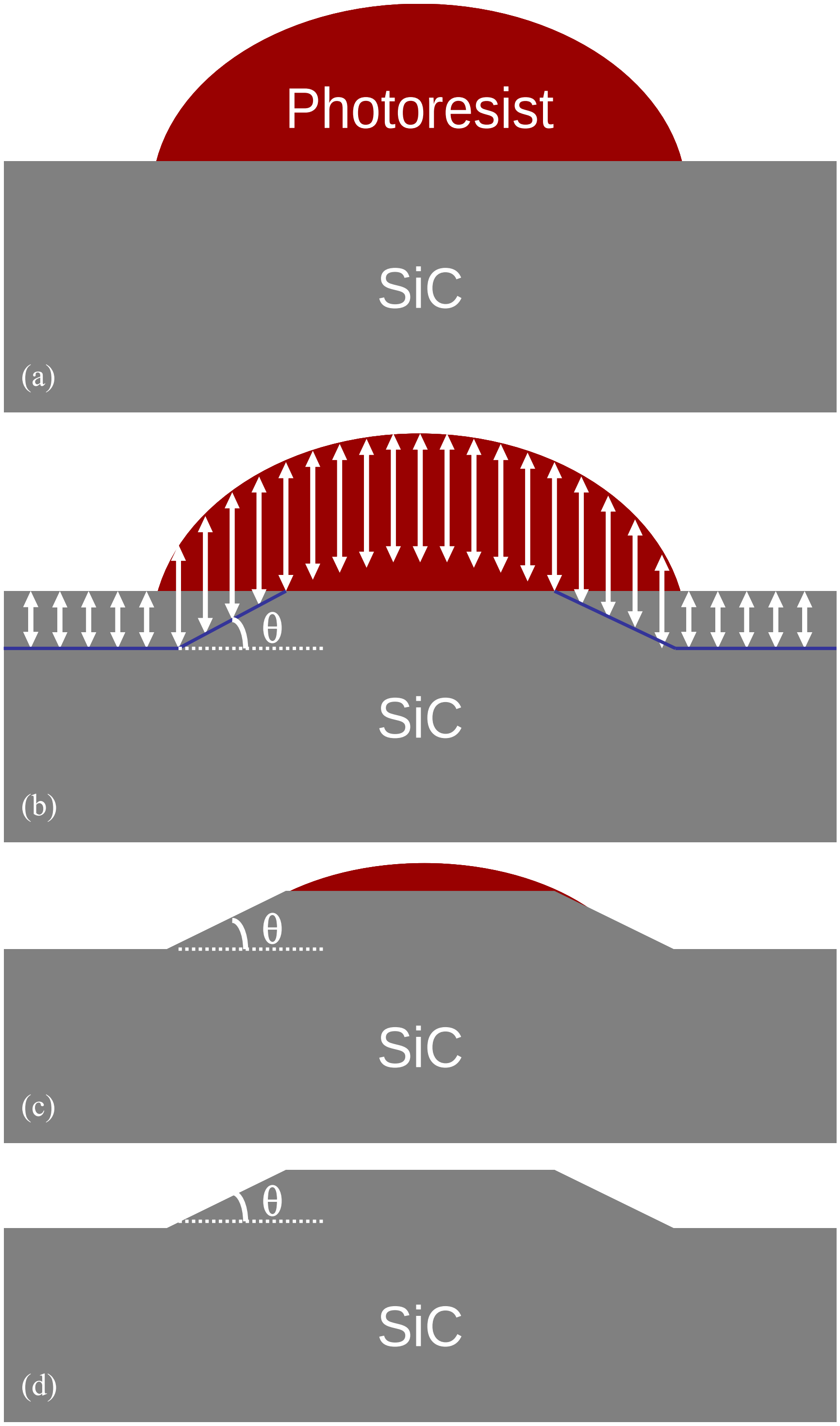

Figure 5.3 Beveled edge process showing (a) SiC wafer with dome shaped photoresist, (b) RIE etch depth represented by white arrows on the wafer and photoresist, (c) after removal from the RIE with remaining photoresist, and (d) resulting beveled mesa on SiC after removal of residual photoresist.

longer bake times. This is due to higher and longer bake temperatures increasing the surface tension, thereby reducing the bevel angle of the photoresist.

The sample was then RIE etched using BCl_3 and $SiCl_4$ at an 8sccm flow rate, 100W RF power, and 50mTorr, yielding an etch rate of approximately 175Å/minute. During RIE etching, the photoresist etches at a faster rate than the SiC surface, thus the SiC mesa takes on an exaggerated angle of the photoresist according to the equation[3]:

$$\tan(\theta) = \left(\frac{d_{SiC}}{d_{PR}}\right)\cdot\tan(\alpha) \tag{5.1}$$

where θ is the angle of the SiC mesa to the wafer surface, (d_{SiC}/d_{PR}) is the selectivity of etching SiC to etching the photoresist mask, and α is the angle of the photoresist mask to the SiC surface before etching. Typical mesas had a bevel angle between 5-10°, as shown in Figure 5.4. The bevel angle was approximated to first order using a calibrated Olympus microscope at 80X magnification.

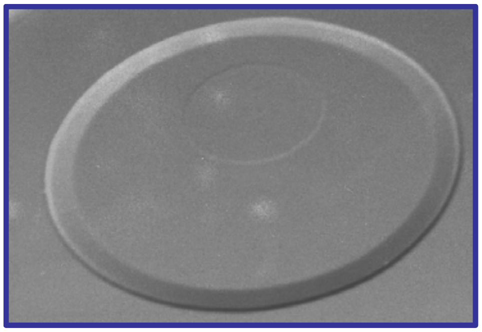

Figure 5.4 SEM photograph of beveled edge mesa.

5.1.2 Ohmic Contacts

Achieving good ohmic contacts is important for minimizing contact resistance, thereby reducing the overall series resistance of the device. The transfer length method (TLM), also referred to as the transmission line model, is a relatively simple technique for determining the contact resistance. Figure 5.5 shows the basic structure used for the measurement. Contacts of equal size are spaced at varyied distances, d, from each other and electrically isolated using a mesa structure. IV measurements taken by probing adjacent contacts yields a set of IV curves (Figure 5.6(a)), the inverse slope of which is a resistance consisting of the contact and sheet resistances. The total resistance, R_T, is then plotted as a function of contact spacing, as in Figure 5.6(b). The contact resistance and sheet resistance can be extrapolated according to[4-5]:

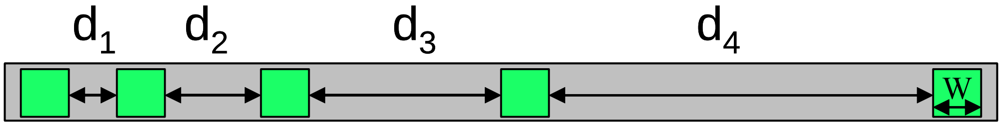

Figure 5.5 Mesa isolated contacts of equal size and varyied spacing used for extrapolating contact resistance in the transfer length method.

$$R_T = \frac{R_s}{W} \cdot \left(d + 2 \cdot L_T\right) \tag{5.2}$$

where R_S is the sheet resistance, W is the width of the contacts, d is the spacing between contacts, and L_T is the linear transfer length. The specific contact resistance, ρ_c, can be determined from:

$$\rho_c = \left(L_T\right)^2 \cdot R_s \, . \tag{5.3}$$

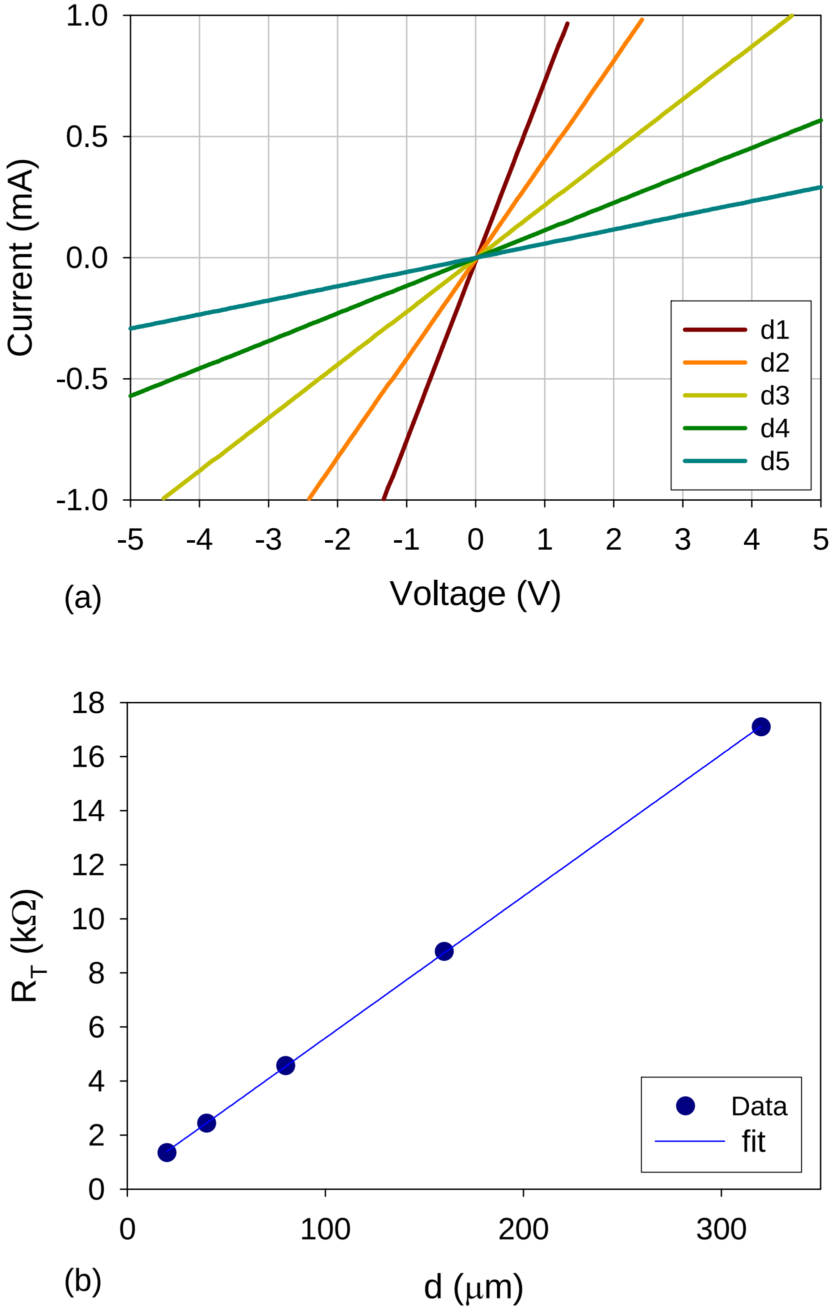

Figure 5.6 (a) IV measurements taken by probing consecutive contacts. The inverse slope of each line is the resistance corresponding to contact separation. (b) Plot of the resistances from the IV curves versus the contact spacing. The specific contact resistance can be calculated from the linear fit.

Four samples from the p-n junction wafer were tested for p-type contact resistance, with metal contacts consisting of Al/Ti, Ti/Al, Ti/Al/Ti, and Ni, where the metals are listed in order of proximity to the surface. Table 5.1 lists the thicknesses along with rapid thermal anneal temperatures and times. The sheet resistance was calculated to be 5-10kΩ/□. Aluminum, titanium, and nickel reportedly achieved contact resistances on the order of $10^{-4}\Omega\cdot cm^2$.[4-9] These values were all reported for higher doping levels (~10^{20}) and much higher anneal temperatures (~950 - 1050°C) than the test samples. The anneal temperatures were limited by contact metal diffusion into the thin device layers. The device will short if the metal diffuses to the junction or the depletion region extends to the metal diffusion depth.[6] At a temperature of 800°C and anneal time of 2 minutes, the device yield was sufficiently high.

Table 5.1 Deposited metals, thickness, anneal conditions, and resulting resistivities.

Metal	**Thickness (Å)**	**Anneal Temperature/ Time (°C/min)**	**ρ_c ($\Omega\cdot cm^2$)**
Al/Ti	800/200	800/ 2	$5\cdot10^{-3}$
Ti/Al	250/800	800/ 0.5	$2.5\cdot10^{-3}$
Ti/Al/Ti	100/900/100	800/ 2	$5\cdot10^{-4}$
Ni	1000	800/ 2	$1\cdot10^{-3}$

The contact resistances for the Al/Ti, Ti/Al, Ti/Al/Ti, and Ni contacts were $5\cdot10^{-3}$ $\Omega\cdot cm^2$, $2.5\cdot10^{-3}$ $\Omega\cdot cm^2$, $5\cdot10^{-4}$ $\Omega\cdot cm^2$, and $1\cdot10^{-3}$ $\Omega\cdot cm^2$, respectively. A longer anneal time for the Ti/Al contacts could reduce the contact resistance to levels comparable to the Ti/Al/Ti contacts; however, aluminum is prone to oxidation, which increases the contact resistance of the probe tips, thus a titanium top layer is preferable. While published results indicate lower resistivities than reported here, the order of magnitude difference in doping and the higher anneal temperatures used in those studies easily account for the discrepancy.

As-deposited Ni contacts exhibited ohmic behavior, contrary to reports in Reference [8], though the contact resistance was only $10^{-2}\Omega\cdot\text{cm}^2$. This attribute can be quite useful for on-mesa wire bonding of devices, since the surface roughness from annealing the samples prevented the wire bonds from sticking. Unfortunately, on-mesa wire bonding increased the leakage current an order of magnitude, thus Ti/Al/Ti contacts in conjunction with Ti/Au probe pads were used for packaging devices. While the Ti/Al/Ti contacts provided a sufficiently low contact resistance for the p-n junction devices, the lower doping in the p^+ contact layer of the PIN260 and PIN480 samples prompted a renewed search for high quality contacts to p-type SiC. Xiangyi Guo investigated the use Ni/Ti/Al/Au contacts, based on Tsukimoto et al.,[10] which yielded a contact resistance of $9\cdot10^{-5}\ \Omega\cdot\text{cm}^2$.

5.2 Electrical Characterization

Figure 5.7 shows the IV characteristics for typical p-n junction, PIN260 and PIN480 100μm-diameter APDs. These are the same devices used for the single photon counting experiments in Chapters 7 and 8. At low bias voltages, all three devices demonstrated low dark currents (~1pA). The dark current in the p-n junction device began to rise at ~40V reverse bias, increasing by almost two orders of magnitude at the onset of avalanche gain. This increase in the dark current was attributed to tunneling current, resulting from the thin depletion region.[11] The dark current in PIN260 and PIN480 remained relatively flat until the onset of multiplication gain, since the i-region thickness was sufficient to suppress tunneling current.

The photoresponse of all three devices was measured using an Oriel Deuterium broadband UV lamp. The photocurrent for all three devices was relatively flat with only a slight dependence on bias voltage prior to the onset of avalanche multiplication. The dependence on bias voltage resulted from enhanced minority carrier collection due to widening of the depletion region.[13] The unity-gain photocurrent was linearly corrected to account for the bias voltage dependence, following the method discussed in Reference [13], in order to more accurately calculate the gain.

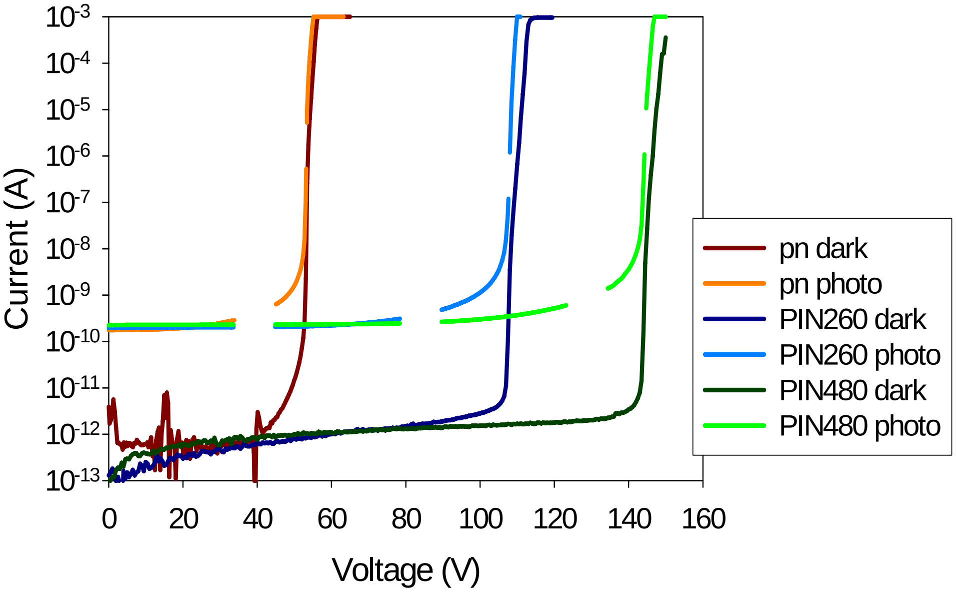

Figure 5.7 IV Characteristics for p-n junction, PIN260, and PIN480 SiC avalanche photodiodes.

APDs from all three structures exhibited gains on the order of 10^6 at bias voltages of 54.5V, 110V, and 146.5V for the p-n junction, PIN260, and PIN480 APDs, respectively, as shown in Figure 5.8(a). The breakdown voltage was arbitrarily determined as the bias at which the gain reached 100. The breakdown voltage for the p-n junction, PIN260, and PIN480 APDs was 52.8V, 107.2V, and 143.25V, respectively. The dark current corresponding to these data points was 2nA, 13pA, and 8pA. Figure 5.8(b) shows the gain as a function of the voltage, V, normalized to the breakdown voltage, V_{Br}, which illustrates the similarity in the breakdown characteristic of the two p-i-n structures.

At high gains, the p-n junction gain curve diverged from the other two gain curves, which was likely due to the spatial non-uniformity of the field. Guo et al. discovered a deviation point of the photocurrent response from the simulated photocurrent, and that this deviation was characteristic of spatial non-uniformity, as shown in Figure 5.9.[14] Non-uniformities in the gain will be discussed in more detail in Chapter 6. Since the gain was calculated directly from the photocurrent, it follows that the same deviation point appears in the gain curve. The non-uniformities result from variations in the doping and i-region thickness. Since the PIN devices experience both of these effects and the p-n junction only experiences the effect of doping variation, it follows that the PIN gain curves will follow the same trend and that this trend will vary somewhat from the p-n junction APDs. The deviation point for the p-n junction, PIN260, and PIN480 APDs occurred at voltages of approximately 53.4V, 108.5V, and 145V, respectively, corresponding to gains of approximately $3 \cdot 10^4$, $6 \cdot 10^4$, and $8 \cdot 10^4$, respectively.

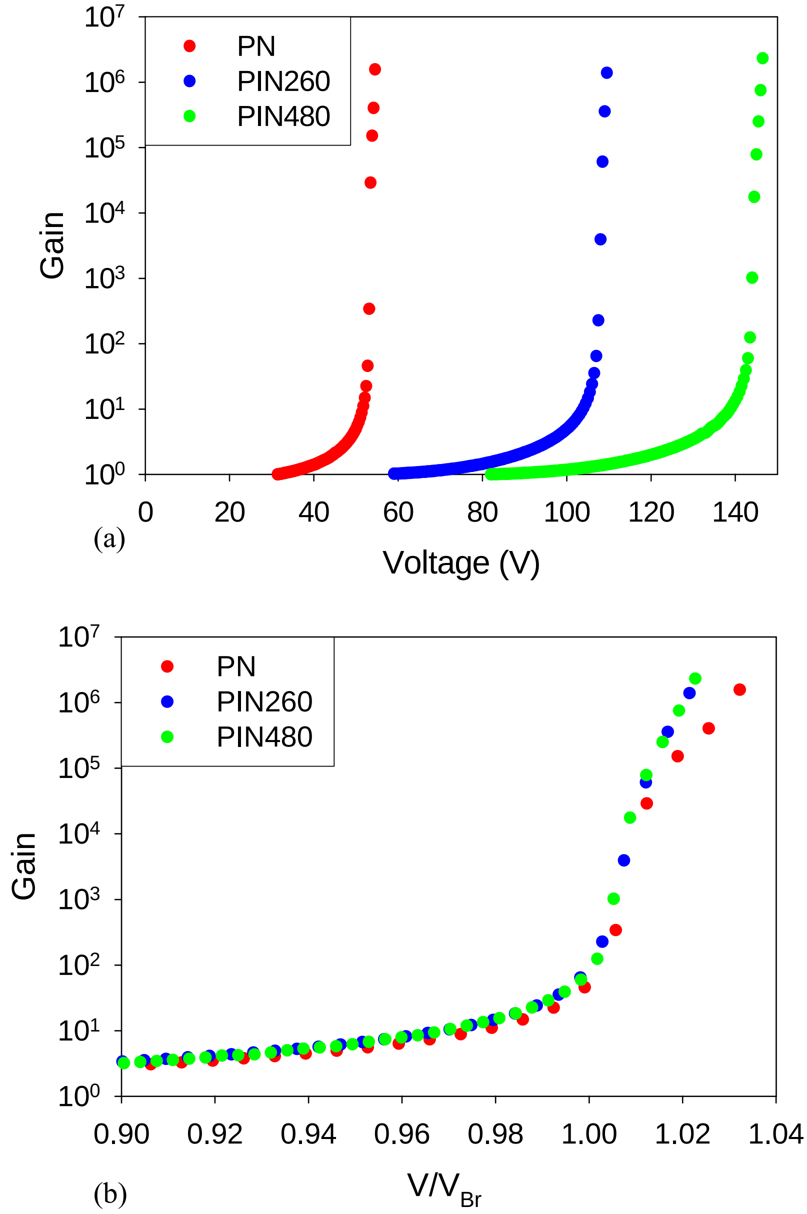

Figure 5.8 (a) Gain-Voltage characteristic of p-n junction, PIN260, and PIN480 SiC APDs. (b) Gain as a function of the voltage, V, normalized to the breakdown voltage, V_{Br}, which was arbitrarily defined as necessary voltage to attain a gain of 100. $V_{Br} = 52.8V$, 107.2V, and 143.25V, for p-n junction, PIN260 and PIN480, respectively.

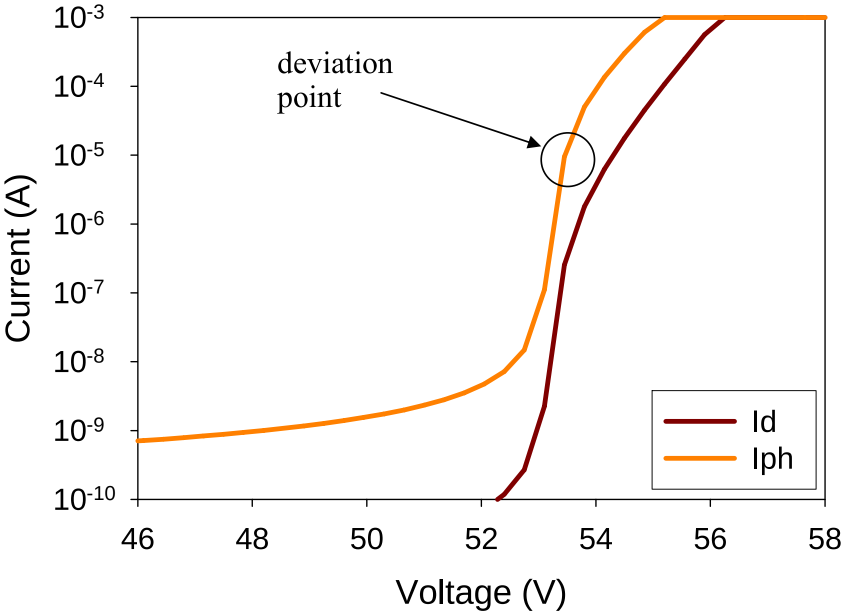

Figure 5.9 Point where simulated photocurrent begins to deviate from the measured photocurrent in a p-n junction APD.

Following basic IV and gain-voltage analysis, the dark current was plotted as a function of diameter at unity-gain, as shown in Figure 5.10. The device diameters ranged from 50µm to 1mm and were fabricated on a sample from the p-n junction wafer. The contributions of the surface current and bulk current can be calculated by fitting the current-diameter curve to:

$$I_{Total} = J_{surface}\cdot\pi\cdot d + J_{bulk}\cdot\pi\cdot(d/2)^2, \tag{5.4}$$

where $J_{surface}$ is the leakage current density that originates at the mesa perimeter, d is the mesa diameter, and J_{bulk} is the leakage current density resulting from the device bulk.

The resulting surface and bulk current densities were 1.66fA/µm and 0.0284fA/µm^2, respectively. For a 100µm-diameter device at unity-gain, the surface current contribution was approximately $1.7\cdot10^{13}$A, and the bulk current contribution was

$8.8 \cdot 10^{-13}$A. These results indicated that the bulk current component of the dark current was slightly larger than the surface current component. When the current-diameter curve was fit only to the bulk term of (5.4) the resulting bulk current density was 0.0335fA/μm^2. This was sufficiently close to the resultant bulk density from fitting the entirety of (5.4) to conclude that bulk current was the main contributor to the total current.

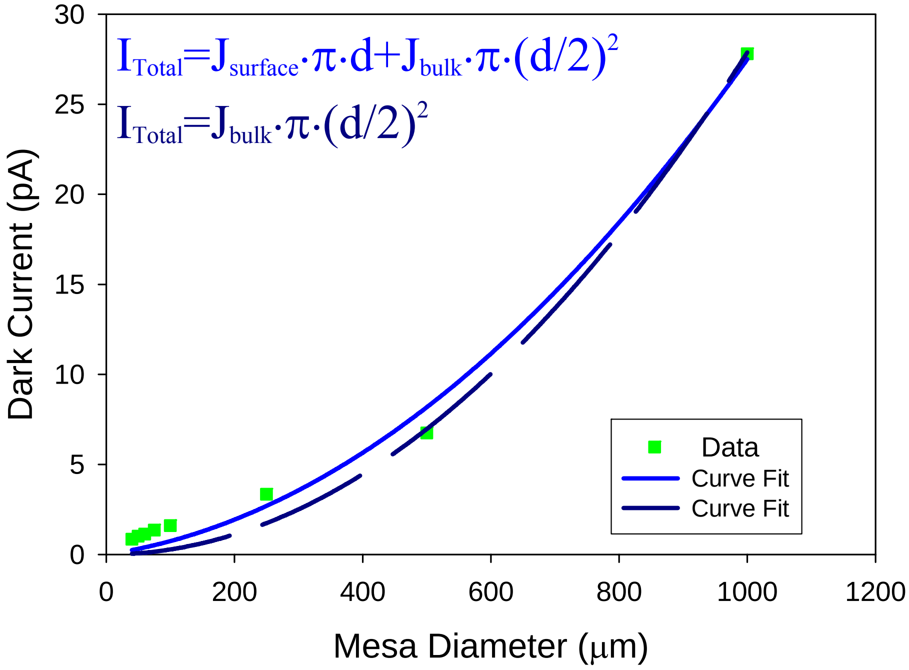

Figure 5.10 Curve fit of the dark current as a function of mesa diameter at unity-gain.

Next, the dark current was plotted as a function of gain in order to determine the multiplied and unmultiplied components of the dark current. This was done using a simple linear fit according to equation (5.5).

$$I_{dark} = I_{unmultiplied} + M \cdot I_{multiplied}, \tag{5.5}$$

where $I_{unmultiplied}$ is the unmultiplied component of the dark current equal to the y-intercept, M is the gain, and $I_{multiplied}$ is the multiplied portion of the dark current equal to the slope. The dark current – gain curves were fitted for the same 100μm-diameter devices measured in Figures 5.7 and 5.8, resulting in the unmultiplied and multiplied dark currents listed in Table 5.2.

Table 5.2 Multiplied and unmultiplied dark current contributions in p-n junction, PIN260, and PIN480 APDs calculated from a linear fit of the dark current – gain curve.

	$I_{unmultiplied}$ (A)	**$I_{multiplied}$ (A)**
p-n junction	$1.1 \cdot 10^{-13}$	$6.5 \cdot 10^{-12}$
PIN260	$7.3 \cdot 10^{-13}$	$1.2 \cdot 10^{-13}$
PIN480	$1.5 \cdot 10^{-12}$	$1.2 \cdot 10^{-13}$

The device series resistance, R_s, can be calculated from the forward IV curves, using the diode equation:

$$\frac{dV}{dI} \cdot I = I \cdot R_s + \frac{n \cdot k \cdot T}{q} \tag{5.4}$$

Figure 5.11(a) shows the forward IV curve of a typical p-n junction device. For the 100μm-diameter p-n junction device, a series resistance of 95Ω was determined from the slope of the line in Figure 5.11(b). Using the same method, the series resistances of the two PIN260 devices and the PIN480 device used in photon counting measurements were calculated to be 45Ω, 8kΩ, and 50Ω, respectively.

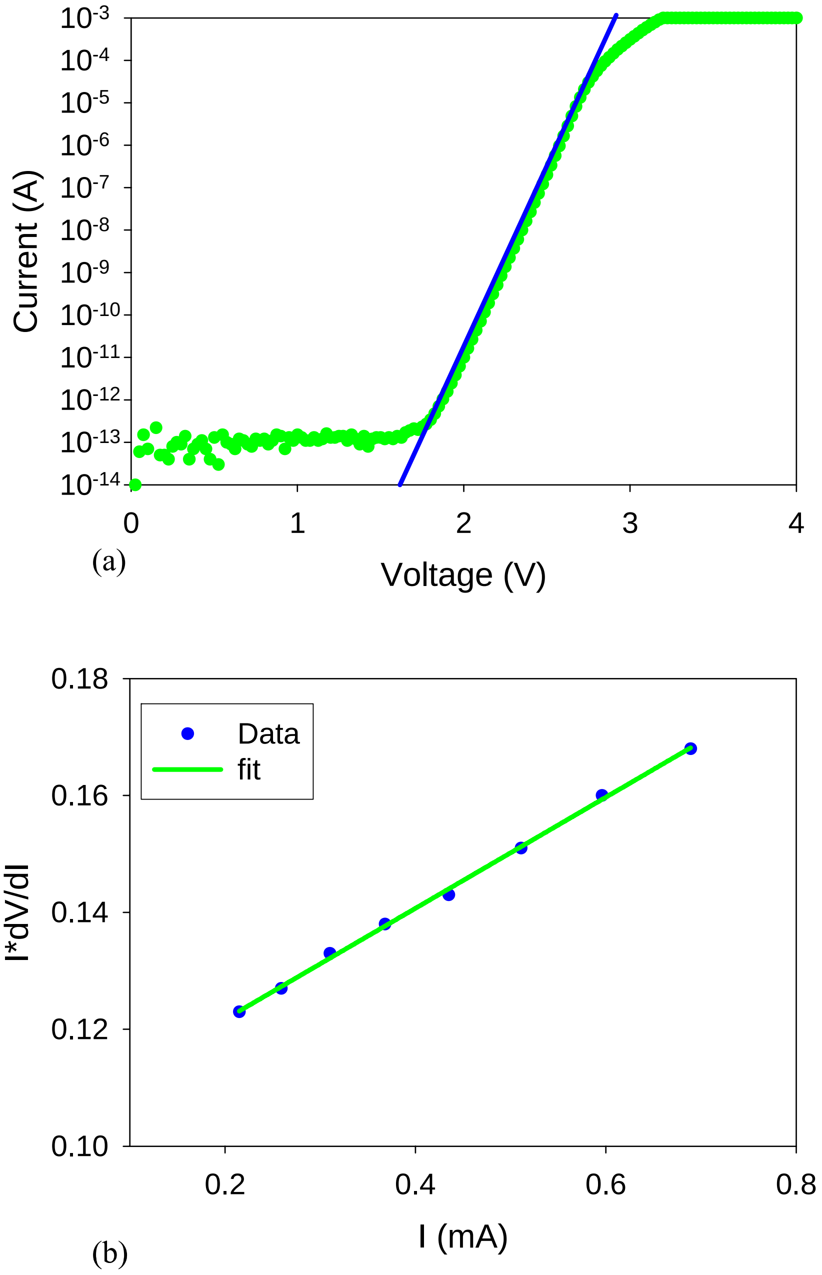

Figure 5.11 (a) Log forward IV curve for a p-n junction device, with an ideality factor 1.95 represented by the blue line. (b) Linear fit of I·dV/dI as a function of current for V=2.85-3.15V. The slope of the line indicates a series resistance of 95Ω.

Capacitance-voltage characteristics were taken with an HP4275 LCR meter at 400kHz and 35V reverse bias. The resulting capacitances for 100μm-diameter devices were 5.3pF, 2pF, and 2.2pF, for p-n junction, PIN260, and PIN480 APDs, respectively. These capacitances included the added capacitance of contact pads, which limit the capacitance at higher voltages. The device RC time constant was calculated from the series resistances and capacitances given above, resulting in RC < 1ns for all but the device with a series resistance of 8kΩ.

5.3 Quantum Efficiency

The quantum efficiency (QE) set-up consisted of a 1kW Xenon lamp as a broadband source output to a SPEX monochromator for wavelength selection in the UV. An Oriel solarization resistant fiber was used to couple the light from the monochromator to the focusing lenses. The light was chopped before the final focusing lens, and the chopper frequency was the reference frequency for the SRS SR850 lock-in amplifier. A UV-enhanced calibrated Si photodiode allowed the conversion of the resulting device photocurrent to responsivity or quantum efficiency as a function of wavelength.

Figure 5.12 shows the quantum efficiency and responsivity as a function of wavelength for all three devices. The peak QE was 38%, 52%, and 42% for the p-n junction, PIN260, and PIN480 devices at peak wavelengths of 266nm, 266nm, and 284nm, respectively. The shift in the PIN480 peak wavelength compared to the other APDs was attributed to increased thickness of the p^+ cap layer.[9] The responsivity shown in Figure 5.12(b) indicated a three order of magnitude rejection ratio for visible wavelengths.

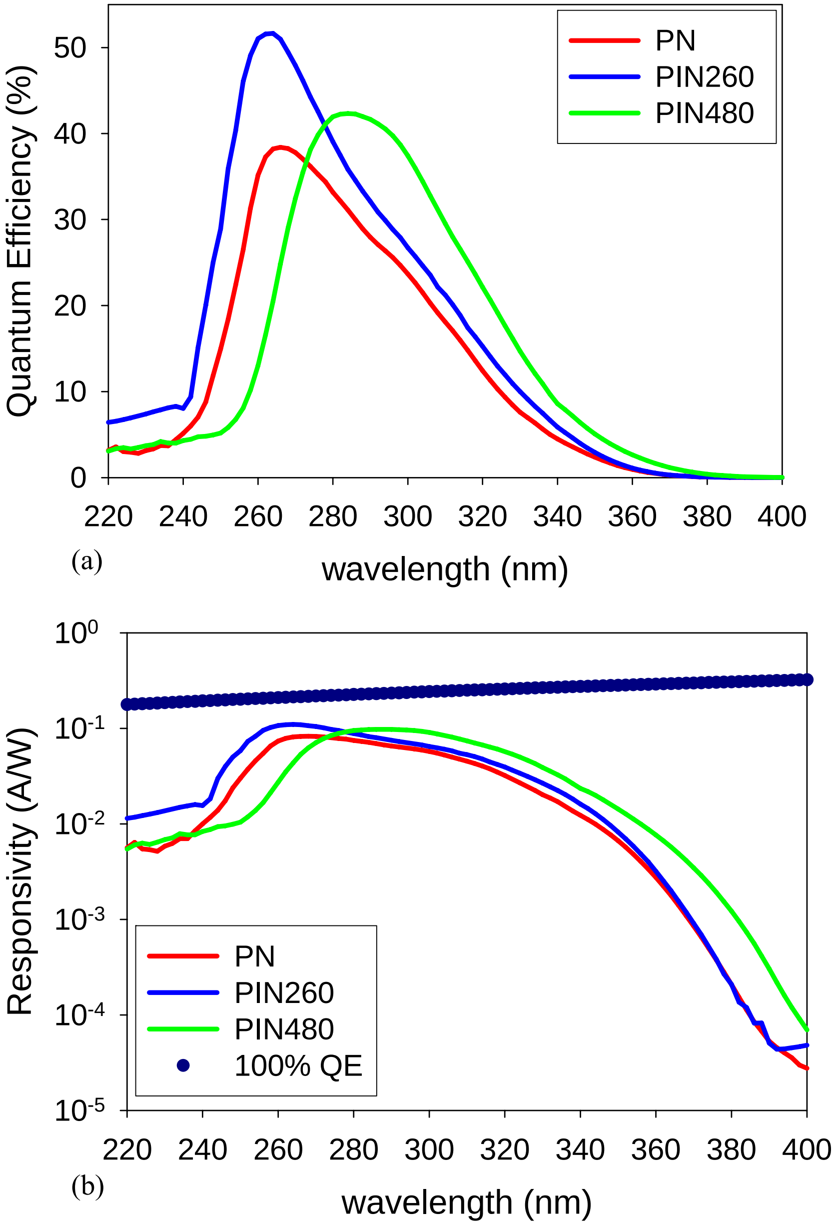

Figure 5.12 (a) Quantum efficiency versus wavelength for p-n junction, PIN260, and PIN480 SiC APDs. (b) Responsivity versus wavelength for p-n junction, PIN260, and PIN480 SiC APDs.

5.4 Raster Scans

Two-dimensional raster scans were taken in order to investigate edge breakdown. The beam of an Argon-ion laser at 351/363nm was focused to an approximately 5μm beam spot through an UV-grade objective mounted on computer controlled micropositioners. The beam was chopped near the source, and the chopper frequency was the reference frequency for the SRS SR850 lock-in amplifier. The micropositioners, controlled by a Newport motion controller, moved the beam spot across the mesa area, generating photocurrent associated with the spatial position of the beam. A Labview program correlated the resulting photocurrent and beam spot location into three-dimensional plots of photocurrent versus x- and y- position. The results of the raster scan experiments will be discussed in detail in Chapter 6.

5.5 Conclusion

Three wafers were used for device fabrication, including p-n junction, PIN260, and PIN480nm structures, and details of the fabrication techniques were discussed. All three structures demonstrated low unity-gain dark current; however, the multiplied p-n junction dark current was an order of magnitude larger than that of the two p-i-n structures. Since higher dark current results in higher dark count levels in Geiger-mode, the p-i-n structures are expected to perform better than the p-n junction. Additionally, the RC time constants were sufficiently low for the typical 4ns to 7ns ac pulses, used in gated quenching single photon counting. The increase in the external quantum efficiency for the p-i-n structures is expected to yield higher single photon detection efficiency for the p-i-n structures compared to the p-n junction structure.

Chapter 6
Gain Uniformity in 4H-SiC APDs

Gain uniformity is an important characteristic to consider in the design of avalanche photodiodes. Non-uniformities in the gain, and thus the field profile, arise from many sources, such as premature edge breakdown, defect related field crowding, contact field crowding, and variations in layer thickness and doping concentration across the wafer.[1-3] Many techniques have been developed to eliminate, or mitigate, the deleterious effect of non-uniformity on photodetector performance.

The first SiC APDs fabricated had mesa structures with nearly vertical sidewalls. Two-dimensional raster scans of the photocurrent revealed non-uniformities in the breakdown characteristics. Of particular concern were sharp peaks around the device perimeter indicating the presence of edge breakdown. Approaches for dealing with non-uniformities resulting from premature edge breakdown include guard rings[4], junction termination extension,[5] multi-step junction termination extension[6], and beveled edge profile.[7] The next section will discuss the implementation of beveled edges in SiC devices, which is the simplest and most appropriate technique for the mesa structure used for our devices. In regard to bulk non-uniformities, Section 6.2 will address the implementation of ring contacts and concentric ring contact devices. Section 6.3 will include observations of non-uniformities as a function of diameter in both p-n junction and p-i-n device structures.

6.1 Edge Breakdown

Figure 6.1 illustrates the relative edge and bulk fields for vertical, positive beveled, and negative beveled sidewalls. In a vertical sidewall mesa, Figure 6.1(a), defects at the surface can lead to a narrowing of the depletion width and higher ionization coefficients.[1,8] Consequently, the surface breakdown field will be lower than the bulk field, leading to premature edge breakdown. Beveled sidewalls employ a sloped sidewall with a shallow angle, θ, the fabrication of which was discussed in Section 5.1.1.

In the case of a positive bevel, the more lightly doped material is closer to the surface, thus the beveling removes more of the lightly doped material than the heavily doped material. When a junction is more heavily doped on one side than the other, the depletion width extends further into the more lightly doped side. Removing more of the lightly doped material forces the depletion region at the edge to extend further into the more lightly doped material in order to compensate for the removed material and maintain charge neutrality. Thus, the depletion width at the mesa edge is thicker than in the bulk, which results in suppression of the edge field, and bulk breakdown precedes edge breakdown.[1-2]

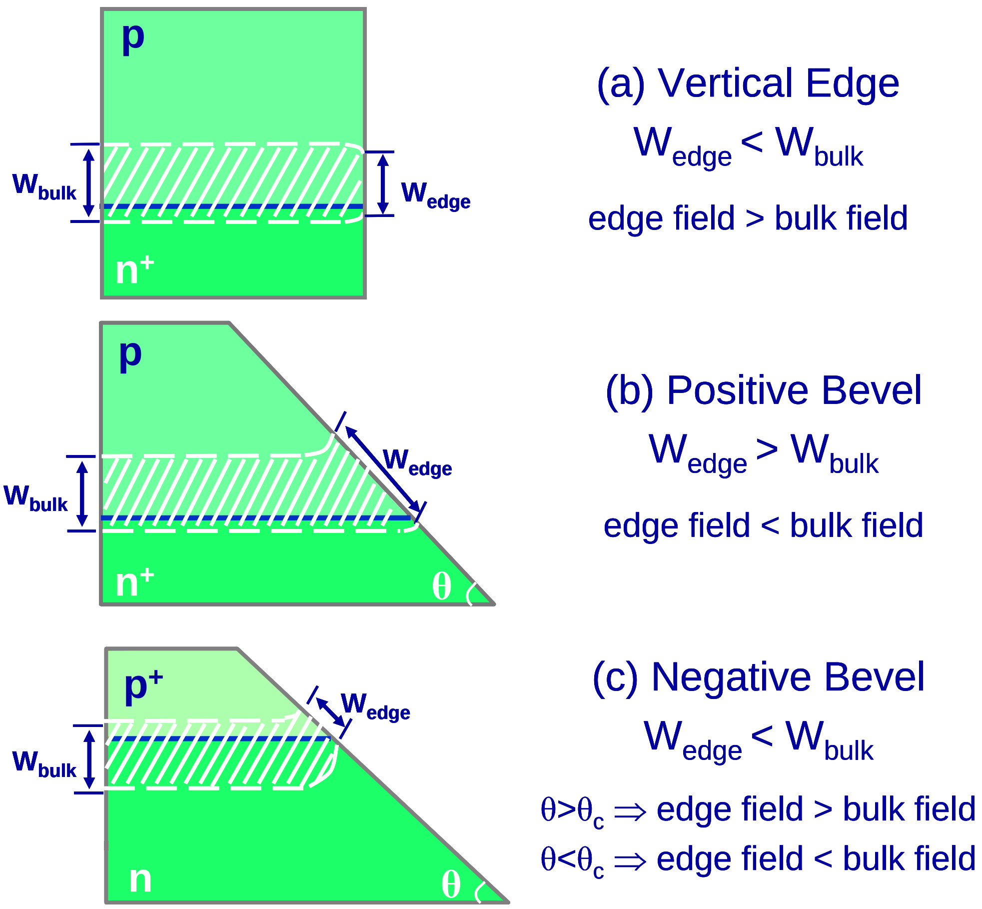

Figure 6.1 Edge profiles for a vertical mesa structure with (a) vertical sidewalls, (b) positive beveled sidewalls, and (c) negative beveled sidewalls.

For the sake of completeness, the negative beveled sidewall case is also included. This case is the inverse of the positive bevel case. Here the more heavily doped material is closer to the top surface, thus more of the heavily doped material is removed during etching. Since the majority of the depletion width extends into the more lightly doped side, the depletion width at the edge is thinner than the depletion width in the bulk, because less charge must be uncovered to maintain charge neutrality. In this case, edge breakdown will precede the bulk breakdown, for angles greater than the critical angle. In order to suppress edge breakdown relative to bulk breakdown, the angle must be less than the critical angle and the junction doping highly disparate.[1]

6.1.1 Device Structure and Processing

Two samples were processed from the p-n junction wafer introduced in Chapter 5, one with vertical sidewalls and another with beveled sidewalls, as shown in Figure 6.2. Non-beveled mesas were defined by reactive ion etching (RIE) using a 5µm-thick photoresist mask baked at 120ºC for 30 minutes, which resulted in a 600nm mesa height. Lithography for the mesa etching of the beveled sample employed an 8µm-thick photoresist mask baked at 150ºC for 30 minutes. The sample was then RIE etched for 100 minutes, resulting in a 1.4µm etch depth. According to a process developed by Yan et al., the bevel angle of a mesa decreases with both higher bake temperatures and longer bake times.[9] This is due to the fact that higher and longer bake temperatures change the shape of the photoresist mesa from straight sidewalls to a rounded dome shape, as discussed in Section 5.1.1. The beveled sample had a bevel angle between 5-10˚, as measured with a calibrated Olympus microscope at 80X magnification, while the non-beveled device showed no discernible bevel angle, indicating approximately vertical sidewalls, as illustrated by Figure 6.2. In both cases, the mesas were 160µm in diameter and an SiO_2 passivation layer grown by PECVD followed etching. The n and p contacts were different metals, but transfer length method (TLM) measurements indicated no difference in the electrical characteristics of the contacts on the two samples.

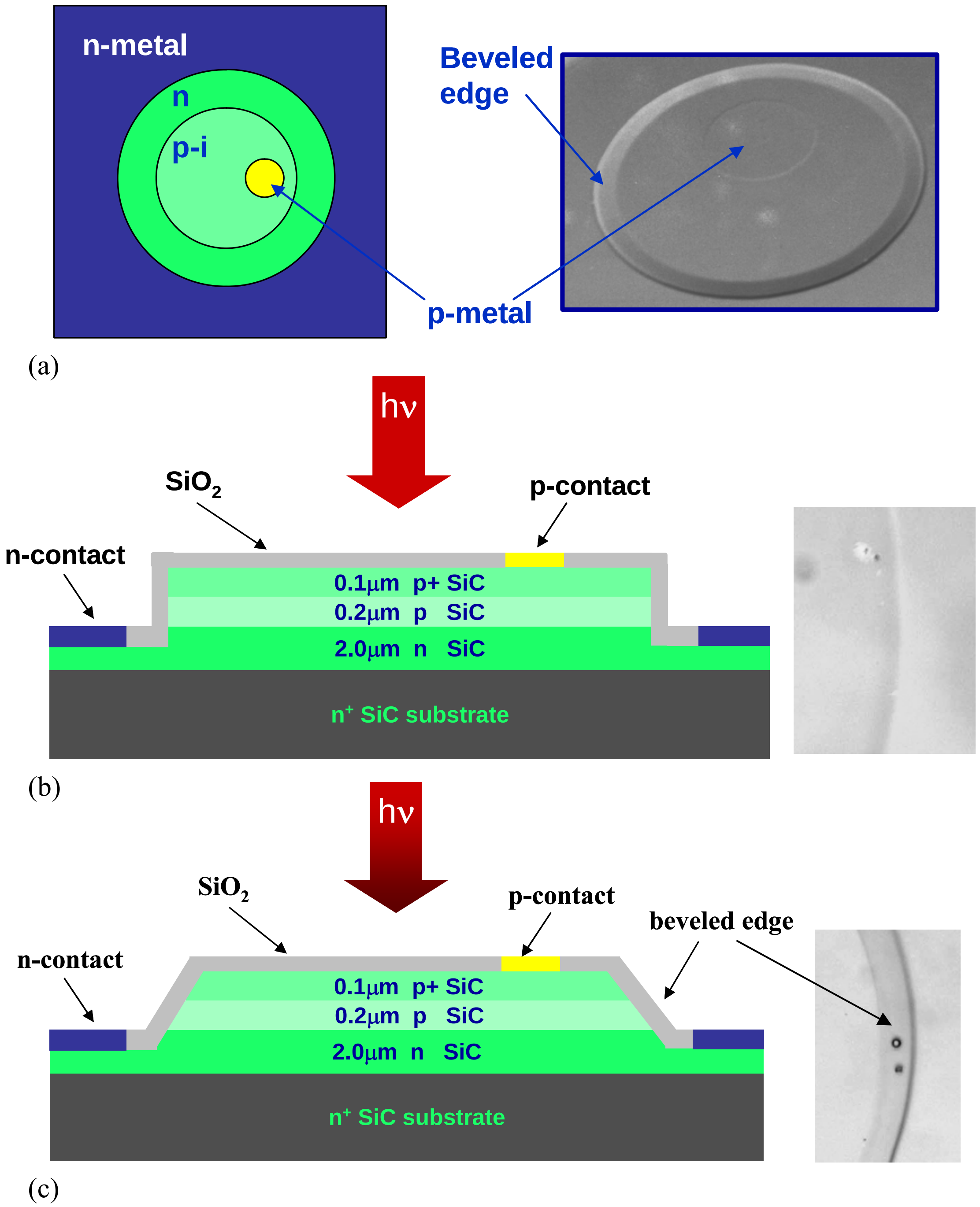

Figure 6.2 (a) Top down view of device structure and SEM of a beveled edge device. Device cross-section and photo of device edge for (b) non-beveled device and (c) beveled device.

6.1.2 Current –Voltage Characteristics

Figure 6.3 shows the IV characteristics for both beveled and non-beveled devices. At low bias voltages, both devices demonstrated low dark currents (~1pA). The dark current in the non-beveled device began to rise at ~29V reverse bias, increasing more

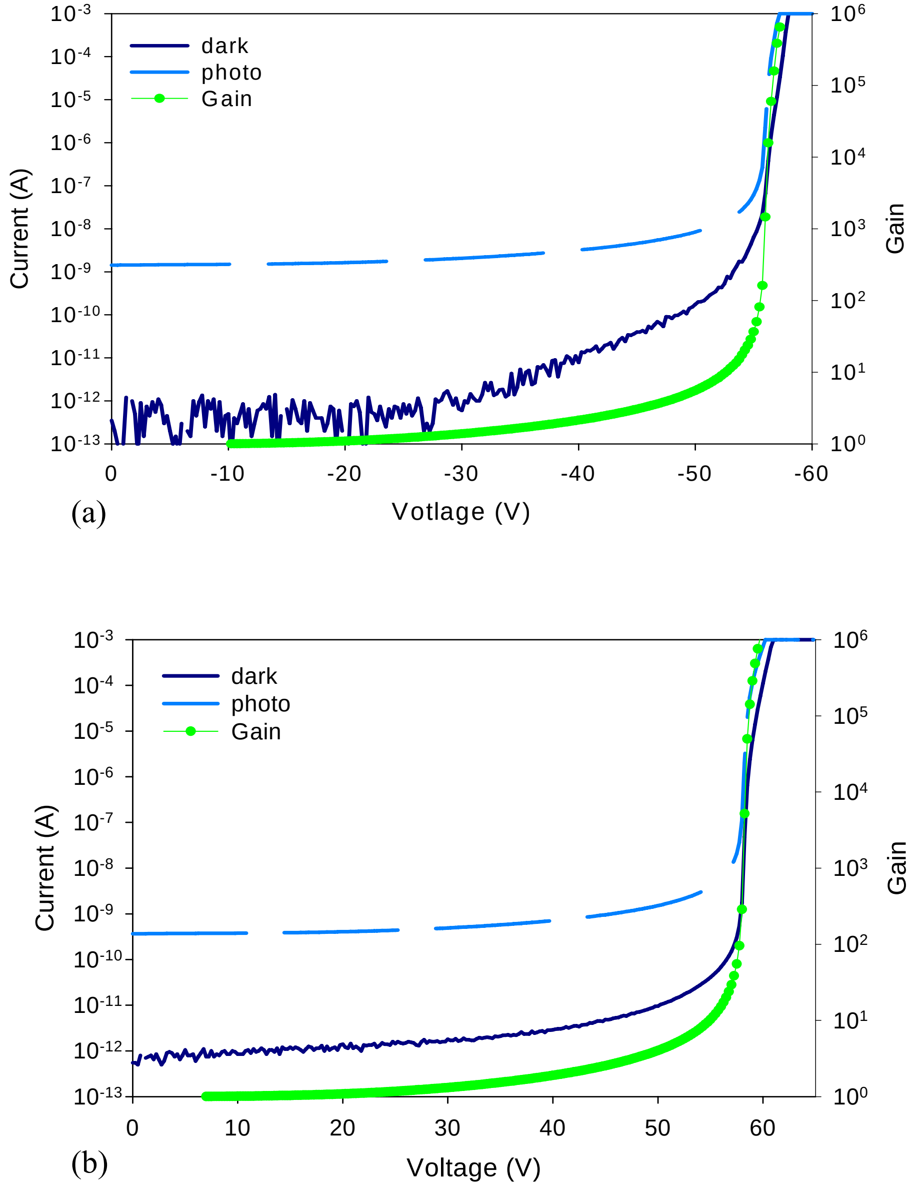

Figure 6.3 IV and gain characrteristics for (a) non-beveled and (b) beveled SiC APDs under broad band UV illumination.

than two orders of magnitude at the onset of avalanche gain. Dark current in the beveled device remained relatively flat until the onset of avalanche gain. In both devices, the photocurrent was flat with little dependence on bias voltage prior to the onset of avalanche multiplication. The breakdown voltages were 57V and 60V for the non-beveled and beveled devices, respectively. The lower breakdown voltage of the non-beveled device compared to the beveled device was consistent with premature edge breakdown.

6.1.3 Raster Scans

In order to investigate edge breakdown, two-dimensional raster scans of both device geometries were taken using the method described in Section 5.4. The micropositioners scanned the device area at 5µm by 5µm resolution, resulting in three-dimensional plots of photocurrent versus x- and y- position. Raster scans taken at unity-gain (5V reverse bias) show a flat, uniform response across the device area, for both the non-beveled and beveled devices. The unity-gain photocurrent was then attenuated to 1nA. The gain for subsequent scans was determined by increasing the voltage to yield a photoresponse in nanoamperes equivalent to the gain, i.e. a photoresponse of 50nA corresponds to a device gain of 50. Both the non-beveled and beveled devices required the same level of attenuation at the same laser power to achieve a 1nA photoresponse at 5V reverse bias. This indicated equivalent quantum efficiencies in both devices, which was confirmed from QE measurements. Figure 5.12 showed the spectral response of the p-n junction devices.

Figures 6.4(a) and (b) show the raster scans for the non-beveled device at gains of 50 and 130, corresponding to reverse bias voltages of 55.1V and 55.7V, respectively. At a gain of 50, edge breakdown began around the front half of the device, farthest from the contact, as shown in Figure 6.4(a). The sharp peaks at (x,y) ~ (75,100) were attributed to localized field crowding around defects. A number of devices were measured from each sample, and all of the devices showed similar localized gain non-uniformity at various locations across the device mesa. This suggests that the peaks were related to local defects and defect densities on the wafer. At a gain of 130, edge breakdown was clearly present around the entire device perimeter. The increased response occurring behind the contact, at the device edge, resulted primarily from contact field crowding, which will be discussed in Section 6.2.

The beveled device showed no evidence of edge breakdown at gains of 50 and 130, corresponding to reverse bias voltages of 57.32V and 57.84V, respectively, as illustrated in Figures 6.4(c) and (d). At a gain of 130, surface non-uniformities do appear, but they occur over the area of the device rather than at the device edge, thus they were not indicative of edge breakdown. The gradual rise in photoresponse in the y-direction in Figure 6.4(b) and in the x-direction in Figure 6.4(d) resulted from a variation in doping density across the wafer.[3,10]

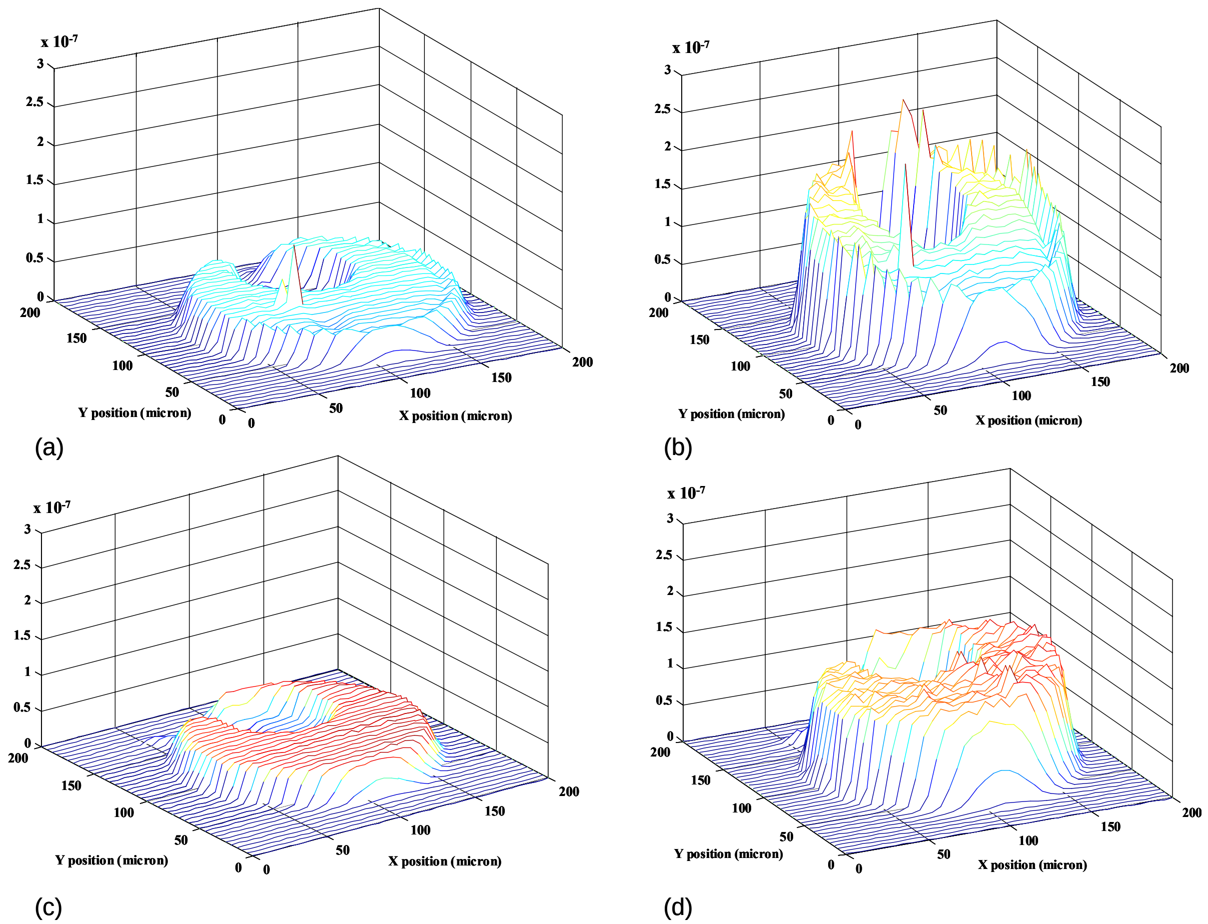

Figure 6.4 Two-dimensional raster scan measurements of a non-beveled edge device at a gain of (a) 50 and (b) 130, corresponding to reverse bias voltages of 55.1V and 55.7V, respectively, and a beveled edge device at a gain of (c) 50 and (d) 130, corresponding to reverse bias voltages of 57.32V and 57.84V, respectively.

Figure 6.5 shows a scan of the beveled device at 58.18V reverse bias, corresponding to a gain of ~10^3 at (x, y) = (100, 100). The high gain measurement was limited by the 1μA compliance of the SRS SR850 lock-in amplifier and required the insertion of a 20dB attenuator at the lock-in amplifier input. Thus, in order to read the gain directly from the raster scan, the photocurrent must be multiplied by 100. The non-beveled device was too unstable to scan at comparably high gains. The non-uniformity in the breakdown of the beveled device increased dramatically between the device contact and edge, where the contact was closest to the device edge. This non-uniformity resulted primarily from field crowding, as in the case of the non-beveled device in Figure 6.4(b), and obfuscates the highest gains attainable by these devices. Contact field crowding will be discussed in the next section.

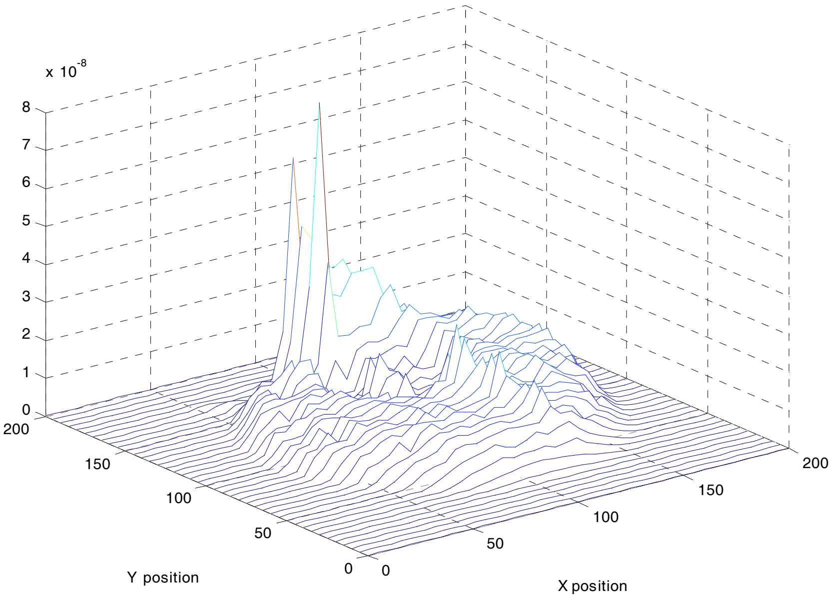

Figure 6.5 Two-dimensional raster scan measurement of a beveled edge device at a gain of 10^3, corresponding to a reverse bias voltage of 58.18V.

6.2 Contact Geometry

While beveled edges mitigated edge breakdown, they did not resolve non-uniformities across the mesa area, particularly the sharp peaks behind the contact in Figures 6.4(b) and 6.5. These sharp peaks were most likely the result of field crowding around the contact. This can occur from either lateral resistance, which hampers the uniform spreading of the field across the mesa, or contact placement close enough to the device edge that edge breakdown or oxide breakdown occurs. Eliminating field crowding in the device is critical to photon counting performance in Geiger-mode.

6.2.1 Device Structure and Processing

This study compared the gain uniformity of a 100µm-diameter mesa device with a 150Å Ti semitransparent ring contact, as shown in Figure 6.6, and a 100µm-diameter mesa device with an off-centered dot contact, as shown in Figure 6.2(a) with the addition of a Ti/Au probe pad. Both devices were processed from the p-n junction wafer described in Chapter 5. For the ring contact device a small via was opened over the p-contact to connect the probe pad, leaving the majority of the semitransparent ring contact under the SiO_2 antireflection coating, as shown in Figure 6.6. Typical linear-mode IV curves and the quantum efficiency were the same as those for the devices in Section 6.1, though the breakdown voltage differs slightly across the wafer. A number of semitransparent contacts covering the entire mesa were also investigated with the aim of improving the gain uniformity; however, a small uncovered area around the perimeter of the contact resulted in higher photocurrent due to misalignment during photolithography. The higher photoresponse was not differentiable from edge breakdown in many cases, thus a self-aligned process is necessary for successful implementation of this technique.

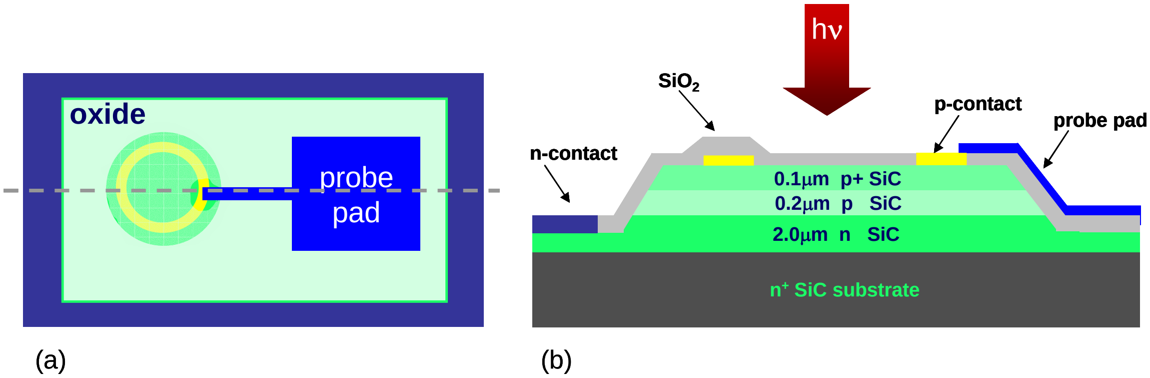

Figure 6.6 (a) Top down view of ring contact device and (b) cross-section showing beveled edge and ring contact.

6.2.2 Raster Scans

Two-dimensional raster scans of both contact geometries were taken with a spot size in the range of 3-5μm. Figure 6.7 shows the resulting scans as contour plots of photocurrent versus position. The scans taken at unity-gain for both devices showed a flat, uniform response across the mesa, with the exception of the contact area. The dot contact and probe pad connecting bar reflected the light, resulting in no response in the contact area, as shown in Figure 6.7(a). The semitransparent ring contact in Figure 6.7(c) appeared as a light orange ring, due to the light being only partially reflected. As in the case of the dot contact device, the probe pad-connecting bar reflected the light resulting in no response under the contact. Figures 6.7(b) and (d) show contour plots of the photocurrent at a gain of 10^3. The ring contact device exhibited far greater spatial uniformity. The remaining non-uniformity of the mesa area manifested as a gradual rise in photocurrent toward (x, y) = (30, 35), most likely resulting from the dopant concentration increasing in this direction, as discussed in References [3] and [10].

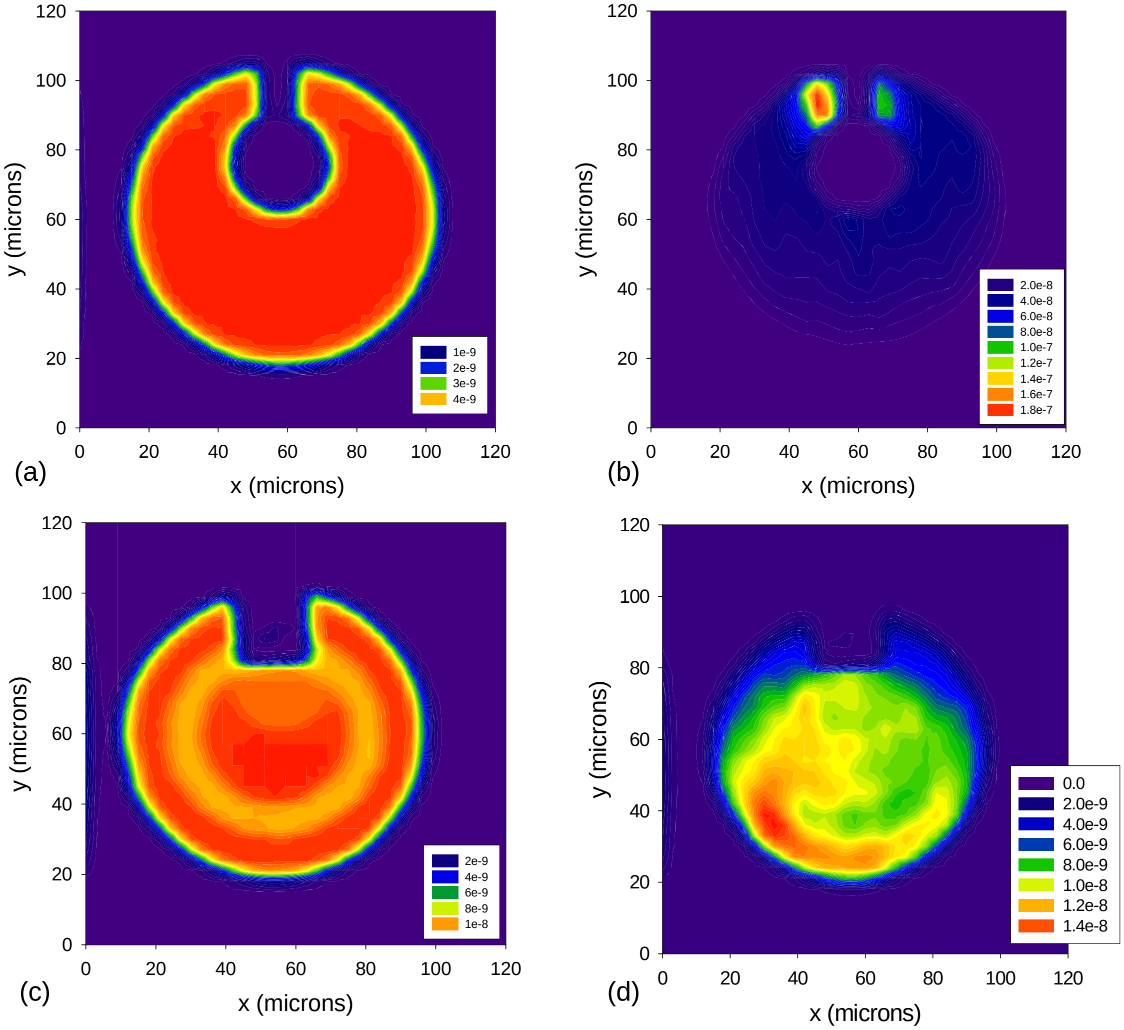

Figure 6.7 Contour plots of 2D raster scans for (a) dot contact device at 10V unity-gain, (b) dot contact device at a gain of 10^3 at 53.44V, (c) ring contact device at 10V unity-gain, and (d) ring contact device at a gain of 10^3 at 53.12V. Both devices had a 100µm-diameter.

Concentric ring contacts were also studied as an approach for improved gain uniformity across larger area mesa devices. Figure 6.8 shows the contour plots of raster scans for a 160µm-diameter semitransparent concentric ring contact device. Just as in Figure 6.7(c), the light orange on the mesa in Figure 6.8(a) resulted from the partial reflection of the incident light. While these concentric ring contacts showed some improvement in uniformity for 160µm-diameter devices, the ring contacts on a 100µm-diameter device resulted in significantly more uniform gain across the mesa.

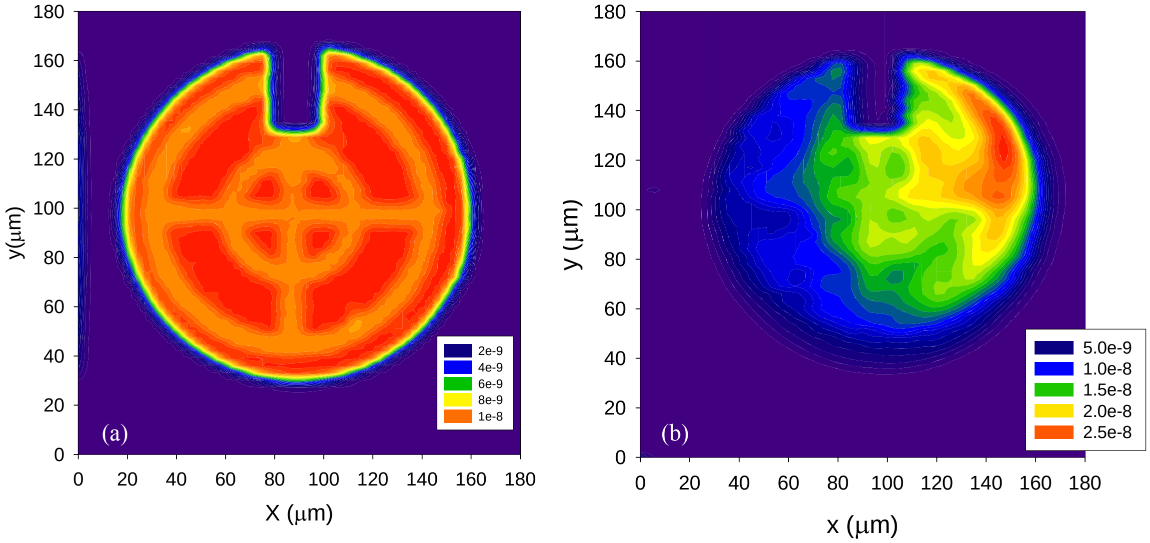

Figure 6.8 Contour plots of 2D raster scans for a 160µm-diameter concentric ring contact device at (a) 10V unity-gain, and (b) a gain of 10^3 at 52.86V.

6.3 Gain Uniformity and Diameter

The two primary sources of bulk non-uniformities in SiC are doping profile variation and material layer thickness variation. Both the doping and layer thickness increase radially from the center of the wafer.[3,10] Thus p-n junction devices, which have no i-region, should experience improved gain uniformity as mesa diameter decreases[12], since the non-uniformity results primarily from doping variation. The 100µm- and 160µm- diameter devices in Figures 6.7(d) and 6.8(b), respectively, support this conclusion, since the 100µm-diameter device was much more uniform than the 160µm-diameter device, even though the larger area device had a higher percentage of contact coverage in order to overcome lateral resistance and contact field crowding.

Raster scans of APDs of varied diameters fabricated on the PIN260 wafer showed the opposite behavior, with smaller area devices being less uniform than larger area devices. Figure 6.9 shows the raster scans from four devices of 50μm, 70μm, 100μm, and 150μm diameter, at a gain of 10^3. These devices were located close to each other on the wafer, and serendipitously oriented to the direction of material parameter variation such that the slope of the photocurrent was easily attained. An additional set of devices from another sample of the PIN260 wafer demonstrated the same relationship between gain uniformity and diameter.

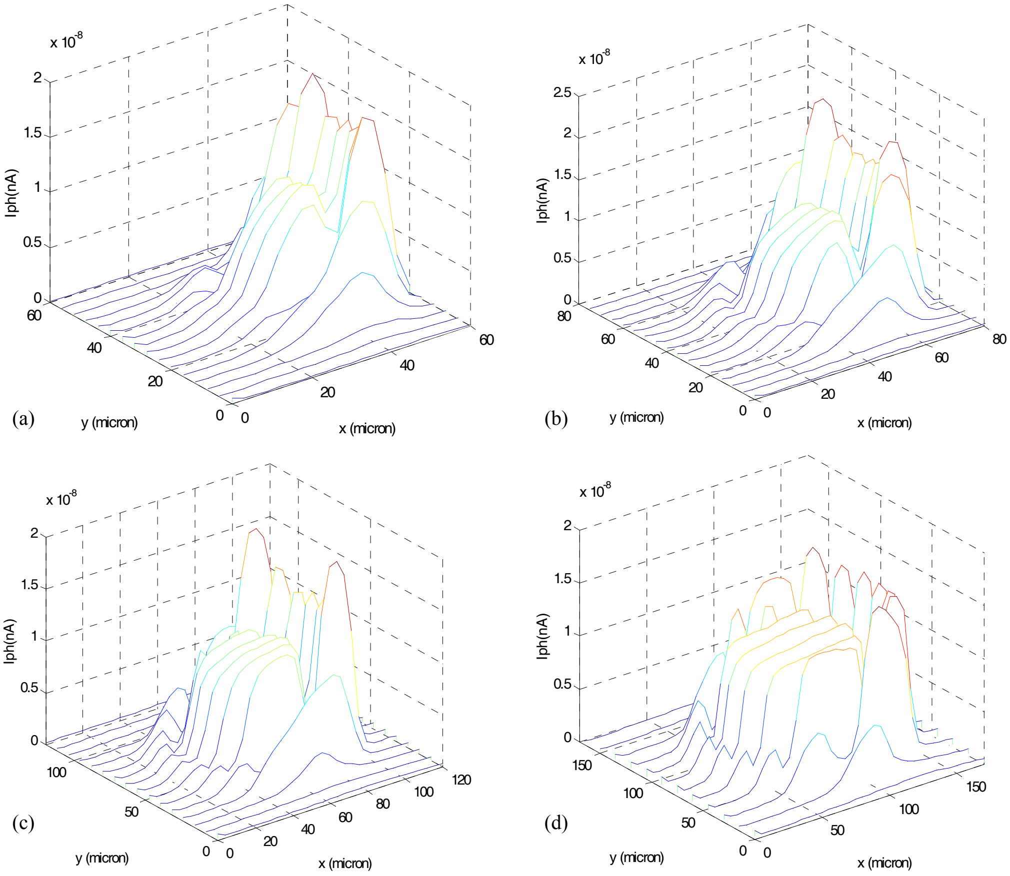

Figure 6.9 Raster scans of 4H-SiC APDs of varying diameter at a gain of 10^3, including a (a) 50μm-diameter device at 108.38V, (b) 70μm-diameter device at 108.37V, (c) 100μm-diameter device at 107.94V, and (d) 150μm-diameter device at 108.1V.

Figure 6.10 shows the slope of the photocurrent versus y-direction as a function of device diameter. A higher slope in the photocurrent indicates increased non-uniformity, thus smaller diameter devices clearly suffered more non-uniformity than larger diameter devices, though the effect appears to saturate for larger diameters. Increasing non-uniformity with decreasing slope was contrary to expectations for these devices.

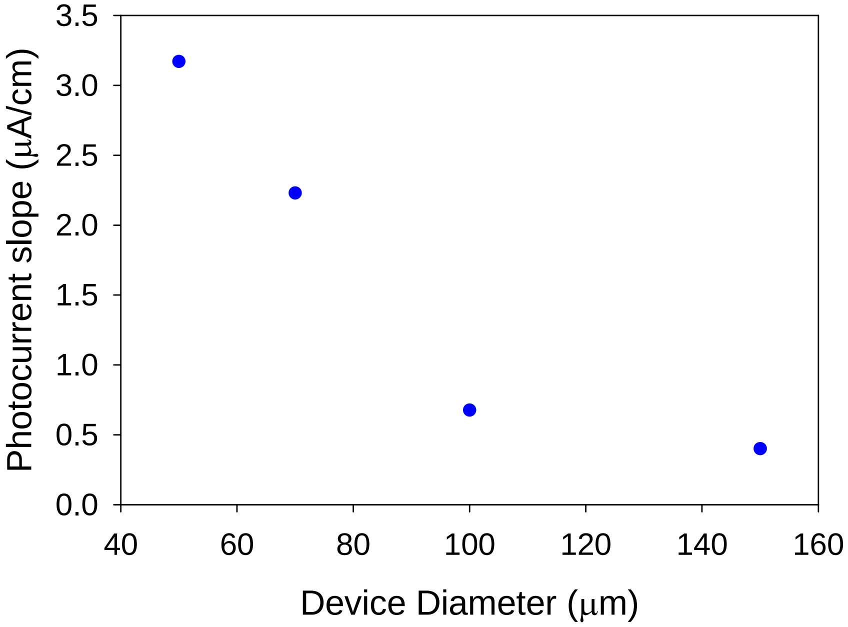

Figure 6.10 Slope of the photocurrent versus y-direction as a function of device diameter.

The increase in doping outward from the wafer center leads to a reduction in the depletion width in the same direction, which results in an increase in the electric field, lowering the breakdown voltage. The material layer uniformity also increases outward from the wafer center, which increases the thickness of the avalanche region in same direction, lowering the electric field and increasing the breakdown voltage. These two mechanisms oppose each other, presumably reducing the non-uniformity of the PIN devices compared to the p-n junction devices. However, Cree reports a 5% doping variation and only a 1% thickness variation[3], indicating that the doping non-uniformity should still be the dominant mechanism of non-uniformity in PIN devices. Furthermore, the compensative effect of the i-layer variation should not be sufficient to reverse the behavior seen in the p-n junction devices. Thus, the smaller diameter devices should experience a smaller variation in material parameters leading to improved uniformity. The fact that they do not warrants further examination as increased uniformity improves the single photon counting performance, particularly the reduction in bulk dark current with decreasing diameter.

6.4 Conclusion

Edge breakdown in SiC APDs was suppressed by employing a sidewall bevel angle <10°. These devices exhibited low dark currents, <10pA for a 160µm-diameter device, at the onset of avalanche gain. Two-dimensional raster scans of both beveled and non-beveled devices fabricated from the same wafer show the photocurrent as a function of position, illustrating the spatial properties of avalanche gain in SiC APDs.

An additional concentric ring contact device with a mesa diameter of 160µm was also measured. While this device showed improved uniformity compared to the dot contact geometry, neither device was more uniform than the 100µm-diameter ring contact device. Thus, we selected the dot contact device for ease in coupling and the ring contact device for uniformity for the single photon counting experiments with p-n junction APDs, discussed in the next chapter.

Chapter 7

Single Photon Counting p-n Junction Avalanche Photodiodes

SiC has many attributes indicative of good single photon counting performance, such as very low dark current, a high ratio of hole to electron ionization coefficients, high thermal conductivity, and the ability to sustain high electric fields.[1-2] We began our study of 4H-SiC APDs as single photon detectors with passive quenching of a 160μm-diameter APD with an off-centered dot contact. The dark count rate for these devices was in the high hundreds of kHz to a few MHz, which prompted an investigation of the low temperature gated quenching behavior of p-n junction SiC APDs.

In the previous chapter, the spatial uniformity of ring and dot contact devices was investigated. Those same devices were used in single photon counting experiments to compare the difference in performance between two devices with very different spatial field profiles. Finally, improvements were made to reduce the noise level of the experimental set-up and the single photon counting measurements were repeated.

7.1 Low Temperature Photon Counting

7.1.1 Linear-mode

The device used for the low temperature measurement was a 160μm-diameter dot contact APD fixed on a TO header and mounted inside a cryostat. The device had Ni/Au probe pads, so that the wire bonds would stick to the device contacts. An AlN pad was placed between the device substrate and header for electrical isolation as well as good thermal conduction. The RC time constant of the device was approximately 1ns prior to wire-bonding. The wire-bonds increased the parasitic capacitance of the device and, consequently, the response time.

Figure 7.1 shows the IV characteristics of this device both in the cryostat at 77K and outside the cryostat at room temperature. The TO header was soldered directly to the gated quenching circuit and mounted inside the cryostat. Thus, the IV characteristic at 77K was measured in series with the 33kΩ load resistor in the quenching circuit. The current began to roll over in response to the load resistor at 57V. Previous low temperature IV characterization revealed a 5mV/K temperature coefficient for 4H-SiC. Accordingly, the breakdown voltage was only expected to differ by approximately 1V between room temperature and 77K.

The dark current at 77K was almost an order of magnitude lower than that at room temperature; however, in order to see photo counts in Geiger-mode the device was biased at voltages greater than 58V. At voltages that high, there was little difference between the dark current at 77K and room temperature, which was attributed to tunneling current dominating the dark current in the p-n junction APD.[3]

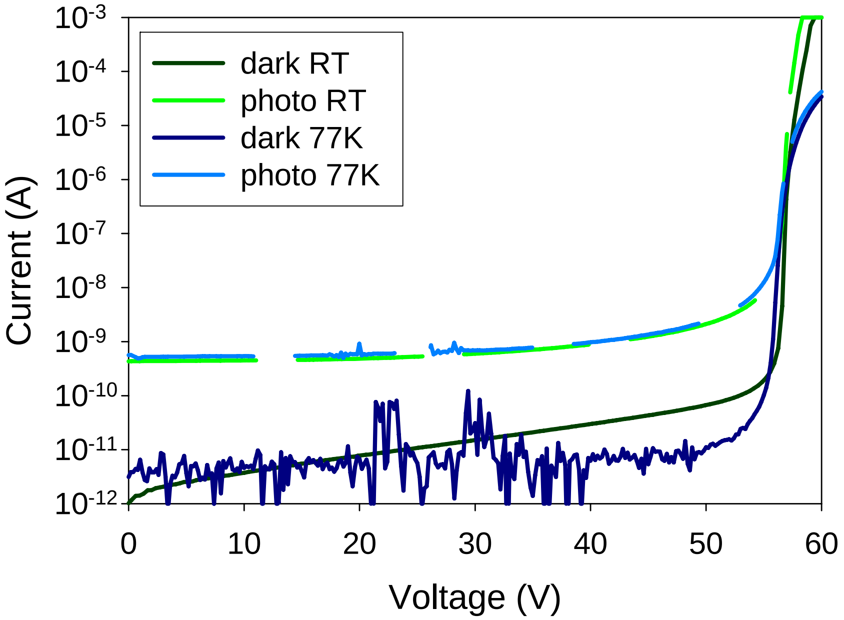

Figure 7.1 IV characteristic of a 160μm-diameter dot contact SiC APD at room temperature and at 77K. The 77K characteristics were taken through the 33kΩ resistor in the quenching circuit.

7.1.2 Experimental Set-up

The device was measured using the experimental set-up in Figure 3.4(b) in conjunction with a cyrostat[4] using a 266nm Nd:YAG laser. The device was cooled to 77K using liquid nitrogen. Measurements were taken at average photon number levels of nbar = 0.44, 0.84, 1.4, 46, and 224 photons per pulse. The APD was dc biased through a 33kΩ resistor and pulse-biased above breakdown through a 100nF capacitor using an Agilent 81110A pulse generator with a 3.8V pulse height for 5ns at a 7.5kHz repetition rate. The output pulses were discriminated and counted using an SR400 photon counter from Stanford Research Systems. The detection gate length was 6ns and triggered by the ac pulse generator. The fast rise and fall times of the ac pulse generated capacitive transients at the output, which were cancelled using matched 50Ω coaxial cables.[5] The discriminator voltage was determined by minimizing the noise equivalent power (NEP) with respect to discriminator voltage, as detailed in Reference [4].

7.1.3 Geiger-mode

The self-sustaining avalanche process is not limited to photo-generated electron-hole pairs, hence the dark counts must be minimized. Dark counts originate from three primary sources: thermal generation-recombination, tunneling, and afterpulsing. Thermal generation-recombination is minimal in a wide band gap semiconductor such as SiC. Tunneling dark current is primarily dependent on temperature through the band gap dependence on temperature, which in SiC is small. Thus, we expect to see little change in the tunneling current contribution at lower temperatures. Afterpulsing, on the other hand, tends to be worse at lower temperatures. In afterpulsing, charge flowing through the junction becomes trapped in trapping centers. These carriers may be emitted during subsequent pulses and initiate a dark count. The contribution of afterpulsing increases with bias voltage and is frequency dependent on the trap lifetime. Since the trap release time is longer at lower temperatures, lower repetition rates may be required in order to give the traps sufficient time to discharge before the next ac pulse.[6-7]

Dark counts were taken as a function of frequency and dc bias voltage, as shown in Figure 7.2, using the internal trigger of the pulse generator. The frequency ranged from 100Hz to 500kHz, while the voltage ranged from 58.5V to 60V. The device showed no dependence on frequency from 100Hz to 500kHz, thus afterpulsing was negligible at the measurement frequency.

The maximum excess bias ratio, V_E/V_{Br}, was 0.04, where the excess bias is defined as

$$V_E = V_{AC} + V_{DC} - V_{Br} \tag{7.1}$$

The excess bias was fixed by the 3.8V maximum pulse height of the pulse generator. The breakdown voltage, approximately 60V, was defined as the voltage at which the current reached 100μA when measured through the circuit. Ng et al. calculated that the breakdown probability of a 2μm i-region 4H-SiC APD should be almost 80% for a 4% excess bias ratio.[8] The probability is expected to be much lower for a p-n junction device, as discussed in Chapter 2.

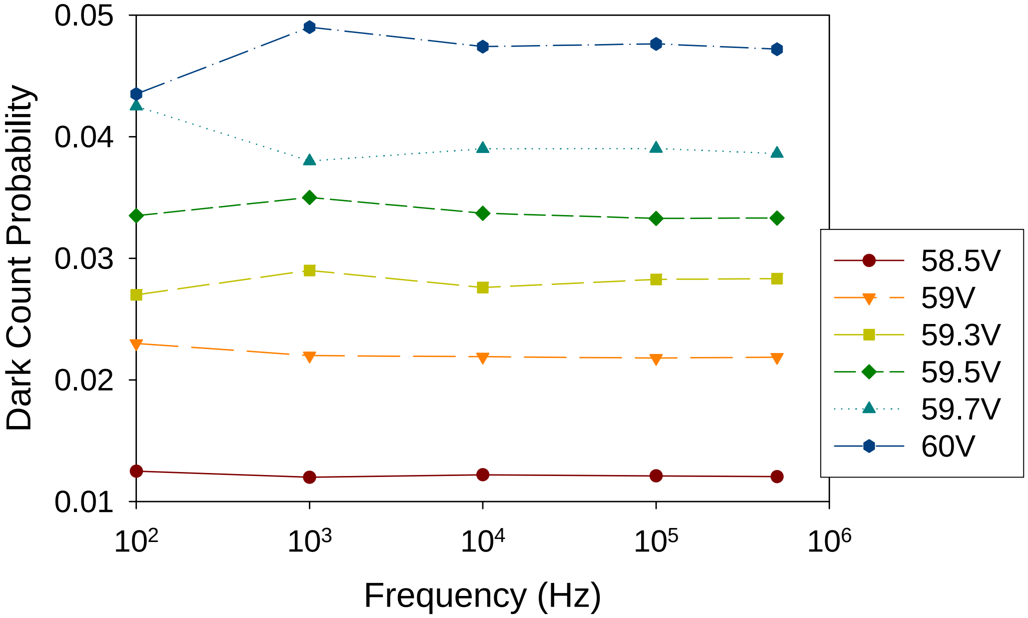

Figure 7.2 Dark count probability versus frequency for a 160μm-diameter dot contact SiC APD at 77K.

Figure 7.3 shows the single photon detection efficiency versus dark count rate for average photon numbers of nbar = 0.44, 0.84, 1.4, 46, and 224 photon per pulse. The single photon detection efficiency (SPDE) was calculated using equation (3.2). The dark count rate, R_D, was calculated according to

$$R_D = \frac{N_D}{f \cdot t_g \cdot t} \tag{7.2}$$

where N_D is the total number of dark counts, f is the repetition rate, t_g is the detection gate width, and t is the integration time. The equation used to calculate the total count probability was

$$P_T = 1 - e^{\frac{-N_T}{f \cdot t}} \tag{7.3}$$

where N_T is the total number of counts with the laser on. This equation differs from the one discussed in Chapter 3 in order to account for using an average photon number greater than one.[9-10]

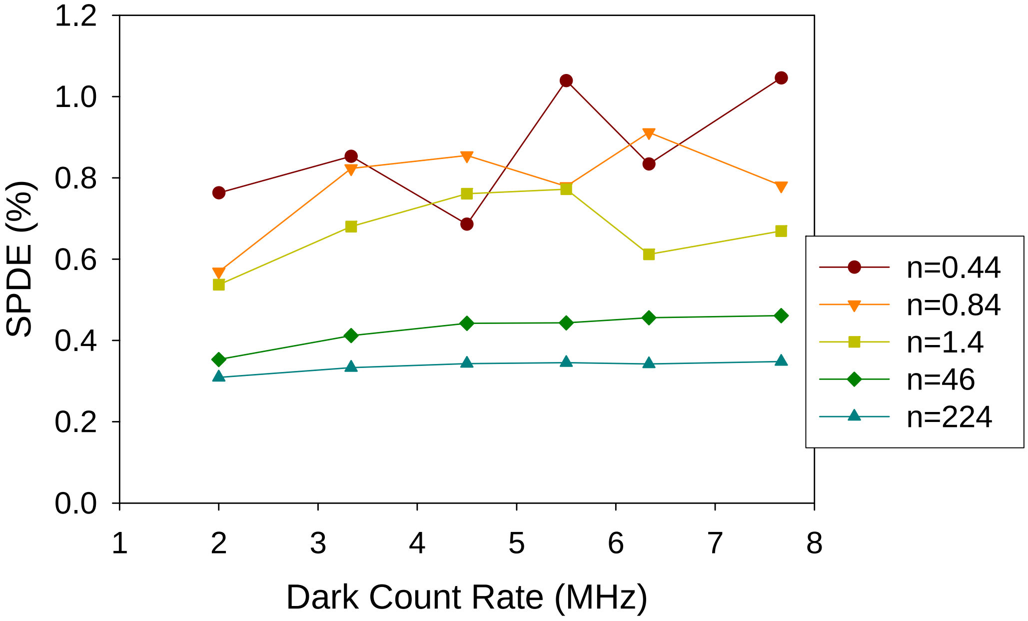

Figure 7.3 Single photon detection efficiency versus dark count rate for an average photon number of nbar = 0.44, 0.84, 1.4, 46, and 224 at 77K. The dc bias voltage was 58.5 – 60V with a 3.8V ac bias pulse height.

The SPDE achieved with higher average photon numbers was lower than for lower photon numbers, which makes sense given that the device will count only once per detection gate. The higher average photon numbers were used because the difference in total counts and dark counts was approximately one standard deviation for nbar < 1 photon per pulse. For nbar = 1.4 photons per pulse the difference in total counts and dark counts was approximately two standard deviations, while nbar ≥ 46 photons per pulse resulted in a difference of many standard deviations. Thus, using a higher number of photons confirmed that the device was performing at a SPDE ≤ 1%. The dark count rate for these measurements ranged from 2MHz to 8MHz, which corresponded to a dark count probability of 1% to 5%. At room temperature the dark count rate ranged from 4MHz to 10MHz for the same bias conditions. Thus, at 77K the dark count rate remained prohibitively high and was not significantly reduced, especially for such low detection efficiency.

7.2 Gain-Uniformity in Single Photon Counting

Despite many efforts, including cooling the APD to 77K, the dot contact device did not achieve single photon counting operation. This was likely attributable to the large spatial non-uniformity, which indicated that the majority of the mesa area was not biased above the breakdown voltage and was not operating in Geiger-mode. Only the two "hot spots" behind the dot contact were actually in Geiger-mode, such that a photon incident on the center of the mesa would initiate very few, if any, self-sustaining avalanche events. Alternatively, the dark carriers were generated throughout the bulk. Kang et al.[11]

developed a model for calculating the number of dark carriers present based on the number of seed carriers available. A seed carrier is defined as a carrier with the potential to initiate a self-sustaining avalanche pulse. Two of the sources of seed carriers included direct contributions from the dark current. One of these contributions comes from the dark current injected or generated in the active region during the ac pulse; the other accounts for carriers multiplied by the dc field that are still present in the junction at the time the ac pulse is applied. Thus, the dark carriers can take advantage of the high field in the hot spots, even if the photo-carriers cannot.[12] Since the dot contact device did not achieve single photon counting, the experiments were continued with only the ring contact device.

7.2.1 Linear-mode

The ring contact SiC APD was processed from the p-n junction wafer described in Chapter 5. The 100μm-diameter mesa device had a semitransparent ring contact and beveled edges to mitigate edge breakdown.[1,13]

The linear-mode gain was approximately $5x10^6$ at a reverse bias voltage of 55V. The dark current at unity-gain, 10V, was ~1pA, while at a gain of 10^4 the dark current was ~200nA. Typical linear gain IV curves for a p-n junction APD can be found in Figure 6.3(b), though the breakdown voltage differs slightly across the wafer. The linear-mode gain as a function of voltage was taken with diffuse broad-band illumination and a focused 325nm laser spot. The laser was aligned in the same way as in the photon counting measurements to indicate the difference in the gain of an incident photon versus the gain of the average dark carrier. Figure 7.4 shows that for gains greater than 10^4 the focused gain diverged from the diffuse gain by almost an order of magnitude. This indicated that the average gain, which corresponds to the electric field, seen by a dark carrier could be greater than an order of magnitude higher than the field seen by the incident photons under Geiger-mode operation.

A HeCd laser operating at 325nm was utilized for these measurements. At 325nm the external quantum efficiency of the p-n junction APD was 10%. The capacitance of the 100μm-diameter ring contact device with a 75μm x 75μm probe pad was 5.3pF. The series resistance was 95Ω yielding an RC time constant of 0.5ns. An RC time constant as short as possible is essential for reducing the recovery time for passive quenching and the gate length for gated passive quenching. Reducing the gate length helps to minimize the dark counts, because the photon counter only records counts when the detection gate is open.

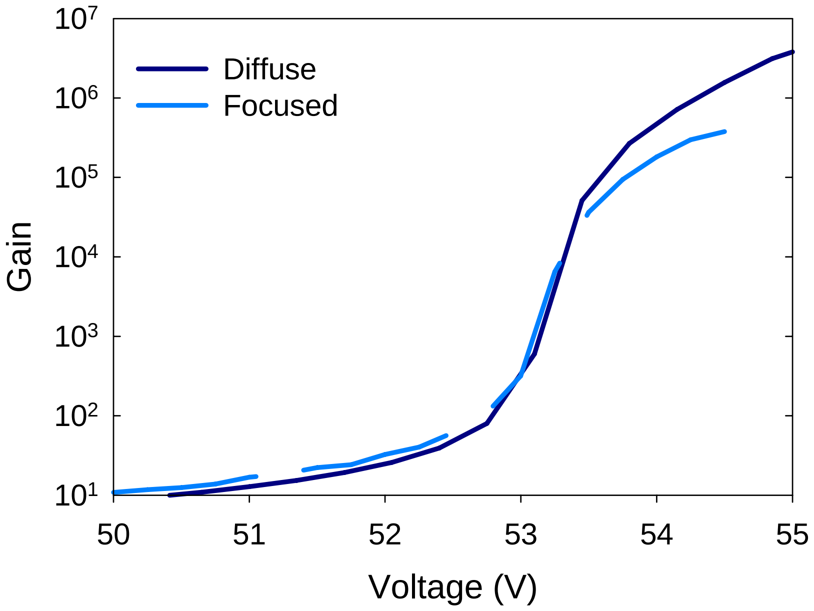

Figure 7.4 Gain-Voltage characteristic under diffuse UV and focused 325nm light.

7.2.2 Experimental Set-up

Both devices were measured using the photon counting setup in Figure 3.2 and a gated quenching circuit.[5,10] The APDs were dc biased through a 33kΩ resistor and pulse-biased above breakdown with 3.8V for 4ns at a 10kHz repetition rate through a 100nF capacitor. The photon source was a cw HeCd laser operating at 325nm and attenuated to ~0.42 photons per detection gate length using calibrated neutral density filters.[14] The output pulses were discriminated and counted using a photon counter from Stanford Research Systems. The detection gate length was 5ns at 10kHz and was set longer than the ac bias in order to ensure that the entire response was collected. The fast rise and fall times of the ac pulse generated capacitive transients at the output, which were cancelled using matched 50Ω coaxial cables.[5] All measurements were taken at room temperature, because previous low temperature single photon counting results indicated little performance enhancement could be gained by operating at low temperatures. The sample had a conducting substrate and was mounted on a thick aluminum nitride pad. AlN was chosen for its excellent electrical isolation and thermal conduction.

7.2.3 Geiger-mode

Since the high dark count rates seemed to be the limiting factor on device performance, the discriminator threshold was set to minimize the number of dark counts. From Figure 7.5, the dark counts begin to flatten out after approximately 30mV and drop by 1MHz from 35mV to 45mV. The discriminator scan was repeated with an average photon number of 0.9 photons per gate. The difference between the total count rate and dark count rate was 4.5MHz and 6MHz for 54V and 54.5V dc bias, respectively. Thus, the device successfully counted at the single photon level, though 0.9 does not fulfill a rigorous definition of single photon counting as discussed in Chapter 3.

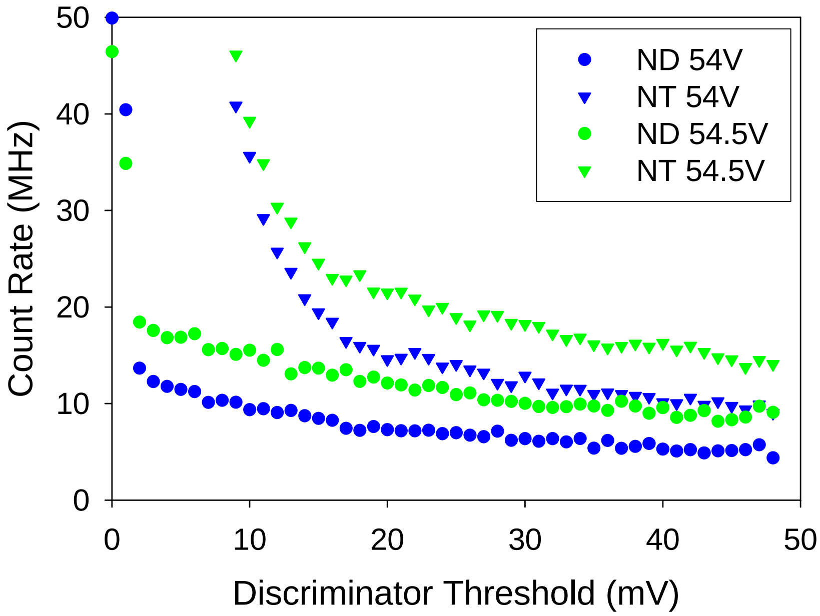

Figure 7.5 Total count rate and dark count rate versus discriminator threshold at 54V and 54.5V dc voltage.

The average photon number was set to 0.42, and the discriminator threshold was set to 45mV. Figure 7.6 shows the dark count rate and dark count probability versus SPDE. The dark count rate, dark count probability, and SPDE were calculated using equations (7.2), (3.1), and (3.2), respectively. The total count probability was calculated according to

$$P_T = \frac{N_T}{f \cdot t} \tag{7.4}$$

where N_T is the total number of counts per measurment including photo and dark, f is the repition rate of the ac and gate pulses, and t is the integration time, which was one second. The breakdown voltage, V_B, was 57V, when the breakdown was defined as the voltage at a current compliance of 50μA. The SiC APDs attained a maximum SPDE of 2.9% at an excess bias of approximately 1.6V. The excess bias ratio was instrumentation limited and higher excess biases may yield greater photon detection efficiency. The detection efficiency increased with the dc bias until it peaked at 54.8V dc bias, after which the dark count rate increased at a faster rate than the detection efficiency.

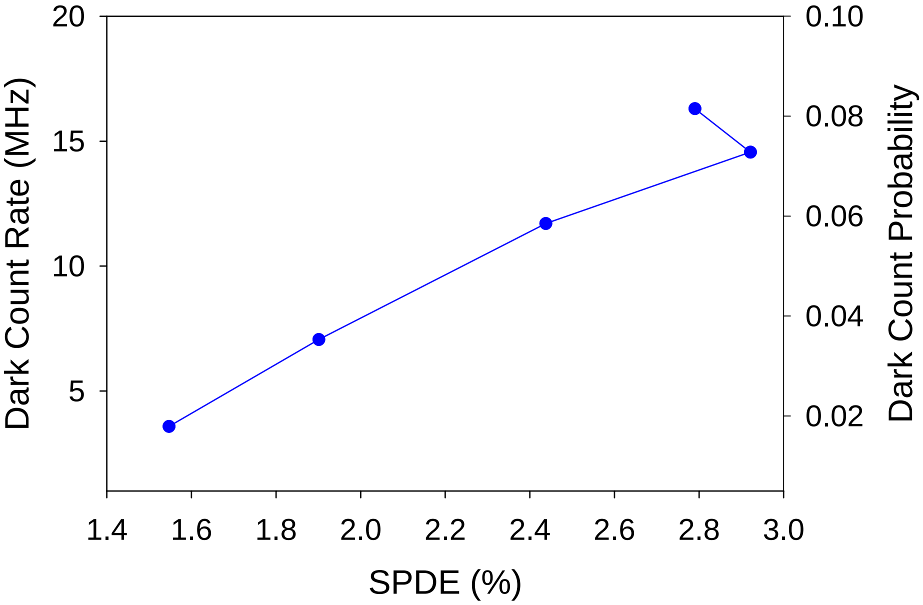

Figure 7.6 Dark count rate versus single photon detection efficiency at 53.5V, 54V, 54.5V, 54.8V, and 55V dc bias with a 3.8V ac bias.

The detection efficiency can also be represented as the product of the avalanche probability, P_b, and external unity-gain quantum efficiency. This is only accurate in the absence of afterpulsing, since afterpulsing can yield an effective avalanche probability greater than unity.[15] Figure 7.7 shows the dark count probability versus frequency for five dc bias voltages. As the dark count probability does not vary with frequency from 100Hz to 500kHz, we concluded that afterpulsing was not a significant source of dark counts for the frequency range used in these experiments. Therefore, we can conclude that the maximum attainable SPDE for these devices was 10%. It follows that $P_b = 0.29$, at the peak SPDE. Thus, 2.9% SPDE represents ~30% of the maximum attainable detection efficiency.

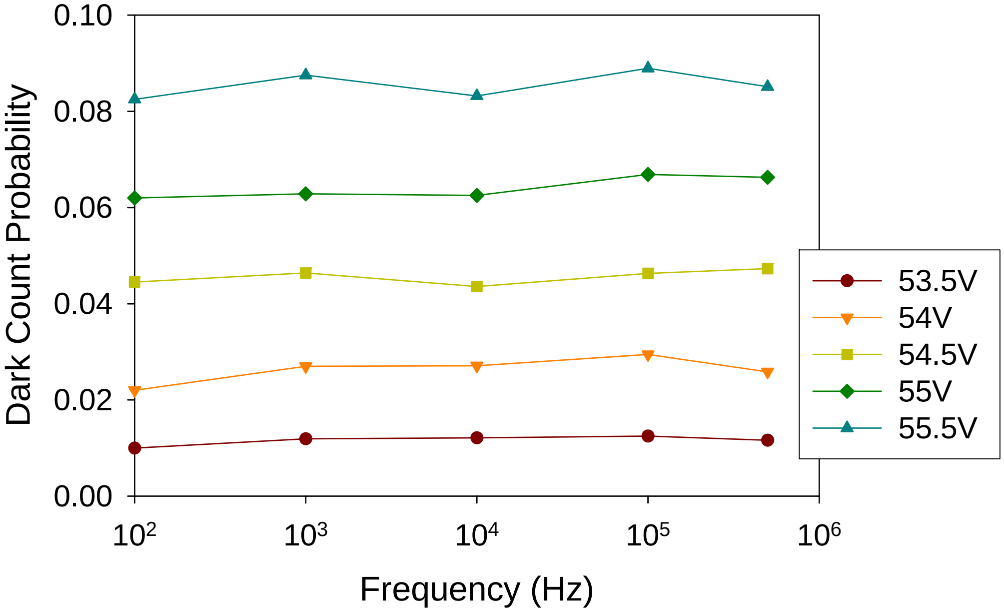

Figure 7.7 Dark count probability versus frequency for a 100μm-diameter ring contact SiC APD at RT.

7.3 Improved Experimental Set-up

In response to the unacceptably high dark count rates, system improvements were made, which included insulating the circuit, lowering the leakage current in the gate capacitor, and replacing the ground-signal probe head with a signal-signal probe head. The new 470pF gate capacitor had a leakage current of approximately 20pF, which was approximately four orders of magnitude lower than the 100nF capacitor. The ground-signal probe head from Cascade Microtech required using the outer cladding of the SMA connector for the output signal, which introduced a high noise level. The signal-signal probe, from Picoprobe, had two SMA connectors, with the cladding of each grounded to the same point, so that both the bias signal and the avalanche signal were carried on separate shielded center pins.

Figure 7.8 illustrates the result of this experiment by comparing the dark count rate versus discriminator threshold scans from Figure 7.5 to new scans for the same APD at 54V and 54.5V dc bias with 3.8V ac pulse height. The dark count rate following the set-up performance improvements was approximately 2MHz and 6MHz at 54V and 54.5V dc bias, respectively, at a 10mV discriminator threshold. At a 15mV threshold, the dark count rate was 720kHz and 3.5MHz at 54V and 54.5V dc bias, respectively. This represents an approximately 8MHz reduction in dark count rate at 54V dc bias and 10MHz reduction in dark count rate at 54.5V dc bias.

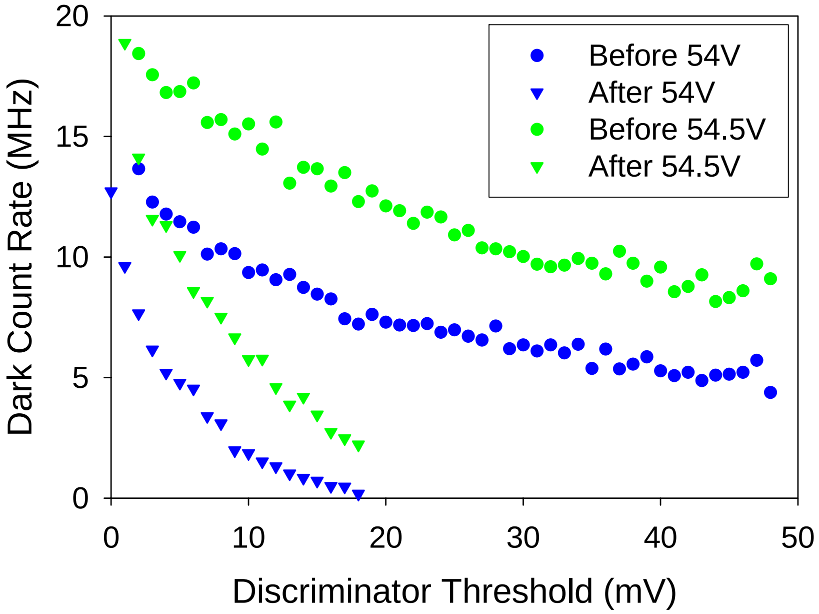

Figure 7.8 Dark count rate versus discriminator threshold at 54V and 54.5V dc voltage both before and after improvements were made to the set-up.

The SPDE as a function of dark count rate was found to yield similar results to the previous data for an average photon number of nbar = 0.4 and a discriminator threshold of 5mV. This represented an order of magnitude reduction in the discriminator threshold compared to the previous set up. Lowering the discriminator threshold is important since a high discriminator level reduces the photo counts as well as the dark counts. Thus, a balance must be found between raising the discriminator threshold to reduce dark counts and lowering the threshold to increase photo counts. Figure 7.9 shows the dark count rate and dark count probability versus SPDE for a 5mV discriminator threshold. The dc bias ranged from 53.5V to 57V. When the voltage was raised above 57V, the detection efficiency dropped just as it did in Figure 7.6 at 55V dc bias. The maximum SPDE attained was 6.9% at a dark count rate of 35MHz. An SPDE of 3.2% was achieved for a dark count rate of 13MHz.

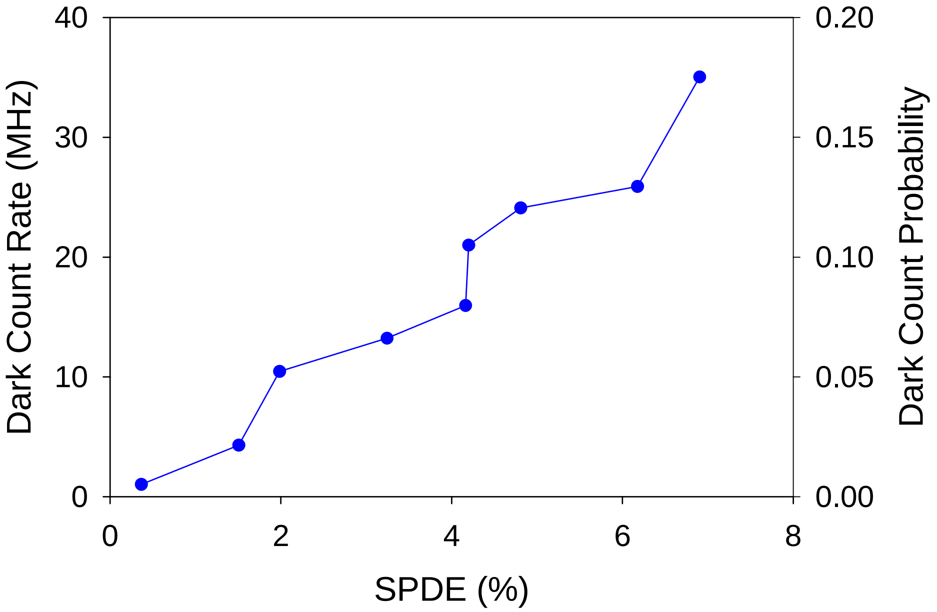

Figure 7.9 Dark count rate versus single photon detection efficiency at 53.5V, 54V, 54.5V, 54.8V, 55V, 55.5V, 55.8V, 56V, and 57V dc bias with a 3.8V ac bias.

7.4 Conclusion

Low temperature gated quenching measurements at 77K indicated that the tunneling current was too high for low temperature measurements to yield a significant reduction in the dark count rate, thus measurements proceeded at room temperature.

Ring contacts further improved the bulk breakdown uniformity, alleviating localized contact field crowding, which allowed for the first successful demonstration of gated quenching single photon counting in 4H-SiC APDs. SiC APDs operating in Geiger-mode were characterized at a wavelength of 325nm. The peak single photon detection efficiency was 6.9% at a dc bias of 57V and a photon level of 0.4 photons per gate. At a dark count rate of 13MHz, the SPDE was 3.2%.

Xin et al.[16] reported a 650KHz dark count rate for passive quenched p-n junction SiC APDs, but with only a 1% detection efficiency at 350nm. However, the 1MΩ load resistor used likely created a long recovery time, which may have placed an upper limit on the count rate. McIntosh et al.[17] reported a 13% SPDE with a 400kHz dark count rate for GaN APDs operated in Geiger-mode at 325nm. A 400kHz dark count rate in a 37μm-diameter device represents one order of magnitude lower dark count density compared to the SiC APDs discussed here. Therefore, the SiC SPAD dark count rate must be reduced in order for SiC APDs to prove a viable single photon counting technology. The next chapter will discuss a p-i-n device structure intended to reduce the dark count rate by reducing the contribution of tunneling to the dark current.

Chapter 8
Single Photon Counting p-i-n Avalanche Photodiodes

SiC APDs with a p-n junction structure demonstrated low single photon detection efficiency (SPDE) and prohibitively high dark count rates. Employing a p-i-n structure should improve the SPDE of the SiC APDs by decreasing the dark counts that result from tunneling current.[1] Additionally, the SPDE should improve due to an increase in the number of higher order avalanche events.[2] The slope of the avalanche probability as a function of overbias ratio is typically sharper for devices with thicker i-regions.[2-3] This is due to an increase in higher-order impact ionization events, which increases the chance of a carrier initiating a self-sustaining avalanche. Additionally, the detection efficiency is expected to improve as the result of using a device structure with an i-region.

Two structures were used in these experiments: a 260nm i-region and a 480nm i-region. These are the same structures referred to as PIN260 and PIN480 in Chapter 5. Gated quenching photon counting measurements will be presented for each i-region thickness, as well as passive quenching results for the PIN260 structure. The PIN480 structure could not operate under passive quenching due to oxide breakdown and contact failure at the high dc biases required.

8.1 Gated Quenching with a 260nm i-region

8.1.1 Linear-mode

A SiC APD was processed from the PIN260 wafer described in Chapter 5. The processing steps included the addition of a sacrificial thermal oxide between mesa etching and PECVD passivation. The 100μm-diameter mesa device had a ring contact and beveled edges to mitigate edge breakdown,[4] as shown in Figure 8.1.

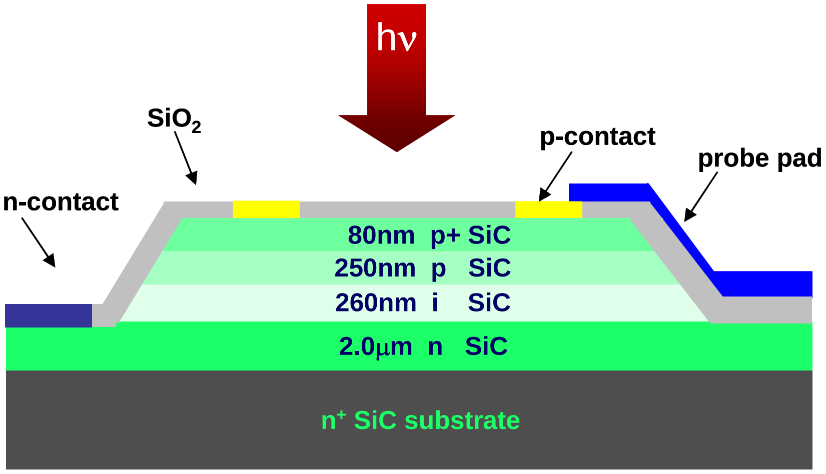

Figure 8.1 Cross-section of a 260nm i-region SiC APD with a ring contact.

The linear-mode gain reached 10^6 at a 1mA current compliance and a reverse bias voltage of 109V. The dark current at unity-gain was >0.5pA. At a gain of approximately 10^4 the dark current was ~5nA, which was two orders of magnitude smaller than the dark current in the p-n junction device at the same linear-mode gain. Typical linear-mode gain and IV curves for the PIN260 APD can be found in Figure 8.2.

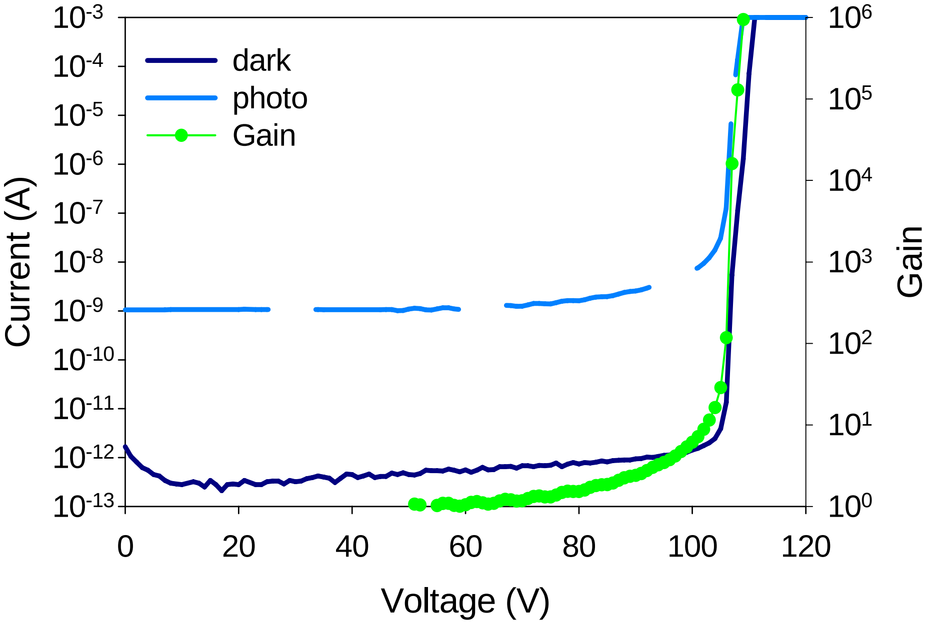

Figure 8.2 IV and gain characteristics of a 260nm i-region SiC APD.

A HeCd laser operating at 325nm was utilized for these measurements. At 325nm the external quantum efficiency of the SiC APDs was 14%. The capacitance of the 100μm-diameter device with a 75μm x 75μm probe pad was 2pF, and the series resistance was 45Ω. The resulting RC time constant was 0.1ns. An RC time constant as short as possible is important for reducing the ac pulse width for gated quenching. Reducing the pulse width helps to minimize the dark counts, because the carriers can only produce an avalanche pulse during the time that the total voltage is greater than the breakdown voltage.

8.1.2 Experimental Set-up

The PIN260 APD was measured using the setup in Figure 3.2 and a gated quenching circuit.[5-6] A new ac pulse generator capable of producing higher peak voltages was used due to the higher breakdown voltage of the p-i-n structure. This should have a two-fold advantage of increasing the avalanche probability through use of a higher excess bias ratio and improving device stability by maintaining a lower dc bias.

The APD was dc biased through a 33kΩ resistor and pulse-biased above breakdown, through a 470pF capacitor. Typical ac biases consisted of an 8-14V pulse height for 4ns to 7ns at a 10kHz repetition rate. Applying the capacitive voltage divider in equation (3.3) indicated that approximately 99% of the ac bias dropped across the diode. The fast rise and fall times of the ac pulse generated capacitive transients at the output that were cancelled using matched 50Ω coaxial cables.[6]

The photon source was a cw HeCd laser operating at 325nm and attenuated to ~0.1 photons per detection gate length using calibrated neutral density filters.[7] The output pulses were discriminated and counted using a Stanford Research Systems SR400 photon counter. All measurements were taken at room temperature. The sample had a conducting substrate and was mounted on a thick aluminum nitride pad. AlN was chosen for its excellent electrical isolation and thermal conduction.

The number of dark counts dropped rapidly as the discriminator threshold increased and leveled out at 4mV. The threshold was set between 4-10mV in order to minimize the number of dark counts while maximizing the opportunity for photo counts to pass. The SPDE was calculated using equation (3.2), while P_D, R_D, and P_T were calculated using equations (3.1), (7.2), and (7.4), respectively.

8.1.3 Geiger-mode

In the initial measurements, the ac pulse width was varied in order to optimize the measurement parameters. For this set of measurements, the discriminator threshold was 10mV. Figure 8.3 shows the SPDE as function of ac pulse width for a detection gate width ranging from 5ns to 8ns, where 5ns was the minimum gate width allowed by the instrumentation. Detection efficiencies of 4-5% were easily attainable in these devices. For a 14% external quantum efficiency, 5% SPDE represents approximately 33% of the total achievable. The dark count rate for this data ranged from 55kHz to 85kHz, which was more than a two order magnitude reduction compared to the p-n junction devices. The slope of the curves decreased as the gate width increased, particularly for the 8ns gate width. This indicated that as the gate width increased the dark count rate increased at a faster rate than the detection efficiency. Two gate widths were selected for further investigation, which included a 5ns gate width for lower dark count rates and a 6ns gate width for higher detection efficiencies. Further experiments revealed that 4ns and 7ns ac pulse widths were the best selections for the 5ns and 6ns gate widths, respectively.

For this configuration of ac and gate widths and a discriminator threshold of 4mV, the SPDE and dark count rate were measured for a 12V ac pulse height and dc bias ranging from 106V to 107.75V.

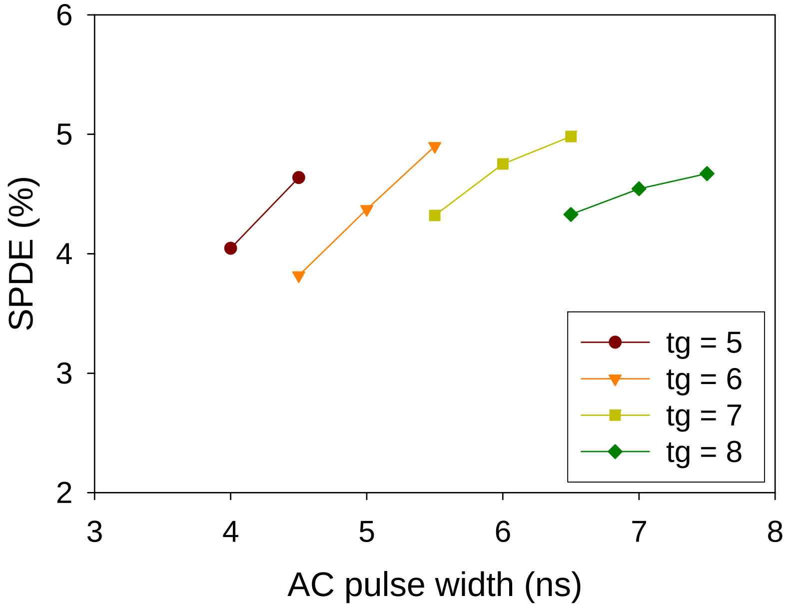

Figure 8.3 Single photon detection efficiency versus ac pulse width for gate widths of 5ns, 6ns, 7ns, and 8ns.

The SPDE for the 4ns ac pulse was 3.6% at a 28kHz dark count rate, which corresponded to $1.4 \cdot 10^{-4}$ dark count probability, as shown in Figure 8.4. This represented a three order magnitude reduction in the dark count rate at the same SPDE compared to the p-n junction devices. At 3.7% SPDE the 4ns and 7ns curves converged at a 40kHz dark count rate. For detection efficiencies greater than 4% the 7ns ac pulse width achieved greater detection efficiencies at lower dark count rates than the 4ns curve. As expected, the 4ns ac pulse width was best for achieving low dark count rates, while the 7ns ac pulse width was best for achieving high single photon detection efficiencies. The highest SPDE attained was 9.6% at a 122kHz dark count rate, or $7.3 \cdot 10^{-4}$ dark count probability. This represents almost 70% of the maximum attainable SPDE.

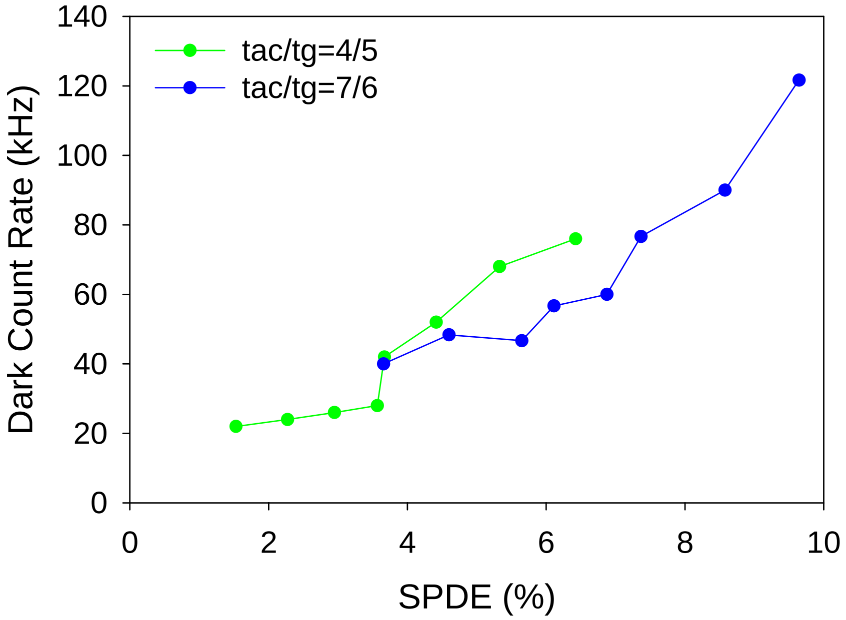

Figure 8.4 Dark count rate versus single photon detection efficiency using 4ns and 7ns ac pulse widths with 5ns and 6ns gate widths, respectively.

A 12V ac pulse height was selected based on measurements in which the ac pulse height varied from 10V to 14V. A higher ac pulse height allowed for a lower dc bias, and consequently a lower dark count rate. This results from the dark count rate dependence on both the number of dark carriers available to generate an avalanche pulse and the avalanche probability. According to Kang et al.,[8] there are four mechanisms that contribute to the number of dark carriers present in the junction during the ac voltage pulse. Two are directly related to afterpulsing, which was not present in SiC APDs at the measurement operating frequencies. The other two are directly related to the linear-mode dark current. The number of carriers injected into or generated inside of the active region during the voltage pulse can be expressed as $I_M \cdot \tau_{ac}/q$, where I_M is the primary dark current, τ_{ac} is the ac pulse width, and q is the electronic charge. The number of carriers still present in the junction that were generated before the ac pulse is equal to $I_M \cdot M \cdot \tau_{tr}/q$, where M is the gain at the dc bias voltage and τ_{tr} is the gain-bandwidth product. From this equation, a higher dc voltage correlates to higher gain, M, and will lead directly to a higher number of dark counts.

This trend was confirmed through two measurements of the dark count rate as a function of total APD bias voltage. The first measurement applied a fixed ac pulse height, while the dc bias voltage was varied, for four different values of ac pulse height ranging from 11.2V to 12V. The second measurement applied a fixed dc voltage, while the ac pulse height was varied, for three values of dc voltage including 106V, 107V, and 108V. From Figure 8.5(a), for a total voltage greater than approximately 118.5V the 11.2V ac pulse showed the highest dark count rate at any given total voltage, which was attributed to the higher dc bias voltages needed to attain the same total bias compared to the other curves. This trend continues with the 12V ac pulse yielding the lowest dark count rate, due to the lower dc voltage required to attain a given total voltage.

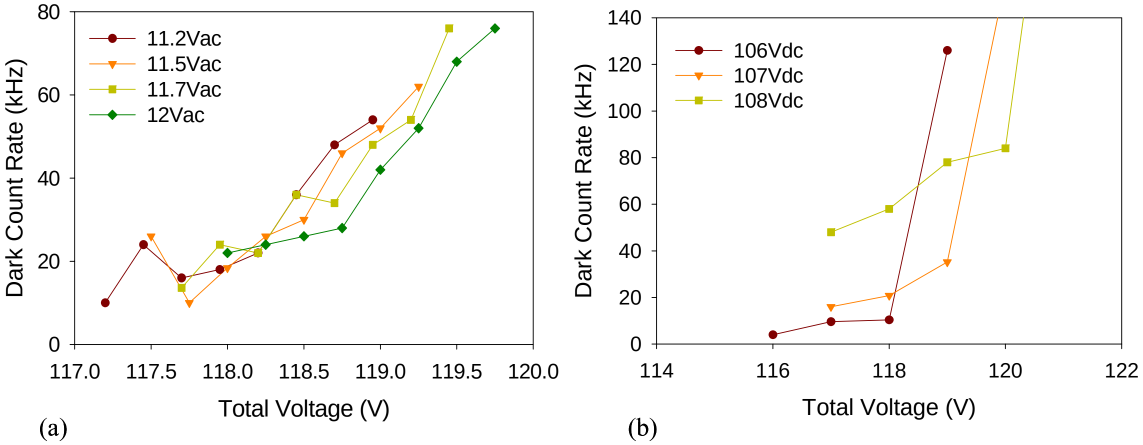

(a) (b)

Figure 8.5 Dark count rate versus total voltage for (a) fixed values of ac pulse height with varying dc bias voltage, for ac voltages of 11.2V, 11.5V, 11.7V, and 12V, and (b) fixed values of dc bias voltage with varying ac pulse height, for dc voltages of 106V, 107V, and 108V.

Figure 8.5(b) shows that for 106V dc bias the dark count rate was lower than that of 107V and much lower than that of the dark count rate at 108V. When the ac voltage was 12V or less, the dark count rate was relatively insensitive to increasing ac voltage for dc voltages of 106V and 107V. In the linear-mode, 108V was the deviation point of the measured IV curve from the modeled IV curve, thus more sensitivity to small changes in voltage was expected. For ac voltages greater than 12V the dark count rate increased exponentially. Though the reason for this behavior is unknown at this time, it places an upper limit of 12V on the ac pulse height regardless of the dc bias voltage for PIN260 APDs.

Figure 8.6(a) shows the SPDE versus total voltage for a fixed ac pulse height and varied dc bias voltages for four different values of ac pulse height ranging from 11.2V to 12V. The detection efficiency increased linearly with total voltage, but was relatively insensitive to ac pulse height. Figure 8.6(b) shows the SPDE versus total voltage for a fixed dc bias voltage and varied ac pulse height for three different values of dc bias voltage including 106V, 107V, and 108V. The SPDE increased with increasing dc voltage. For total voltages less than 120V, detection efficiency only increased slightly with increasing total voltage, but above 120V the increase was much sharper. At 106V dc bias the dark count rate was less than 20kHz. Unfortunately, the detection efficiency was less than 1% at 106V dc bias. Thus, the benefits of the low dark count rate at this voltage cannot be exploited.

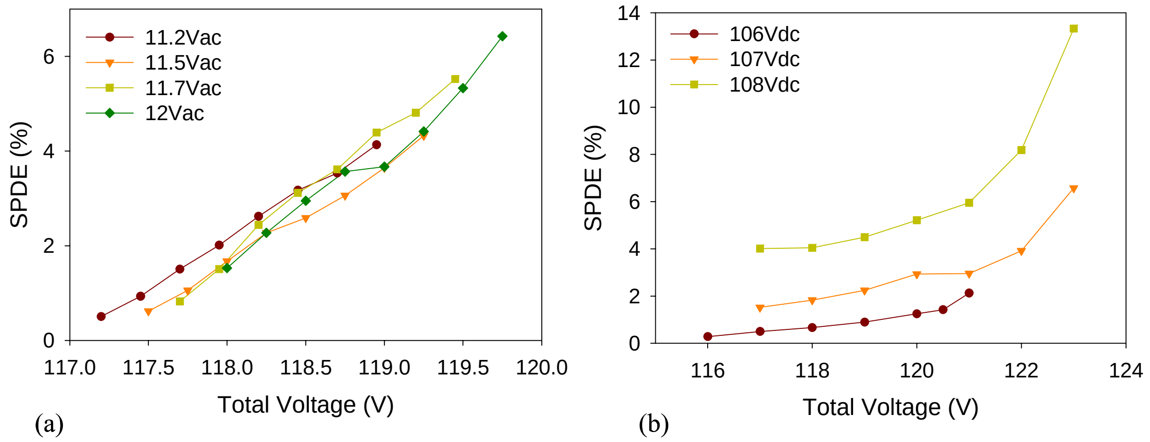

Figure 8.6 Single photon detection efficiency versus total voltage for (a) fixed values of ac pulse height with varying dc bias voltage, for ac voltages of 11.2V, 11.5V, 11.7V, and 12V, and (b) fixed values of dc bias voltage with varying ac pulse height, for dc voltages of 106V, 107V, and 108V.

8.1.4 Photon Counting and Diameter

Another approach to reducing dark count rates is to reduce the device size, since dark current scales with area. Accordingly, a 4x reduction in the dark count rate would be expected for a 50µm-diameter device compared to a 100µm-diameter device. However, the gain non-uniformity increased as the device diameter decreased, which resulted in the focused gain curves diverging more quickly from the gain measured under broad illumination. This indicated that the high field regions would contribute a higher number of dark counts to attain the same single photon detection efficiency. Furthermore, the 1mA compliance of the 50µm-diameter and 70µm-diameter devices was 113V and 111V, respectively, which was 4V and 2V higher than for the 100µm-diameter device, respectively. After multiple measurements on multiple devices, the 50µm-diameter device showed no photo counts at all, while the 70µm-diameter device attained only 1% SPDE at approximately 70kHz dark count rate.

8.2 Gated Quenching with a 480nm i-region

8.2.1 Linear-mode

A 100µm-diameter APD with a ring contact and beveled edges, as shown in Figure 8.7, was fabricated from the PIN480 wafer described in Chapter 5. The processing steps included the addition of a sacrificial thermal oxide between mesa etching and deposition of 6000Å of PECVD oxide.

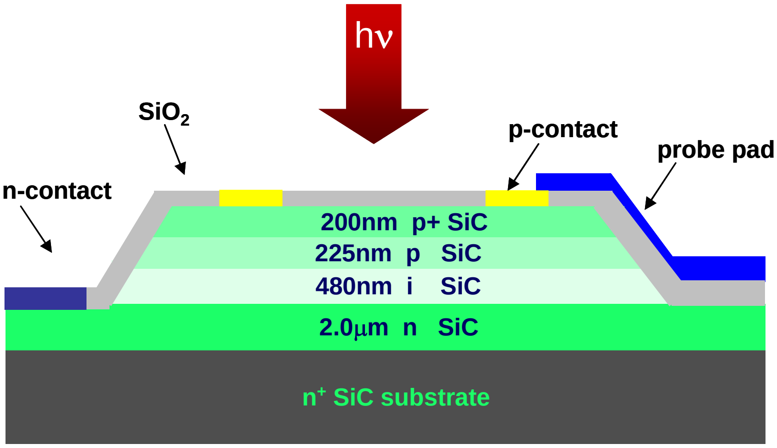

Figure 8.7 Cross-section of a 480nm i-region SiC APD with a ring contact.

The linear-mode gain reached $2{\cdot}10^6$ at a 1mA current compliance and a reverse bias voltage of 146V. The dark current at unity-gain was less than 1pA. At a gain of 10^3 (144V), the dark current was ~0.15nA, half that of the PIN260 device at the same linear-mode gain. Figure 8.8 shows typical linear-mode gain and IV curves for the PIN480 APD. The IV characteristics for both PIN260 and PIN480 were plotted together in Figure 5.7 for comparison.

These measurements utilized a HeCd laser operating at 325nm. At 325nm the external quantum efficiency of PIN480 was approximately 18%. The capacitance of a

100μm-diameter device with probe pads was 2pF, and the series resistance was 50Ω. The resulting RC time constant was 0.1ns.

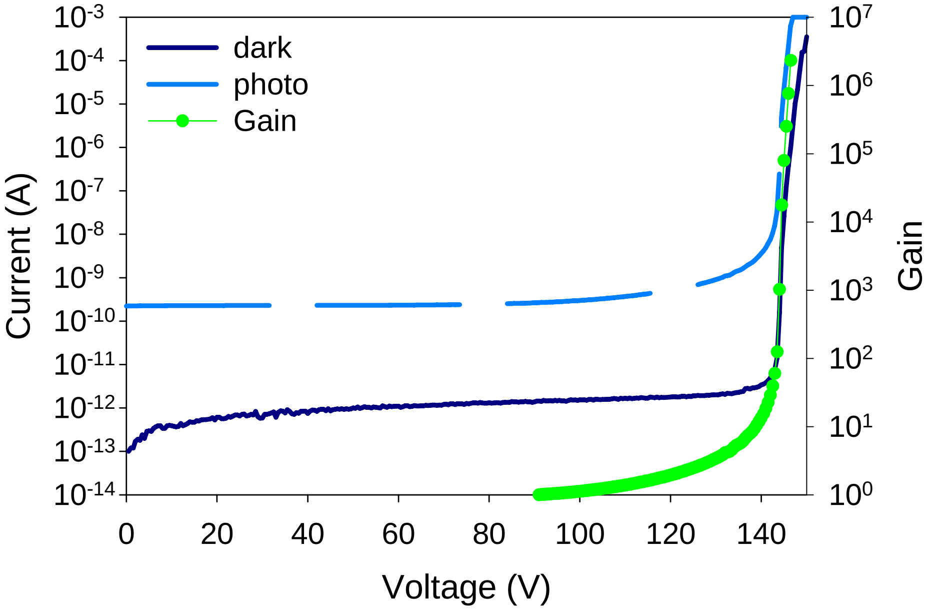

Figure 8.8 IV and gain characteristics of a 480nm i-region SiC APD.

8.2.2 Experimental Set-up

Geiger-mode characterization of a PIN480 APD was measured using the same set-up used to characterize the PIN260 APD. The dc bias ranged from 143V to 144.5V, and the ac pulse height varied from 18-24V for 4ns at a 10kHz repetition rate through a 470pF capacitor. The photon level was ~0.1 photons per detection gate length using calibrated neutral density filters.[7] Due to the conducting substrate the device was mounted on a thick AlN pad. The number of dark counts dropped rapidly as the discriminator threshold increased and leveled out at approximately 5mV. The discriminator threshold was set between 6-8mV.

8.2.3 Geiger-mode

Implementing a 480nm i-region was not expected to reduce the dark count rate as significantly as moving from a p-n junction device to a PIN260 device. The reasoning was two-fold. The largest contribution to the high dark count rate was tunneling current, which was mitigated by using the 260nm i-region.[1] Also, PIN480 had less than an order of magnitude reduction in dark current compared to PIN260 and showed no difference in multiplied dark current (Chapter 5). The expected performance enhancement was an increase in avalanche probability from nearly doubling the width of the active region.[2-3]

Figure 8.9 shows the dark count rate as a function of single photon detection efficiency for dc voltages of 144V and 144.5V. At 143V dc bias the SPDE remained below 2% for ac pulse heights as high as 23V. The best results yielded 2.8% efficiency at a 24kHz dark count rate, or $1.1 \cdot 10^{-4}$ dark count probability. These results were comparable to those achieved using a 4ns ac pulse in the PIN260 APD. For both dc bias voltages, the SPDE and R_D remained almost identical until just over 2.5% efficiency, at which point the dark count rates diverged. The sharp increase for the 144.5V curve was attributed to the 23V ac pulse height. As shown in Figure 8.10, the dark count rate increased exponentially from 22V, analogous to the ac pulse in the PIN260 APD at 12V.

Biasing the APDs at higher dc voltages resulted in catastrophic device failure, which was attributed to both contact failure and oxide breakdown. With additional processing improvements, higher bias voltages may yield the higher detection efficiencies seen in the PIN260 devices. At this stage in the research, the higher stability of the PIN260 APD was more important than the small improvement in dark count rate.

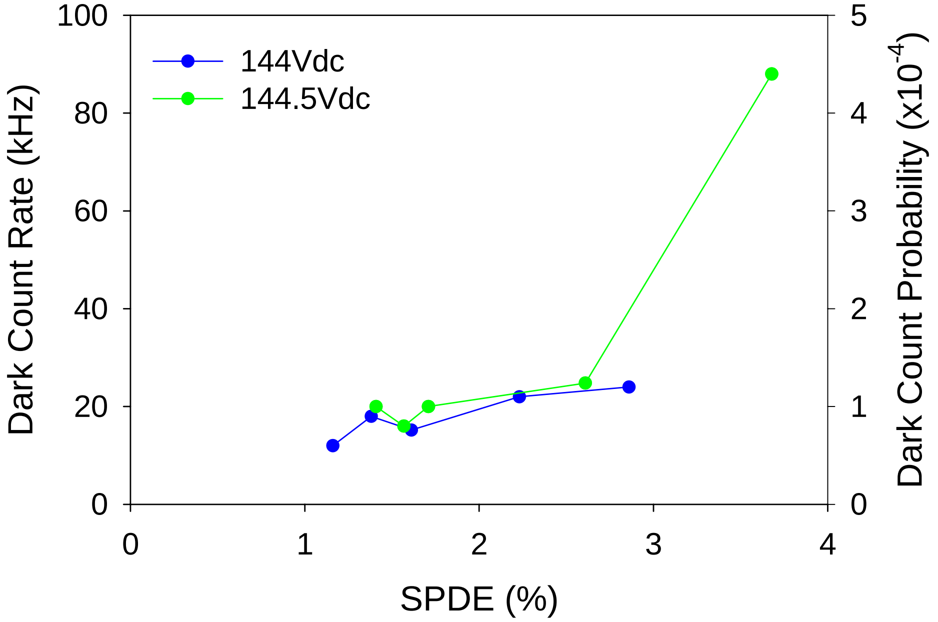

Figure 8.9 Dark count rate versus single photon detection efficiency for a PIN480 APD at dc bias voltages of 144V and 144.5V.

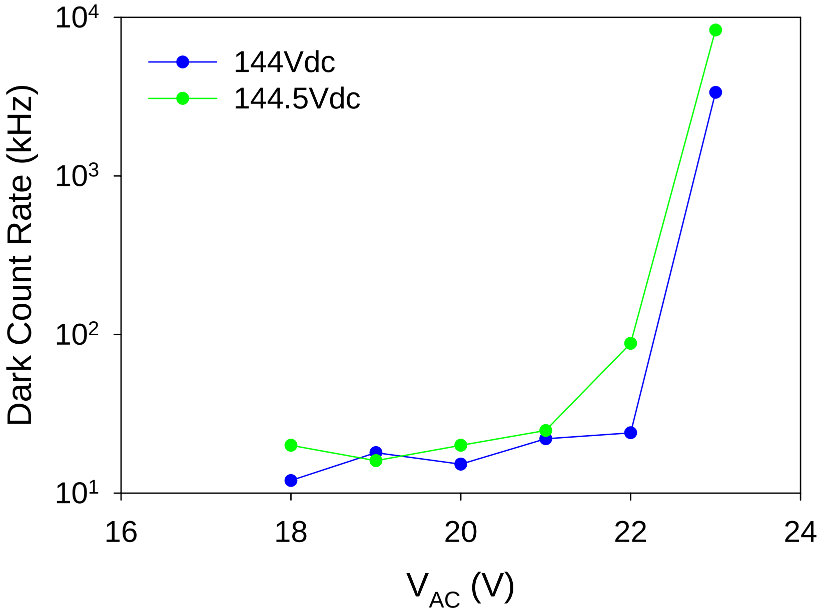

Figure 8.10 Dark count rate versus ac pulse height for a PIN480 APD at dc bias voltages of 144V and 144.5V.

8.3 Passive Quenching

8.3.1 Linear-mode

Two PIN260 devices fabricated from the same wafer were characterized using passive quenching including the device described in Section 8.1, which will be referred to as PIN260a. The second device, which will be referred to as PIN260b, was also a 100μm-diameter ring contact device, but had lower dark current than PIN260a. Figure 8.11 shows the IV characteristics of PIN260b. The linear-mode gain reached $4.5\cdot10^{6}$ at a 1mA current compliance and a reverse bias voltage of 110V. This gain was almost five times higher than the gain at the 1mA current compliance in PIN260a. The dark current at unity-gain was less than 1pA. At a gain of 10^{4}, the dark current was ~5nA, which was the same dark current level as in PIN260a for the same linear-mode gain. At gains greater than 10^{5}, the dark current in PIN260b was more than one order of magnitude lower than in PIN260a.

The capacitance of the 100μm-diameter device with a 75μm x 75μm probe pad was 2pF, and the series resistance was 8kΩ, which was attributed to high contact resistance. The resulting RC time constant was 16ns, which made these devices inappropriate for gated quenching measurements. The measurements utilized lasers operating at both 325nm and 266nm. The external quantum efficiency of the SiC APDs was 14% and 51% at 325nm and 266nm, respectively.

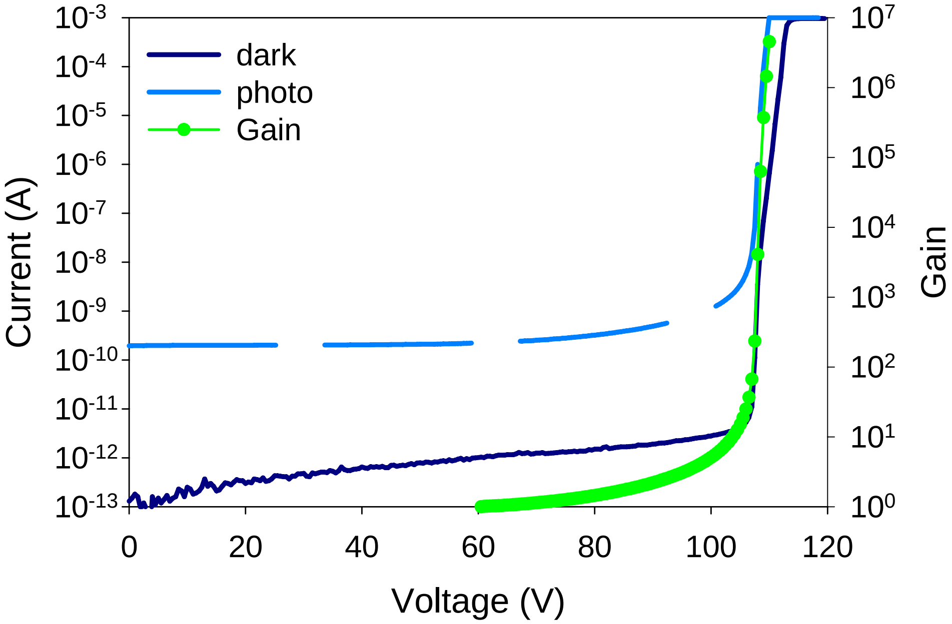

Figure 8.11 IV and gain characteristics of PIN260b.

8.3.2 Experimental Set-up

The experimental set-up for passive quenching was quite simple. The APDs were dc biased through a 220kΩ resistor connected in series with the input probe-head connector. The discriminator was set to 5mV in order to allow the maximum number of photo counts to pass. A 10mV discriminator threshold was considered, but showed a greater reduction in detection efficiency than in dark count rate; hence, measurements were taken at a 5mV discriminator threshold.

Both a 325nm cw HeCd laser and 266nm pulsed Nd:YAG laser were used for illumination. The cw laser was attenuated to a level of 25 photons/μs for measurements of PIN260a and 3.5 photons/μs for PIN260b. For comparison, previous reports of 325nm photon counting APDs using passive quenching operated at photon levels of 280 photons/μs and 2300 photons/μs.[7,9,10] The measurements were taken for a one second integration time, thus the number of dark counts was equal to the dark count rate. The single photon detection efficiency can be calculated according to

$$\mathrm{SPDE} = \frac{\left(N_T - N_D\right)}{\bar{n}} \tag{8.1}$$

for a cw laser, where N_T is the total number of counts, N_D is the number of dark counts, and nbar is the average number of photon per a 1 second integration time. For a pulsed laser this equation changes to

$$\mathrm{SPDE} = \frac{N_T - N_D}{\bar{n} \cdot f} \tag{8.2}$$

where nbar is the average number of photon per pulse and f is the repetition rate of the laser.

The pulsed laser was attenuated to approximately 0.43 photons per pulse, which only allowed for approximately 3200 possible photo counts for a one second integration time at 100% detection efficiency. The low number of photons contributed to a large error in the measurement. Alignment of the 266nm laser was performed at a photocurrent level of 600nA. The dark count rate increased approximately by 50% compared to the dark count rate prior to 266nm exposure. This was assumedly related to damage caused by the high energy photons. For PIN260a the damage was catastrophic; thus, the 266nm detection efficiency was not measured. However, initial measurements were attained for PIN260b at 266nm.

8.3.3 Geiger-mode

The dark count rate as a function of voltage revealed much higher dark count rates for PIN260a compared to PIN260b, as shown in Figure 8.12. At 110V, the dark count rate was 500kHz for PIN260a. PIN260b had a dark count rate of 27kHz at 111V, which yielded a comparable linear-mode gain.

Figure 8.13 shows the detection efficiency versus dark count rate for both PIN260a and b for 325nm photons. The SPDE for PIN260a saturated at approximately 3% at a dark count rate of 300kHz. PIN260b attained 3% detection efficiency at 27kHz, which was comparable to the gated quenching results. At 5.4% detection efficiency, the dark count rate reached 68kHz. At the same SPDE, PIN260a had a dark count rate of 47kHz in gated quenching operation, as shown in Figure 8.4.

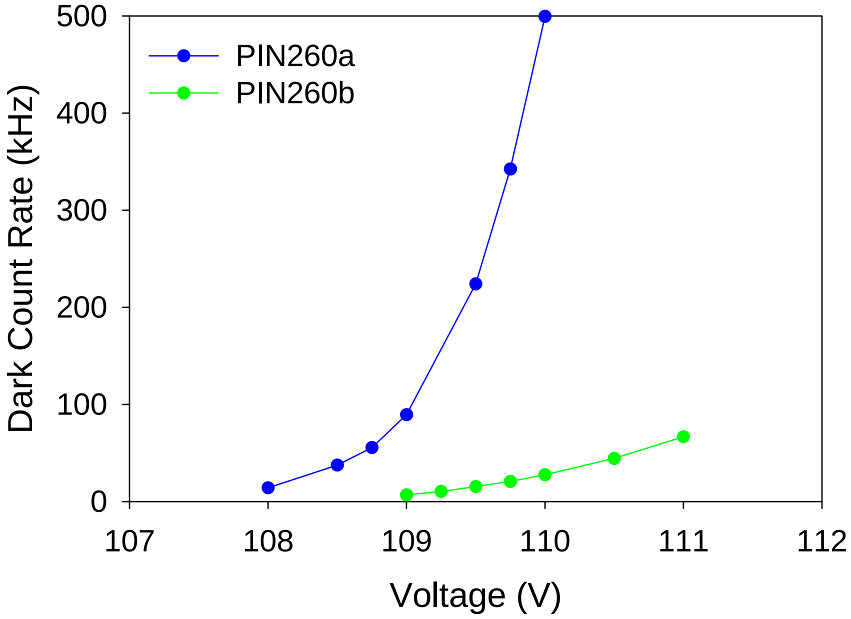

Figure 8.12 Dark count rate as a function of voltage for PIN260a and PIN260b.

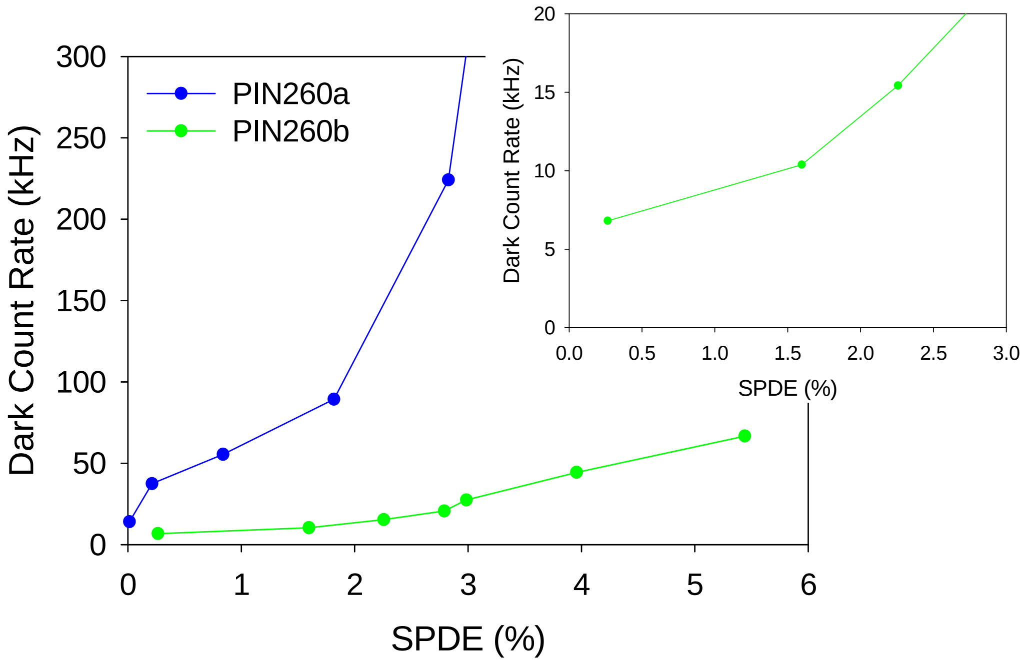

Figure 8.13 Dark count rate as a function of single photon detection efficiency for PIN260a and PIN260b at 325nm.

At 266nm, the total number of photons (approximately 3200) was relatively small compared to the tens of thousands of dark counts. This means that an SPDE of 10% would only show a difference of 320 counts, which was roughly equal to the standard deviation of dark counts at a dark count rate of 30kHz. Figure 8.14 shows the dark count rate as a function of SPDE for 266nm photons with error bars. At 109.75V, the SPDE was 44% ± 33%, which constituted a 75% error compared to approximately 1% error for the 325nm measurements. In other words, the detection efficiency was somewhere between 11% and 78%, which indicates that a much higher number of photons are required to take meaningful measurements at 266nm.

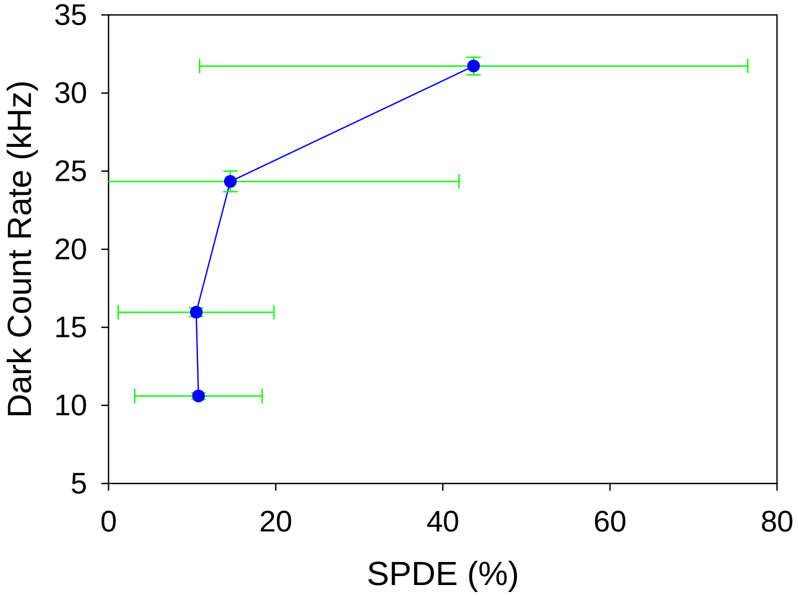

Figure 8.14 Dark count rate as a function of single photon detection efficiency for PIN260b at 266nm with uncertainty.

8.4 Conclusion

Both passive and gated quenching of p-i-n APDs with a 260nm i-region have been demonstrated. Only gated quenching was possible for APDs with a 480nm i-region due to processing constraints that limited the dc bias voltage. Both PIN structures attained a dark count rate of 24-28kHz at 3% SPDE, which was a three order reduction in dark count rate compared to p-n junction devices at the same SPDE. Detection efficiencies greater than 9% were achieved in the PIN260 device under gated quenching operation. Unfortunately, the dark count rate at this SPDE reached 122kHz. For high efficiencies, gated quenching was preferable because the lower dc voltages yielded lower dark count rates. Increased spatial non-uniformity in smaller diameter devices resulted in high dark count rates and lower detection efficiencies. Additionally, passive quenching measurements of the PIN260b at 266nm indicated potential for high SPDE in SiC APDs; however, the photon number must be increased relative to the dark count levels in order for meaningful measurements to take place.

Chapter 9
Conclusion

9.1 Summary

In order for semiconductor photodiodes to replace PMTs a high gain and low dark count rate photodiode with high UV and single photon detection capability must be developed. GaP APDs were the first devices studied in the pursuit of that goal, followed by SiC APDs, which emerged as the front-runner.

Both p-i-n and recessed window p-i-n structures, as well as a Schottky structure, were implemented using GaP structures with thin device layers. The results showed sub-picoamp dark current, photo response in the UV, and high gains up to 10^4, with good uniformity across the wafer. The peak quantum efficiency at 440nm indicated Γ-valley absorption, rather than band edge absorption, and the recess window device confirmed UV detection enhancement via reduction of the p-layer thickness. Additionally, the Schottky structure demonstrated potential for UV detection improvement. Though these results indicated that successful implementation of a Schottky – APD could achieve a device with both high gain and strong QE performance below 290nm, SiC APDs outperformed GaP APDs in every metric.

Linear-mode characterization of 4H-SiC APDs demonstrated sub-picoamp unity-gain dark current and gains higher than 10^6 for all three wafers investigated, which included p-n junction, 260nm i-region, and 480nm i-region structures. The fabrication and characterization techniques were detailed and included beveled edge formation and two-dimensional raster scan measurements of the spatial gain uniformity.

Taking raster scans of the mesa area revealed edge breakdown, contact field crowding, and material non-uniformity. Employing a sidewall bevel angle <10° suppressed edge breakdown. Additionally, a ring contact geometry alleviated contact field crowding. Decreasing the device diameter from 160μm to 100μm diminished non-uniformities resulting from variations in doping density in the p-n junction structure. The resulting 100μm-diameter ring-contact beveled-edge device was characterized as a single photon counting APD.

Low temperature gated quenching measurements at 77K indicated that the tunneling current was too high for low temperature measurements to yield a significant reduction in the dark count rate, thus measurements proceeded at room temperature. A room temperature set-up was established for gated quenching using a cw 325nm laser and passive quenching using both a cw 325nm laser and a pulsed 266nm laser. Functionality and selection of the gate capacitance, transient canceling cable length, and average photon number were discussed.

Characterization of APDs with varying degrees of uniformity indicated that gain uniformity is critical to device performance. The improvement in device uniformity allowed the first successful demonstration of gated quenching single photon counting in

SiC APDs. The peak single photon detection efficiency was 6.9% at 325nm with a dc bias of 57V and a photon level of 0.4 photons per gate. The SPDE was 3.2% at a dark count rate of 13MHz.

Dark current in the p-n junction devices was two orders of magnitude larger than in PIN260 devices and three orders larger than in PIN480 devices. Since higher dark current results in higher dark count levels in Geiger-mode, the p-i-n structures were expected to perform better than the p-n junction APDs and achieve higher external quantum efficiency.

Both passive and gated quenching of p-i-n APDs with a 260nm i-region were demonstrated. Only gated quenching was possible for APDs with a 480nm i-region due to processing constraints that limited the dc bias voltage. Both PIN structures attained a dark count rate of 24-28kHz at 3% SPDE and 325nm, which was a three order reduction in dark count rate compared to p-n junction devices at the same SPDE. The PIN260 device achieved detection efficiencies greater than 9% under gated quenching operation. Unfortunately, the dark count rate for SPDE this high reached 122kHz. For high efficiencies, gated quenching was preferable because the lower dc voltages yielded lower dark count rates. Smaller diameter p-i-n devices experienced increased spatial non-uniformity that resulted in high dark count rates and lower detection efficiencies. Additionally, passive quenching measurements of PIN260b at 266nm indicated potential for high SPDE in SiC APDs; however, the photon number must be increased relative to the dark count levels in order for meaningful measurements to take place.

9.2 Future Work

The study of SiC avalanche photodiodes as single photon counting detectors is still in its infancy. The main goal of this work was to show that it could work and demonstrate that Geiger-mode SiC APDs have potential worthy of further study. To that end, the project was successful; however, there is still much research to do.

Recently, I discovered that gain non-uniformity in PIN260 APDs increased as the device diameter decreased. This is counterintuitive and prevents the use of smaller diameter devices to lower the dark count rate through a reduction in bulk dark current. Two sets of devices of varying diameter were tested and revealed the same trend, but they were from the same wafer. Samples from different wafers that extend from wafer center to wafer edge should be studied in order to determine if the trend is consistent in multiple p-i-n wafers and consistent across the direction of layer thickness and doping variation. If the same trend emerges, devices of large diameter should be characterized in Geiger-mode.

Additionally, a set-up combining single photon detection and raster scan measurement techniques should allow the characterization of Geiger-mode performance as a function of device area. This would allow the peak performance of SiC APDs to be ascertained, as well as glean insight into the effect of gain uniformity on single photon detection efficiency. These measurements would be simplest using passive quenching.

Finally, the relationship among ac, dc, and total voltage should be better understood, in order to optimize the performance of SiC APDs in Geiger-mode. Figure 9.1(a) below shows the dark count rate for a 260nm i-region APD as a function of ac pulse height, which clearly reveals an exponential growth for ac voltages greater than 12V. The 480nm i-region device shows the same behavior for ac pulse heights greater than 22V. In Figure 9.1(b), the SPDE is shown as a function of total voltage for dc bias voltages of 106V, 107V, and 108V. The SPDE shows a clear dependence on dc voltage, but most models of Geiger-mode behavior only include total voltage and excess voltage as variables. The majority of devices designed to operate in Geiger-mode have lower linear-mode gain and consequently improved gain uniformity, thus the interdependence of ac, dc, and total voltage may not be the same as for SiC APDs. Studies of time varying fields and the anisotropic electric fields in SiC may yield insight into the effect of these mechanisms on SPDE and dark count rate.

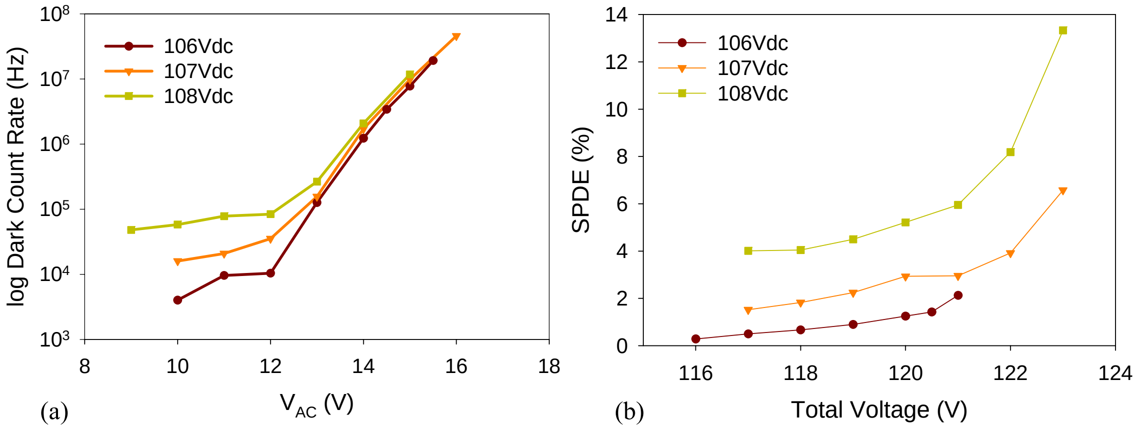

Figure 9.1 (a)Dark count rate for a 260nm i-region APD as a function of ac pulse height for dc voltages of 106V, 107V, and 108V, and (b) SPDE as a function of total voltage for dc bias voltages of 106V, 107V, and 108V.

Appendix
Process Flow for 4H-SiC APDs

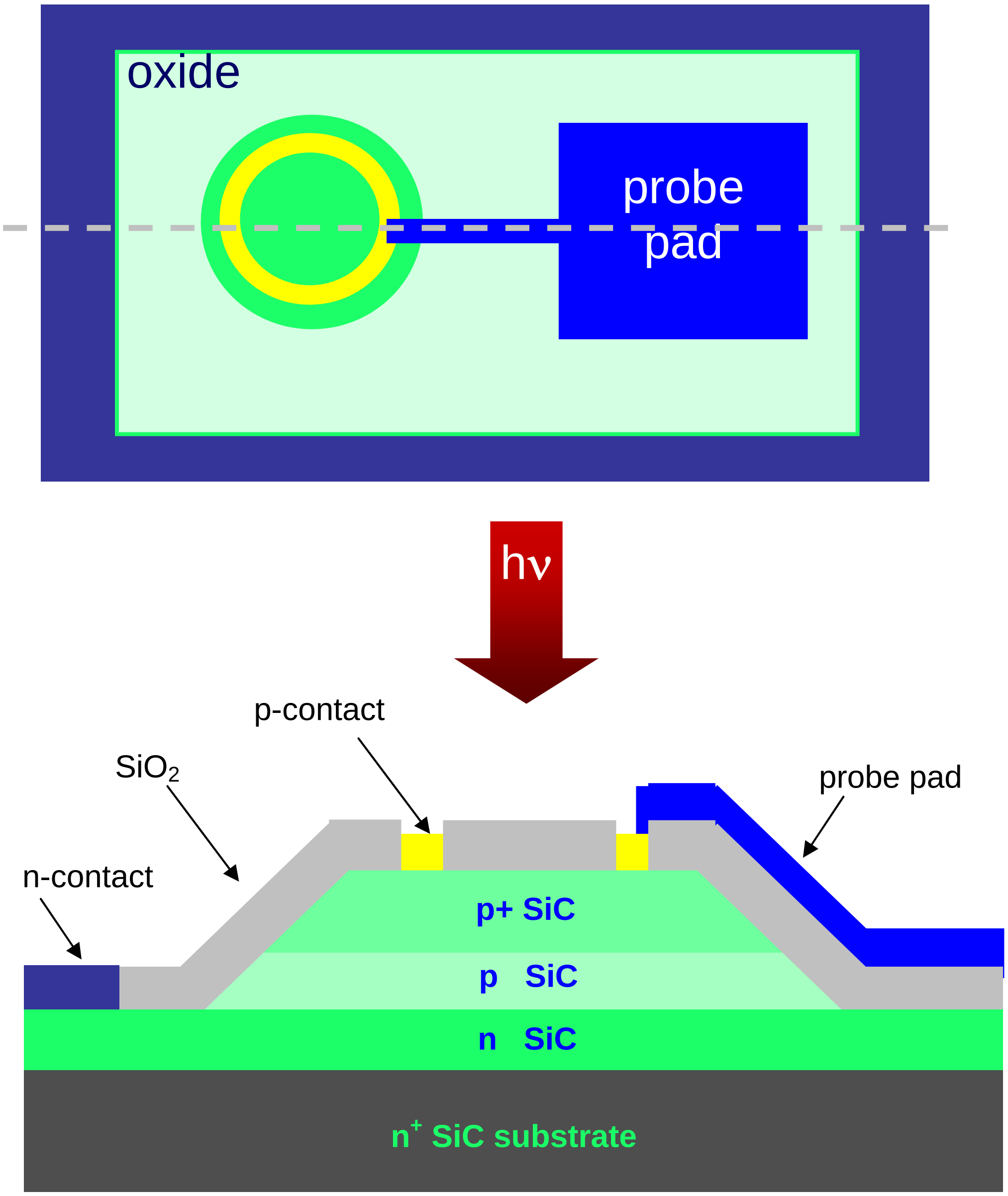

1. Surface prep of SiC:
    a. Organic solvent clean
    b. BOE pre-process dip for ~30 sec
    c. DI rinse and N_2 blow dry
    d. hydroscopic bake @ 150° C for 5 min

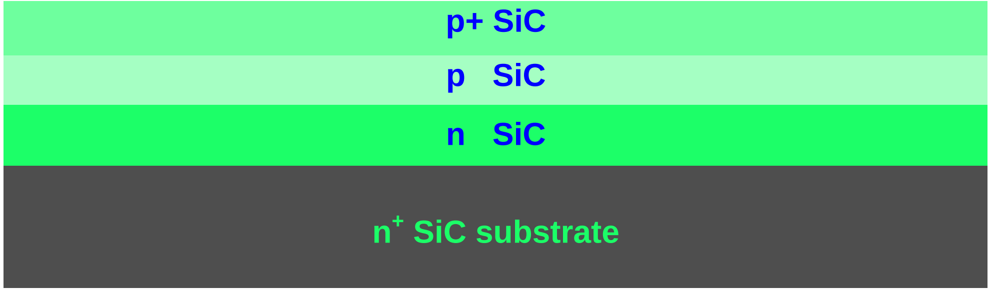

2. Mesa- mask definition
    a. standard clean of surface
    b. hydroscopic bake @ 150° C for 5 min
    c. spin on PR4620 @ 3K for 30 sec
    e. soft bake @ 90° C for 3 min
    f. photolithography using mesa layer; exposure for 1.8 min; develop in 1:3 AZ400K : H_20 for ~1 min
    g. optical inspection to ensure good development
    h. hot plate bake @ 140° C for 5 min
    i. hard bake 120° C for 10 min
    j. α-step measurement to verify photoresist step height
    k. DI rinse and N_2 blow dry

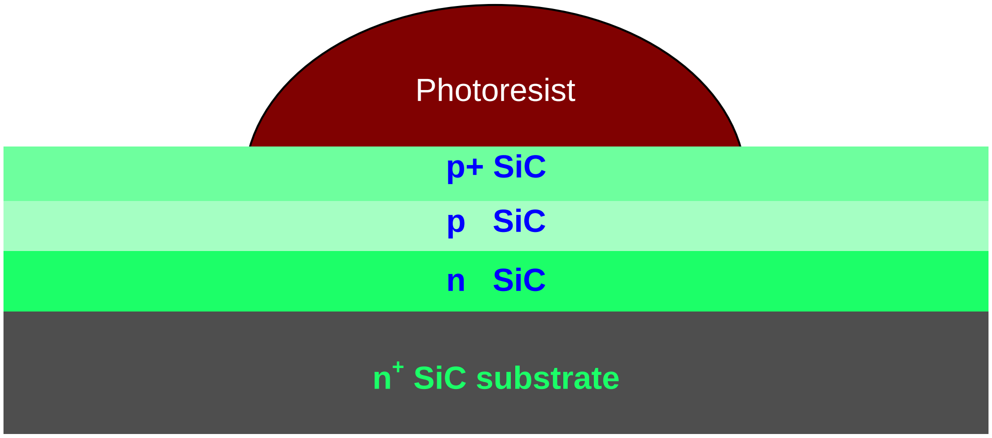

3. RIE Mesa definition
   a. RIE using 8sccm each of BCl_3 and $SiCl_4$ at 100W and 50mTorr (~175Å/min)
   b. α-step measurement and record step height

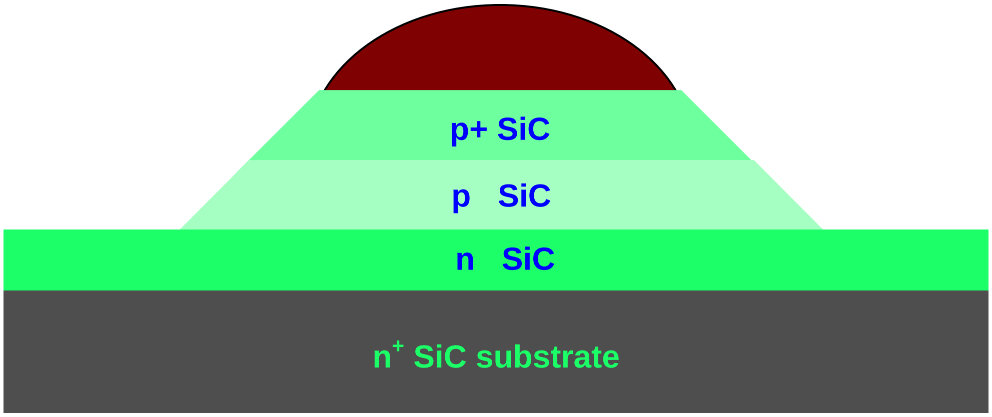

   c. strip photoresist using acetone in ultrasonic for as long as necessary
   d. standard clean of surface
   e. α-step measurement to verify step height

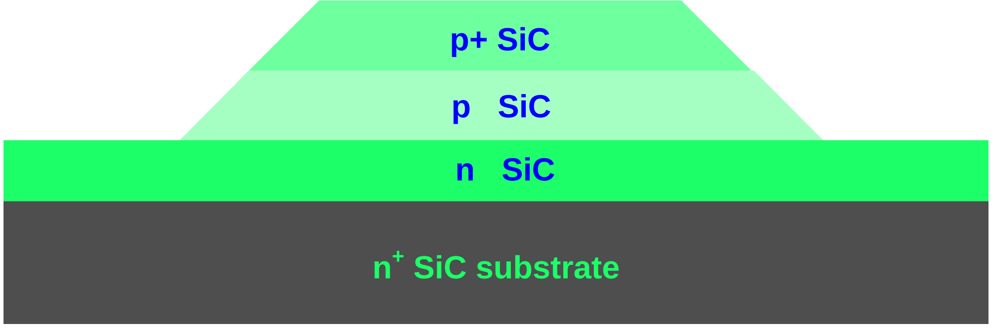

4. SiO_2 Passivation/AR coating layer deposition by PECVD
   a. PECVD 285° C
   b. adjust time to grow oxide layer to proper AR coating thickness (~2000Å)
   c. verify SiO_2 thickness on dummy Si sample using nanospec
   d. perform BOE calibration etch on the dummy sample

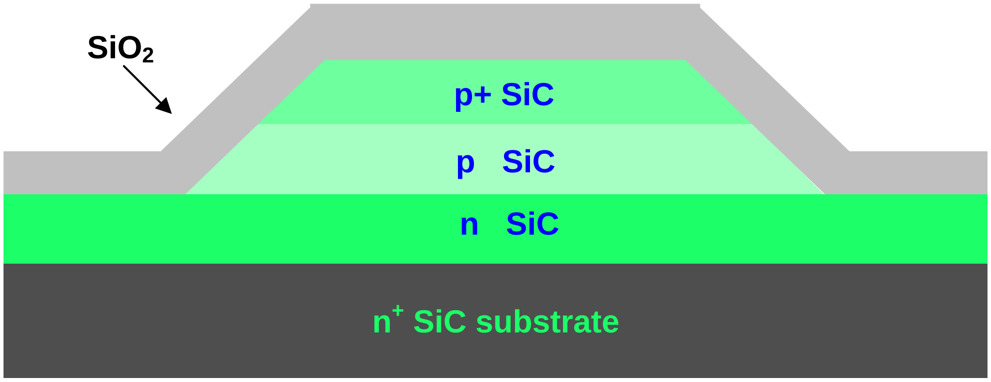

5. N-type contact formation
    a. standard clean and N_2 blow dry
    b. hydroscopic bake @ 150° C for 5 min
    c. spin on PR5214 @ 4K for 40 sec
    d. soft bake @ 90° C for 5 min
    e. photolithography using n-contact layer; exposure for 40 sec; develop in AZ 726 for ~30-45 sec
    f. hard bake @ 120° C for 5 min
    g. BOE based on calibrated etch time from step 4.d

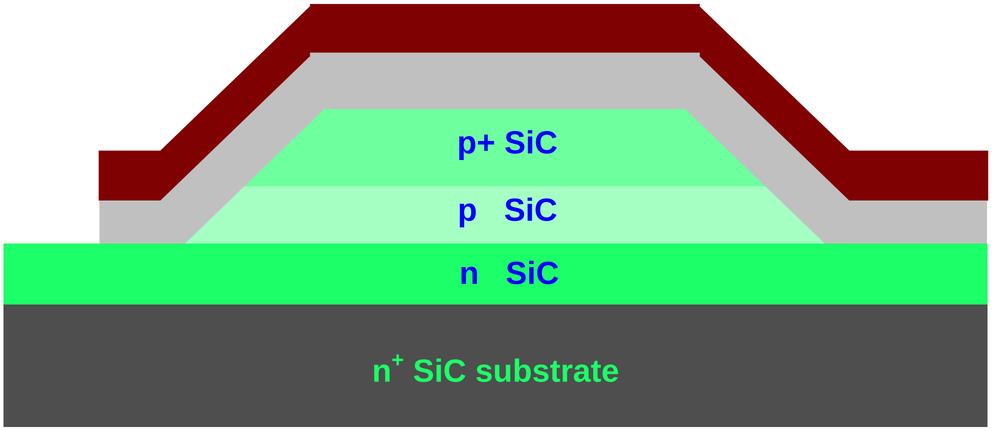

    h. e-beam evaporation of n-type ohmic metals
        1). Ni 1000 Å
    i. lift-off in acetone (ultrasonic only if necessary)
    j. RTA @ 900° C for 3 min

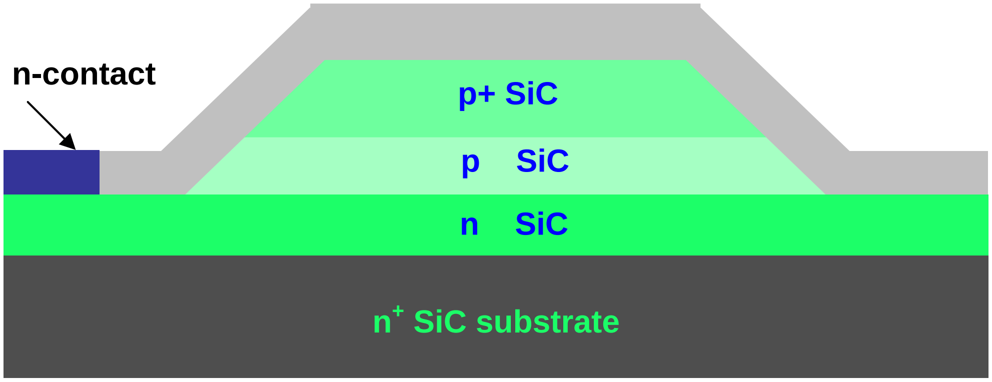

6. P-type contact formation
    a. standard clean and N_2 blow dry
    b. hydroscopic bake @ 150° C for 5 min
    c. spin on PR5214 @ 4K for 40 sec
    d. soft bake @ 90° C for 5 min
    e. photolithography using p-contact layer; exposure for 40 sec; develop in AZ 726 for ~30-45 sec
    f. hard bake @ 120° C for 5 min
    g. BOE based on calibrated etch time from step 4.d

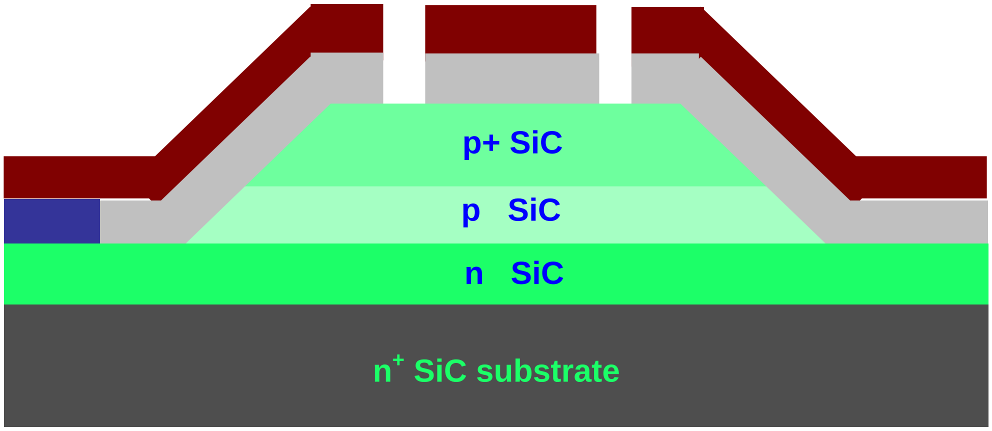

h. e-beam evaporation of p-type ohmic metals
    1). Ti 200 Å
    2). Al 800 Å
    3). Ti 200 Å
i. lift-off in acetone (ultrasonic only if necessary)
j. RTA @ 800° C for 2min

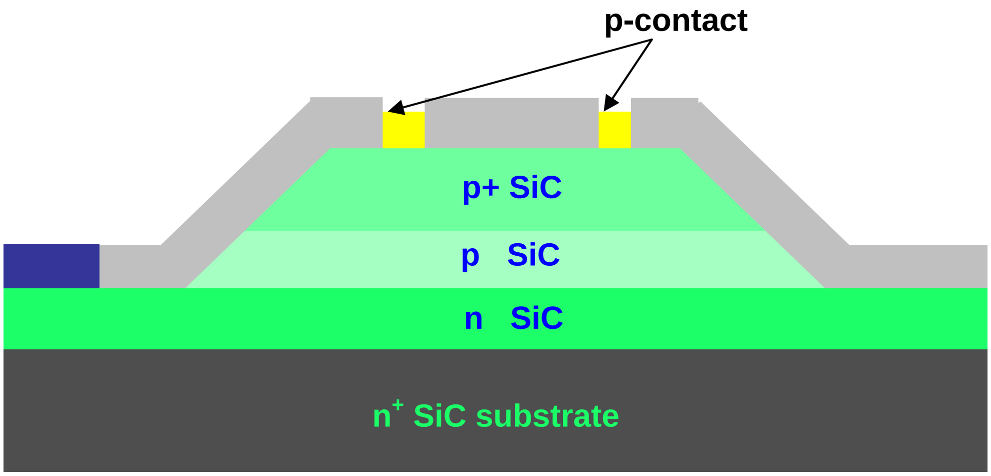

7. Probe Pad formation
    a. standard clean and N_2 blow dry
    b. hydroscopic bake @ 150° C for 5 min
    c. spin on PR5214 @ 4K for 40 sec
    d. softbake @ 90° C for 20 min
    e. photolithography using probe pad layer; exposure for 40 sec; develop in AZ 726 for ~30-45 sec

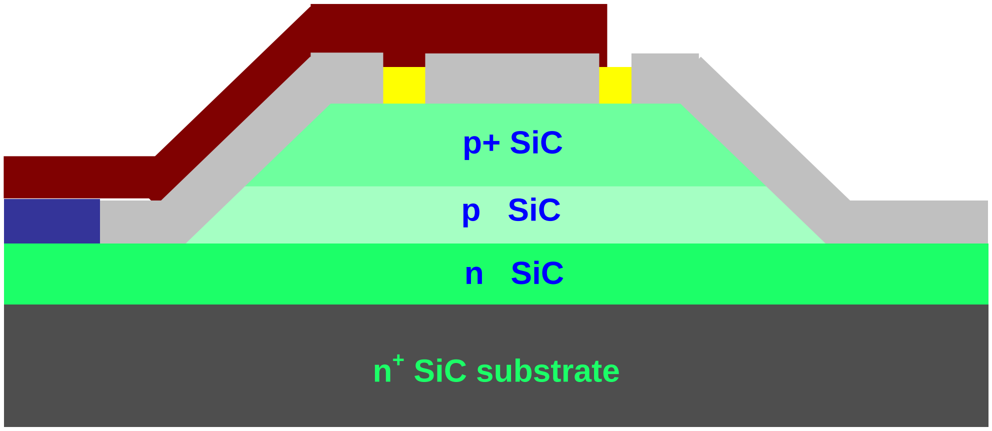

f. e-beam evaporation of probe pad metals
  1). Ti 100 Å
  2). Au 1000 Å

g. lift-off in acetone (ultrasonic only if necessary)

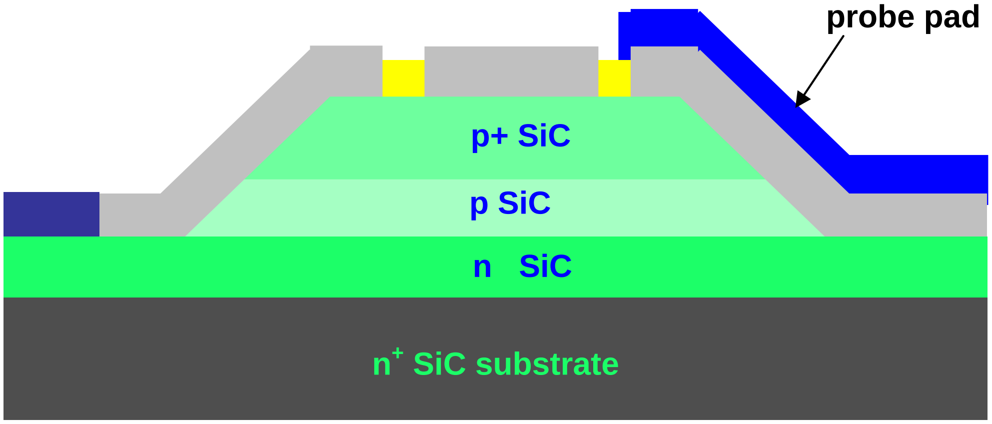

References

Chapter 1

[1] Charles.A. Primmerman, "Detection of Biological Agents," *Lincoln Laboratory Journal,* vol.12 n.1, pp. 3-31, 2000.

[2] G.A. Shaw, A.M. Siegel, and J. Model, "Ultraviolet Comm Links for Distributed Sensor Systems," IEEE LEOS Newsletter, pp. 26-9. October 2005.

[3] J.S. Ng, C.H. Tan, J.P.R. David, and G.J. Rees, "Theoretical study of breakdown probabilities in single photon avalanche diodes," 2003 IEEE LEOS Annual Meeting Conference Proceedings, vol.2 pp.773-4, Piscataway, NJ, USA, 2003.

[4] S. Cova, M. Ghioni, A. Lotito, I. Rech, and F. Zappa, "Evolution and prospects for single-photon avalanche diodes and quenching circuits," *J. Modern Optics*, vol. 51 n.9-10, pp. 1267-88, June-July 2004.

[5] D.M. Taylor, J.C. Jackson, A.P. Morrison, A. Mathewson, and J.G. Rarity, "Characterization of novel active area silicon avalanche photodiodes operating in the Geiger mode," *J. Modern Optics*, vol. 51 n.9-10, pp. 1324-32, June-July 2004.

[6] T. Isoshima, Y. Isojima, K. Hakomori, K. Kikuchi, K. Nagai, and H. Nakagawa, "Ultrahigh sensitivity single-photon detector using Si avalanche photodiode for the measurement of ultraweak biochemiluminescence," *Rev. Sci. Instrum.*, vol. 66 n.4, pp. 2922-2926, April 1995.

[7] J.C. Carrano, D.J.H. Lambert, C.J. Eiting, C.J. Collins, T. Li, S. Wang, B. Yang, A.L. Beck, R.D. Dupuis, J.C. Campbell, "GaN avalanche photodiodes," *Appl. Phys. Lett.* vol. 76 n.7, pp.924-926, 2000.

[8] B.Yang, T. Li, K. Heng, C. Collins, S. Wang, J.C. Carrano, R.D. Dupuis, J.C. Campbell, M.J. Schurman, I.T. Ferguson, "Low Dark Current GaN Avalanche Photodiodes," *IEEE J. of Quant. Electron.,* vol. 36 no. 12, Dec. 2000.

[9] S. Verghese, K.A. McIntosh, R.J. Molnar, L.J. Mahoney, R.L. Aggarwal, M.W. Geis, K.M. Molvar, E.K. Duerr, and I. MeIngailis, "GaN Avalanche Photodiodes Operating in Linear-Gain Mode and Geiger Mode," IEEE Trans. Electron Devices, vol. 48 n.3, pp.502-511, March 2001.

[10] T. Li, D.J.H. Lambert, M.M. Wong, C.J. Collins, B. Yang, A.L. Beck, U. Chowdhury, R.D. Dupuis, and J.C. Campbell, "Low-noise Back-Illuminated AlGaN-Based p-i-n Solar-Blind Ultraviolet Photodetectors," *IEEE J. Quant. Electron*, vol. 37 n. 4, pp. 538-545, April 2001.

[11] K.A. McIntosh, R.J. Molnar L.J. Mahoney, K.M. Molvar, N. Efremow, Jr., and S. Verghese, "Ultraviolet photon counting with GaN avalanche phtodiodes," *Appl. Phys. Lett.*, vol. 76 n. 26, pp. 3938-40, 26 June 2000.

[12] I. Prochazka, K. Hamal, and B. Sopko, "Recent acheivments in single photon detectors and their applications," *J. Modern Optics*, vol. 51 n. 9-10, pp.1289-1313, June-July 2004.

[13] A.N. Pikhtin, S.A. Tarasov, T.A. Orlova, and B. Kloth, "Selective and broadband GaP UV photodetectors," IWRFRI'2000, International Workshop: Results of Fundamental Research for Investments. St. Petersburg, Russia, 2000.

[14] A.N.Pikhtin, S.A. Tarasov, "Ag-GaP Schottky Photodiodes for UV Sensors," IEEE Trans. on Electron Dev., vol. 50 no. 1 p. 215, 2003.

[15] Goldberg Yu.A. *Handbook Series on Semiconductor Parameters*, vol.1, World Scientific, London, 1996, pp. 104-124.

[16] F.Yan, C.Qin, J.H.Zhao, M.Weiner, B.K.Ng, J.P.R.David, and R.C.Tozer, "Low noise visible-blind UV avalanche photodiodes with edge terminated by 2° positive bevel," *Electon. Lett.*, vol. 38, pp. 335-336, 2002.

[17] Xiangyi Guo, *High Performance Ultraviolet 4H-SiC Avalanche Photodiodes*. Dissertation. University of Texas at Austin, 2005.

[18] *Process Technology for Silicon Carbide Devices*. London: INSPEC, 2002. Editor Carl-Mikael Zetterling.

[19] J.S. Ng, C.H. Tan, and J.P.R. David, "A comparison of avalanche breakdown probabilities in semiconductor materials," *J. Modern Optics,* vol. 51 n. 9-10, pp.1351-1321, 15 June- 10 July 2004.

[20] A.R. Powell and L.B. Rowland, "SiC materials-progress, status, and potential roadblocks," *Proceedings of IEEE*, vol. 90 n. 6, pp.942-955, 2002.

[21] A.L. Beck B. Yang, X. Guo, and J.C. Campbell, “Edge Brakdown in 4H-SiC Avalanche Photodiodes,” IEEE. J Quant. Electron., vol. 40 n. 3, pp.321-4, March 2004.

[22] X. Xin, F. Yan, X. Sun, P. Alexandrove, C.M. Stahle, J. Hu, M. Matsumura, X. Li, M. Weiner, and H.J. Zhao, “Demonstration of 4H-SiC UV single photon counting avalanche photodiodes,” *Electron. Lett.*, vol. 41 n. 4, 17 February 2005.

[23] A.L. Beck, G. Karve, S. Wang, J. Ming, X. Guo, and J.C. Campbell, “Geiger Mode Operation of Ultraviolet 4H-SiC Avalanche Photodiodes,” *IEEE Photon. Tech. Lett.*, vol. 17 n.7, July 2005.

Chapter 2

[1] G.E. Stillman and C.M. Wolfe, “Avalanche Photodiodes,” *Semiconductors and Semimetals*, vol. 12, Academic Press, pp.291-393, 1977.

[2] R.J. McIntyre, “Multiplication noise in uniform avalanche photodiodes,” *IEEE Trans. Electron. Dev.*, vol.13 n.1, pp.164-8, January 1966.

[3] P.A. Hiskett, G.S. Buller, A.Y. Loudon, J.M. Smith, I. Gontijo, A.C. Walker, P.D. Townsend, and M.J. Robertson, “Performance and design of InGaAs/InP photodiodes for single-photon counting at 1.55μm,” *Appl. Optics*, vo. 39 n. 26, 20 December 2000.

[4] B.F. Aull, A.H. loomis, D.J. Young, R.M. Heinrichs, B.J. Felton, P. J. Daniels, and D.J. Landers, “Geiger-mode Avalanche Photodiodes for Three-Dimensional Imaging,” *Lincoln Laboratory Journal*, vol. 13 n.2, 2002.

[5] S. Cova, M. Ghioni, A. Lacaita, C. Samori, and F. Zappa, “Avalanche photodiodes and quenching circuits fro single-photon detection,” Appl. Optics, vol. 35 n. 12, pp.1956-1958, 20 April 1996.

[6] S. Wang, F. Ma, X. Li, G. Karve, X. Zheng, and J.C. Campbell, “Analysis of breakdown probabilities in avalanche photodiodes using a history-dependent analytical model,” *Appl. Phy. Lett*. vol. 82 n. 12, pp. 1971-3, 24 March 2003.

[7] J.S. Ng, C.H. Tan, and J.P.R. David, “A comparison of avalanche breakdown probabilities in semiconductor materials,” *J. Modern Optics*, vol. 15 n. 9-10, pp.1315-21, July 2004.

Chapter 3

[1] S. Cova, M. Ghioni, A. Lacaita, C. Samori, and F. Zappa, "Avalanche photodiodes and quenching circuits fro single-photon detection," Appl. Optics, vol. 35 n. 12, pp.1956-1958, 20 April 1996.

[2] Gauri Karve. *Avalanche Photodiodes as Single Photon Detectors*. Dissertation. University of Texas at Austin, 2005.

[3] B.F. Levine, C.G. Bethea, and J.C. Campbell, "Near Room Temperature 1.3µm Single Photon Counting with a InGaAs Avalanche Photodiode," Electron. *Lett.*, vol. 20 n. 14, pp. 596-7, 1984.

[4] D.S. Bethune and W.P. Risk, "An Autocompensating Fiber-Optic Quantum Cryptography System Based on Polarization Splitting of Light," IEEE J. Quant. Electron., col. 36 n. 3, March 2000.

[5] B.A.E. Saleh and M.C. Teich. *Fundamentals of Photonics*. New York: Wiley, 1991.

Chapter 4

[1] C.A. Primmerman, *Detection of Biological Agents*, Lincoln Laboratory Journal vol.12 n.1, 2000.

[2] J.C. Carrano, D.J.H. Lambert, C.J. Eiting, C.J. Collins, T. Li, S. Wang, B. Yang, A.L. Beck, R.D. Dupuis, J.C. Campbell, "GaN avalanche photodiodes," *Appl. Phys. Lett.* vol. 76 n. 7, 2000.

[3] B.Yang, T. Li, K. Heng, C. Collins, S. Wang, J.C. Carrano, R.D. Dupuis, J.C. Campbell, M.J. Schurman, I.T. Ferguson, "Low Dark Current GaN Avalanche Photodiodes," *IEEE J. of Quan. Elect.,* vol. 36 no. 12, Dec. 2000.

[4] McIntosh, K.A., Verghese, S., Molnar, R.J., Mahoney, L.J., Molvar, K.M., Connors, M.K., Aggarwal, R.L., Melngailis, I.L., "Ultraviolet photon counting with GaN avalanche photodiodes," *58th DRC. Device Research Conference*, p169, 2000.

[5] F. Yan, et al., "4H-SiC avalanche photodiode with multistep junction extension termination," *Elect. Lett.* vol. 38, n. **7**, pp-335-336, 1998.

[6] Goldberg Yu.A. *Handbook Series on Semiconductor Parameters*, vol.1, World Scientific, London, 1996, pp. 104-124.

[7] Roithner Lasertechnik, http://www.roithner-laser.com/UV-PD.html

[8] A.R. Clawson, "Guide to references on III-V semiconductor etching," *Matl. Sci. Engr.,* vol. 31, pp. 1-438, 2001.

[9] T. Li, S. Wang, A.L. Beck, C. Collins, B. Yang, R.D. Dupuis, J.C. Carrano, M.J. Schurman, I.T. Ferguson, J.C. Campbell, "High quantum efficiency AlGaN/GaN-based ultraviolet photodetectors with a recessed window structure," *Proc. SPIE*, vol. 3948, pp. 304-310, Apr 2000.

[10] A.N. Pikhtin, S.A. Tarasov, T.A. Orlova, and B. Kloth, "Selective and broadband GaP UV photodetectors," IWRFRI'2000, International Workshop: Results of Fundamental Research for Investments. St. Petersburg, Russia, 2000.

[11] A.N. Pikhtin, S.A. Tarasov, "Ag-GaP Schottky Photodiodes for UV Sensors," *IEEE Trans. on Electron Dev.*, vol. 50 no. 1 p. 215, 2003.

[12] T. Li, J.C. Carrano, J.C. Campbell, M. Schurman, and I. Ferguson, "Analysis of External Quantum Efficiencies of GaN Homojunction p-i-n Ultraviolet Photodetectors," *IEEE J.of Quan. Elect.,* vol. 25 no. 8, Aug. 1999.

[13] T.S Moss, G.J. Burrell, and B. Elias, *Semiconductor Opto-electronics*. New York: Wiley, 1973.

[14] R. Shikler, N. Fried, T. Meoded, and Y. Rosenwaks, "Measuring minority-carrier diffusion length using Kelvin probe force microscope," *Phy. Rev. B*, vol. 61 n.16, April 15, 2000.

[15] S. Wang, R. Sidhu, G. Karve, F. Ma, X. Li, X.G. Zheng, J.B. Hurst, X. Sun, N. Li, A.L. Holmes, and J.C. Campbell, "A Study of Low-Bias Photocurrent Gradient of Avalanche Photodiodes," *IEEE Trans. on Electron Dev*., vol. 49, n. 12, 2002.

[16] R. J. McIntyre, "Multiplication noise in uniform avalanche diodes," *IEEE Trans. on Electron Dev.,* vol. 13, n. 1, pp.164- 1966.

[17] Wang, S., Hurst, J.B., Ma, F., Sidhu, R., Sun, X., Zheng, X.G., Holmes, A.L., Jr., Huntington, A., Coldren, L.A.; Campbell, J.C., "Low-noise impact-ionization-engineered avalanche photodiodes grown on InP substrates," *IEEE Photonics Tech. Lett.,* vol. 14 n. 12, pp.1722-1724, Dec. 2002 .

[18] A.N. Pikhtin, S.A. Tarasov, “Ag-GaP Schottky Photodiodes for UV Sensors,” *IEEE Trans. on Electron Dev.*, vol. 50 n. 1 p. 215, 2003.

[19] Carrano, J.C.; Li, T.; Beck, A.L.; Collins, C.; Dupuis, R.D.; Campbell, J.C.; Schurman, M.J.; Ferguson, I.A., “Improved device performance using a semi-transparent p-contact AlGaN/GaN heterojunction positive-intrinsic-negative photodiode,” *Appl. Phy. Lett.*, vol. 75, p.2138, 1999.

Chapter 5

[1] F. Yan, C. Qin, J.H. Zhao, M. Weiner, B.K. Ng, J.P.R. David, and R.C. Tozer, “Low noise visible-blind UV avalanche photodiodes with edge terminated by 2° positive bevel,” *Elect. Lett.*, vol. 38, pp. 335-336, 2002.

[2] F.Yan, C.Qin, J.H.Zhao, and M.Weiner, “Novel Technology for the Formation of a Very Small Bevel Angle for Edge Termination,” *Materials Science Forum*, vol. 389-393, pp. 1305-1308, 2002.

[3] *Wide Bandgap Semiconductors; Growth, Processing and Applications.* New Jersey: Noyes, 2000. p.172. Editor Stephen Pearton.

[4] *Process Technology for Silicon Carbide Devices.* London: INSPEC, 2002. Editor Carl-Mikael Zetterling.

[5] H.H. Berger, *Solid-State Electron*. vol. 15, p.145 1972.

[6] B.J. Johnson, M.A. Capano, “Mechanism of ohmic behavior of Al/Ti *contacts* to p-type 4H-*SiC* after annealing,” J. Appl. Phy., vol. 95 n. 10, pp.5616-20, 15 May 2004.

[7] S.K. Lee, C.M. Zetterling, M. Ostling, J.P. Palmquist, H. Hogberg, and U. Jansson, “Low resistivity ohmic titanium carbide contacts to n- and p-type 4H-silicon carbide,” *Solid-State Electron*, vol. 44, pp. 1179-86, 2000.

[8] L.G. Fursin, J.H. Zhao, M. Weiner, “Nickel Ohmic contacts to p- and n-type 4H-SiC,” *Electron. Lett.,* vol. 37 n. 17, 16 August 2001.

[9] Xiangyi Guo, *High Performance Ultraviolet 4H-SiC Avalanche Photodiodes*. Dissertation. University of Texas at Austin, 2005.

[10] S. Tsukimoto, K. Nitta, T. Sakai, M. Moriyama, and M. Murakami, “Correlation between the Electrical Properties and the Interfacial Microstructures of TiAl-Based Ohmic Contacts to p-Type 4H-SiC,” *J. Electron. Mat.*, vol. 33 n. 5, pp.460-6, 2004.

[11] X. Guo, A. Beck, X. Li, J.C. Campbell, D. Emerson, and J. Sumakeris, “Study of Reverse Dark Current in 4H-SiC Avalanche Photodiodes,” IEEE J. Quant. Electron., vol. 41 n.4, pp.562-7, April 2005.

[12] X. Guo, A. Beck, B. Yang, and J.C. Campbell, “Low dark current 4H-SiC avalanche photodiodes,” *Electron. Lett.,* vol. 39 n. 23, 13 November 2003.

[13] S. Wang, R. Sidhu, F. Ma, X.W. Li, X.G. Zheng, J.B. Hurst, X.G. Sun, N. Li, A.L. Holmes, and J.C. Campbell, “A study of low-bias photocurrent gradient of avalanche photodiodes,” *IEEE Trans. Electron Devices*, vol.49 n.12, pp. 2107-2113, 2002.

[14] X. Guo, A. Beck, X. Li, J.C. Campbell, D. Emerson, and J. Sumakeris, “Spatial Nonuniformity of 4H-SiC Avalanche Photodiodes at High Gain,” IEEE J. of Quant. Electron., vol. 41 n. 10, pp. 1213-6, October 2005.

Chapter 6

[1] B. Jayant Baliga, *Power Semiconductor Devices* (PWS Publishing Company, Boston, 1995).

[2] R.L. Davies and F.E. Gentry, “Control of Electric Field at the Surface of P-N Junctions,” *IEEE Trans. Electron Devices*, vol. ED-11, pp. 313-323, 1964.

[3] A.R. Powell, J.J. Sumakeris, R.T. Leonard, M.F. Brady, St.G. Muller, V.F. Tsvertkov, H.McD. Hobgood, A.A. Burk, M.J. Paisley, R.C. Galss, and C.H. Carter, Jr., “Status of 4H-SiC Substrate and Epitaxial Materials for Commercial Power Applications,” *Mat. Res. Soc. Proc.*, vol. 815 pp.3-14, 2004.

[4] S.R. Cho, S.K. Yang, J.S. Ma, S.D. Lee, J.S.Yu, A.G. Choo, T.I. Kim, and J. Burm, “Suppression of avalanche multiplication at the periphery of diffused junction by floating guard rings in a planar InGaAs-InP avalanche photodiode,” Photonics Tech. Lett., vol. 12 n. 5, pp.534-6, May 2000.

[5] Victor A.K. Temple and W. Tantraporn, “Junction Termination Extension for Near-Ideal Breakdown Voltage in p-n Junctions,” *IEEE Trans. Electron Devices*, vol. ED-33 n. 10, pp.1601-08, October 1986.

[6] X. Li, K. Tone, L. Fursin, J.H. Zhao, T. Burke, P. Alexandrov, M. Pan, and M. Weiner, “Multistep junction termination extension for SiC power devices,” *Elect. Lett.* vol. 37 n. 6, pp. 392-3, 15 March 2001.

[7] F. Yan, C. Qin, J.H. Zhao, M. Weiner, B.K. Ng, J.P.R. David, and R.C. Tozer, “Low noise visible-blind UV avalanche photodiodes with edge terminated by 2° positive bevel,” *Elect. Lett*., vol. 38, pp. 335-336, 2002.

[8] Y. Choi, and W. Kwan, “On the surface electric field of junction diodes with a tapered window,” *Solid-State Elec*., vol. 30 n. 3, pp. 353-360, 1987.

[9] F. Yan, C. Qin, J.H. Zhao, and M. Weiner, “Novel Technology for the Formation of a Very Small Bevel Angle for Edge Termination,” *Materials Science Forum*, vol. 389-393, pp. 1305-1308, 2002.

[10] X. Guo, A. L. Beck, J. C. Campbell, D. Emerson, and J. Sumakeris, “Spatial Nonuniformity of 4H-SiC Avalanche Photodiodes at High Gain,” *IEEE J. Quant. Electron.*, vol. 41 n. 10, pp.1213-16, October 2005.

[11] A.R. Powell and L.B. Rowland, “SiC materials-progress, status, and potential roadblocks,” *Proceedings of IEEE*, vol. 90 n. 6, pp.942-955, 2002.

[12] Xiangyi Guo, *High Performance Ultraviolet 4H-SiC Avalanche Photodiodes*. Dissertation. University of Texas at Austin, 2005.

Chapter 7

[1] F.Yan, C.Qin, J.H.Zhao, M.Weiner, B.K.Ng, J.P.R.David, and R.C.Tozer, “Low-noise visible-blind UV avalanche photodiodes with edge terminated by 2° positive bevel,” *Electon. Lett*., vol. 38, pp. 335-336, 2002.

[2] Goldberg Yu.A. *Handbook Series on Semiconductor Parameters*, vol.1, World Scientific, London, 1996, pp. 104-124.

[3] X. Guo, A. Beck, X. Li, J.C. Campbell, D. Emerson, and J. Sumakeris, “Study of Reverse Dark Current in 4H-SiC Avalanche Photodiodes,” *IEEE J. Quant. Electron*., vol. 41 n.4, pp.562-7, April 2005.

[4] Gauri Karve. *Avalanche Photodiodes as Single Photon Detectors*. Dissertation. University of Texas at Austin, 2005.

[5] D.S. Bethune and W.P. Risk. "An Autocompensating Fiber-Optic Quantum Cryptography System Based on Polarization Splitting of Light," *IEEE J. Quantum Electron*, vol. 36 n. 3, pp. 340-347, March 2000.

[6] G. Karve, X.G. Zheng, X. Zhang, X. Li, N. Li, S. Wang, F. Ma, A. Holmes. Jr., J.C. Campbell, G.S. Kinsey, J.C. Boisvert, T.D. Isshiki, R. Sudaharsanan, D.S. Bethune, W.P. Risk, "Gieger Mode Operation of an $In_{0.53}Ga_{0.47}As$ – $In_{0.52}Al_{0.48}As$ Avalanche Photodiode," IEEE J. Qunatum Electron., vol.39, n.10, pp.1281-1286, October 2003.

[7] A. Karlsson, M. Bourennane, G. Ribordy, H. Zbinden, J. Brendel, J. Rarity, and P. Tapster, "A Single-Photon Counter for Long-Haul Telecom," IEEE Circuits and Devices, vol.15 n.6, pp.34-40, November 1999.

[8] J.S. Ng, C.H. Tan, and J.P.R. David, "A comparison of avalanche breakdown probabilities in semiconductor materials," *J. Modern Optics,* vol. 51 n. 9-10, pp.1351-1321, 15 June- 10 July 2004.

[9] Discussions with Dr. Feng Ma.

[10] S. Cova, M. Ghioni, A. Lacaita, C. Samori, and F. Zappa, "Avalanche photodiodes and quenching circuits fro single-photon detection," Appl. Optics, vol. 35 n. 12, pp.1956-1958, 20 April 1996.

[11] Y. Kang, H.X. Lu, Y.H. Lo, D.S. Bethune, and W.P. Risk, "Dark count probability and quantum efficiency of avalanche photodiodes for single-photon detection," *Appl. Phys. Lett.* vol.83 n. 14, 6 October 2003.

[12] A. Lacaita, M. Mastrapasqua, M. Ghioni, and S. Vanoli, "Observation of avalanche propagation by multiplication assisted diffusion in p-n junctions," *Appl. Phys. Lett.,* vol. 57 n. 5, 30 July 1990.

[13] B. Jayant Baliga, *Power Semiconductor Devices* (PWS Publishing Company, Boston, 1995).

[14] S. Verghese, K.A. McIntosh, R.J. Molnar, L.J. Mahoney, R.L. Aggarwal, M.W. Geis, K.M. Molvar, E.K. Duerr, and I. MeIngailis, "GaN Avalanche Photodiodes Operating in Linear-Gain Mode and Geiger Mode," *IEEE Trans. Electron Devices*, vol. 48 n.3, pp.502-11, March 2001.

[15] H. Dautet, P. Deschamps, B. Dion, A.D. MacGregor, D. MacSween, R.J. McIntyre, C. Trottier, and P.P. Webb, "Photon counting techniques with silicon avalanche photodiodes," Appl. Opt., vol.32 n.21, pp. 1281-1286, October 2003.

[16] X. Xin, F. Yan, X. Sun, P. Alexandrove, C.M. Stahle, J. Hu, M. Matsumura, X. Li, M. Weiner, and H.J. Zhao, "Demonstration of 4H-SiC UV single photon counting avalanche photodiodes," *Electron. Lett.*, vol. 41 n. 4, 17 February 2005.

[17] K.A. McIntosh, R.J. Molnar L.J. Mahoney, K.M. Molvar, N. Efremow, Jr., and S. Verghese, "Ultraviolet photon counting with GaN avalanche phtodiodes," *Appl. Phys. Lett.*, vol. 76 n. 26, pp. 3938-40, 26 June 2000.

Chapter 8

[1] X. Guo, A. Beck, X. Li, J.C. Campbell, D. Emerson, and J. Sumakeris, "Study of Reverse Dark Current in 4H-SiC Avalanche Photodiodes," *IEEE J. Quant. Electron.*, vol. 41 n.4, pp.562-7, April 2005.

[2] S. Wang, F. Ma, X. Li, G. Karve, X. Zheng, and J.C. Campbell, "Analysis of breakdown probabilities in avalanche photodiodes using a history-dependent analytical model," *Appl. Phy. Lett.* vol. 82 n. 12, pp. 1971-3, 24 March 2003.

[3] J.S. Ng, C.H. Tan, and J.P.R. David, "A comparison of avalanche breakdown probabilities in semiconductor materials," *J. Modern Optics,* vol. 51 n. 9-10, pp.1351-1321, 15 June- 10 July 2004.

[4] F.Yan, C.Qin, J.H.Zhao, M.Weiner, B.K.Ng, J.P.R.David, and R.C.Tozer, "Low-noise visible-blind UV avalanche photodiodes with edge terminated by 2° positive bevel," *Electon. Lett.*, vol. 38, pp. 335-336, 2002.

[5] S. Cova, M. Ghioni, A. Lacaita, C. Samori, and F. Zappa, "Avalanche photodiodes and quenching circuits fro single-photon detection," Appl. Optics, vol. 35 n. 12, pp.1956-1958, 20 April 1996.

[6] D.S. Bethune and W.P. Risk, "An Autocompensating Fiber-Optic Quantum Cryptography System Based on Polarization Splitting of Light," *IEEE J. Quantum Electron*, vol. 36 n. 3, pp. 340-347, March 2000.

[7] S. Verghese, K.A. McIntosh, R.J. Molnar, L.J. Mahoney, R.L. Aggarwal, M.W. Geis, K.M. Molvar, E.K. Duerr, and I. MeIngailis, "GaN Avalanche Photodiodes Operating in Linear-Gain Mode and Geiger Mode," *IEEE Trans. Electron Devices*, vol. 48 n.3, pp.502-11, March 2001.

[8] Y. Kang, H.X. Lu, Y.H. Lo, D.S. Bethune, and W.P. Risk, “Dark count probability and quantum efficiency of avalanche photodiodes for single-photon detection,” *Appl. Phys. Lett.* vol.83 n. 14, 6 October 2003.

[9] X. Xin, F. Yan, X. Sun, P. Alexandrove, C.M. Stahle, J. Hu, M. Matsumura, X. Li, M. Weiner, and H.J. Zhao, “Demonstration of 4H-SiC UV single photon counting avalanche photodiodes,” *Electron. Lett.*, vol. 41 n. 4, 17 February 2005.

[10] K.A. McIntosh, R.J. Molnar L.J. Mahoney, K.M. Molvar, N. Efremow, Jr., and S. Verghese, “Ultraviolet photon counting with GaN avalanche phtodiodes,” *Appl. Phys. Lett.*, vol. 76 n. 26, pp. 3938-40, 26 June 2000.

Publications

[1] Xiangyi Guo, L.B. Rowland, G.T. Dunne, J.A. Fronheiser, P.M. Sandvik, A.L. Beck, J.C. Campbell, “Demonstration of ultraviolet separate absorption and multiplication 4H-SiC avalanche photodiodes,” IEEE Photonics Technology Letters, vol.18 n.1, pp. 136-8, Jan. 2006.

[2] X. Guo, A.L. Beck, J.C. Campbell, D. Emerson, and J. Sumakeris, “Spatial Nonuniformity of 4H-SiC Avalanche Photodiodes at High Gain,” IEEE J. Quant. Elec., v.41 n.10, p. 1213-6 October 2005.

[3] A.L. Beck, G. Karve, S. Wang, J. Ming, X. Guo, and J.C. Campbell, “Geiger Mode Operation of Ultraviolet 4H-SiC Avalanche Photodiodes,” IEEE Photonics Tech. Lett., v.17 n.7 p.1507-9, July 2005.

[4] Xiangyi Guo; A.L.Beck, Xiaowei Li, J.C. Campbell, “Study of reverse dark current in 4H-SiC avalanche photodiodes,” IEEE J. Quant. Elec., v.41, n.4, p. 562-7, April 2005.

[5] A.L. Beck, B. Yang, S. Wang, C.J. Collins, J.C. Campbell, A. Yulius, A. Chen, J.M. Woodall, “Quasi-direct UV/Blue GaP Avalanche Photodetectors.” IEEE J. Quant. Elec., v.40 n.12 p.1695-9, December 2004.

[6] J. C. Campbell, S. Demiguel, F. Ma, A. Beck, X. Guo, S. Wang, X. Zheng, X. Li, J. D. Beck, M. A. Kinch, A. Huntington, L. A. Coldren, J. Decobert, N. Tscherptner, " Recent Adancec in Avalanche photodiodes, " IEEE Journal of Selected Topics in Quantum Electronics. v.10, n.4, pp. 777-787, Jul/Aug 2004.

[7] Ariane L. Beck, Bo Yang, Xiangyi Guo, Joe C. Campbell, “Edge Breakdown in 4h-SiC Avalanche Photodiodes,” IEEE J. Quant. Elec., v.40 n.3 p.321-4, March 2004.

[8] Xiangyi Guo; Beck, A.; Bo Yang; Campbell, J.C., “Low dark current 4H-SiC avalanche photodiodes,” Lasers and Electro-Optics Society, 2003: LEOS 2003, The 16th Annual Meeting of the IEEE , v2 pp. 851-852 (2003).

[9] Campbell, J.C.; Shuling Wang; Xiaoguang Zheng; Xiaowei Li; Ning Li; Feng Ma; Xiaoguang Sun; Collins, C.J.; Beck, A.L.; Yang, B.; Hurst, J.B.; Sidhu, R.; Holmes, A.L., Jr.; Chowdhury, U.; Wong, M.M.; Dupuis, R.D.; Huntington, A.; Coldren, L.A.; Zhonghui Chen; Eui-Tae Kim; Madhukar, A., "Photodetectors: UV to IR," *Proceedings of the SPIE - The International Society for Optical Engineering*, Active and Passive Optical Components for WDM Communications III, v.524, p.375 (2003).

[10] Yanning Sun; Campbell, J.C.; Shuling Wang; Beck, A.L.; An Chen; Yulius, A.; Woodall, J.M., "Drift dominated InP photodetectors with high quantum efficiency," International Conference on Indium Phosphide and Related Materials, p.502 (2003).

[11] Xiangyi Guo; Beck, A.; Bo Yang; Campbell, J.C., "Low dark current 4H-SiC avalanche photodiodes," Electronics Letters, v 39, n23 pp.1673-4, Nov. 2003.

[12] Collins, C.J.; Chowdhury, U.; Wong, M.M.; Yang, B.; Beck, A.L.; Dupuis, R.D.; Campbell, J.C., "Improved solar-blind external quantum efficiency of back-illuminated $Al_xGa_{1-x}N$ heterojunction pin photodiodes," *Elec. Lett.* v.38 p. 824 (2002).

[13] Beck, A.L.; Collins, C.J.; Wang, S.; Yang, B.; Campbell, J.C.; Yulius, A.; Chen, A.; Woodall, J.M., "UV/blue gap avalanche photodiodes," *Lasers and Electro-Optics Society, 2002. LEOS 2002. The 15th Annual Meeting of the IEEE* , v.2 pp.837-8(2002).

[14] Collins, C.J.; Chowdhury, U.; Wong, M.M.; Yang, B.; Beck, A.L.; Dupuis, R.D.; Campbell, J.C., "Improved solar-blind detectivity using an $Al_xGa_{1-x}N$ heterojunction p-i-n photodiode," *Appl. Phy. Lett.* v. 80 p.3754 (2002).

[15] Chowdhury, U.; Wong, M.M.; Collins, C.J.; Yang, B.; Zhu, T.G.; Beck, A.L.; Campbell, J.C.; Dupuis, R.D., "High quantum efficiency AlGaN/GaN solar-blind photodetectors grown by metalorganic chemical vapor deposition," GaN and Related Alloys – 2001, p. 817 (2002).

[16] Li, T.; Lambert, D.J.H.; Beck, A.L.; Collins, C.J.; Yang, B.; Wong, M.M.; Chowdhury, U.; Dupuis, R.D.; Campbell, J.C., "Low-noise solar-blind $Al_xGa_{1-x}N$-based metal-semiconductor-metal ultraviolet photodetectors," *J. Elec. Materials*, v.30 p.872 (2001).

[17] Ting Li; Lambert, D.J.H.; Wong, M.M.; Collins, C.J.; Yang, B.; Beck, A.L.; Chowdhury, U.; R.Dupuis, R.D.; Campbell, J.C., "Low-noise back-illuminated $Al_xGa_{1-x}N$-based p-i-n solar-blind ultraviolet photodetectors," *IEEE J. Quantum Electronics*, v.37 p.538 **(**2001).

[18] Campbell, J.C.; Collins, C.J.; Wong, M.M.; Chowdhury, U.; Beck, A.L.; Dupuis, R.D., "High quantum efficiency at low bias $Al_xGa_{1-x}N$ p-i-n photodiodes," *Physica Status Solidi A*, Fourth International Conference on Nitride Semiconductors, v. 188 p.282 (2001).

[19] Ting Li; Lambert, D.J.H.; Beck, A.L.; Collins, C.J.; Yang, B.; Wong, M.M.; Chowdhury, U.; Dupuis, R.D.; Campbell, J.C., "Solar-blind $Al_xGa_{1-x}N$-based metal-semiconductor-metal ultraviolet photodetectors," *Elec. Lett.* v. 36 p.1581 (2000).

[20] Carrano, J.C.; Lambert, D.J.H.; Eiting, C.J.; Collins, C.J.; Li, T.; Wang, S.; Yang, B.; Beck, A.L.; Dupuis, R.D.; Campbell, J.C., "GaN avalanche photodiodes," *Appl. Phy. Lett.* v.76 p.924 (2000).

[21] Lambert, D.J.H.; Yang, B.; Li, T.; Collins, C.J.; Wong, M.M.; Chowdhury, U.; Shelton, B.S.; Beck, A.L.; Campbell, J.C.; Dupuis, R.D., "High-performance back-illuminated solar-blind AlGaN metal-semiconductor-metal photodetectors," *2000 IEEE International Symposium on Compound Semiconductors Proceedings of the IEEE Twenty-Seventh International Symposium on Compound Semiconductors,* p.525 (2000)

[22] Collins, C.J.; Li, T.; Lambert, D.J.; Wong, M.M.; Yang, B.; Beck, A.L.; Dupuis, R.D.; Campbell, J.C., "Back illuminated solar-blind photodetectors," *LEOS 2000*, 2000 IEEE Annual Meeting Conference Proceedings, p.84 (2000).

[23] Campbell, J.C.; Li, T.; Wang, S.; Beck, A.L.; Collins, C.J.; Yang, B.; Lambert, D.J.H.; Dupuis, R.D.; Carrano, J.C.; Schurman, M.J.; Ferguson, I.T., "AlGaN/GaN ultraviolet photodetectors," *Proceedings of the SPIE - The International Society for Optical Engineering*, Photonics for Space Environments VII, v.4134, p.124 (2000).

[24] Ting Li; Shuling Wang; Beck, A.L.; Collins, C.J.; Bo Yang; Dupuis, R.D.; Carrano, J.C.; Schurman, M.J.; Ferguson, I.A.; Campbell, J.C., "High quantum efficiency Al_xGa_{1-x}/GaN-based ultraviolet p-i-n photodetectors with a recessed window structure," *Proceedings of the SPIE - The International Society for Optical Engineering*, Photodetectors: Materials and Devices V, v.3948 p.304 (2000).

[25] Carrano, J.C.; Ting Li; Collins, C.; Beck, A.L.; Shuling Wang; Bo Yang; Lambert, D.J.H.; Eiting, J.; Dupuis, D.; Campbell, J.C.; Wraback, M.; Shen, H.P.; Schurman, M.J.; Ferguson, I.T, "High-performance GaN/AlGaN-based ultraviolet photodetectors," *Proceedings of the SPIE - The International Society for Optical Engineering*, Photodetectors: Materials and Devices V, v. 3948 p.250 (2000).

[26] Li, T.; Beck, A.L.; Collins, C.; Dupuis, R.D.; Campbell, J.C.; Carrano, J.C.; Schurman, M.J.; Ferguson, I.A., "Improved ultraviolet quantum efficiency using a

semitransparent recessed window AlGaN/GaN heterojunction p-i-n photodiode," *Appl. Phy. Lett.* v.75 p.2421 (1999).

[27] Collins, C.J.; Li, T.A.; Beck, A.L.; Dupuis, R.D.; Campbell, J.C.; Carrano, J.C.; Schurman, M.J.; Ferguson, I.A., "Improved device performance using a semi-transparent p-contact AlGaN/GaN heterojunction positive-intrinsic-negative photodiode," *Appl. Phy. Lett.* v.75 p.2138 (1999).

[28] Collins, C.J.; Li, T.; Beck, A.L.; Dupuis, R.D.; Campbell, J.C.; Carrano, J.C.; Schurman, M.J.; Ferguson, I.A., "Improved device performance using a semi-transparent p-contact AlGaN/GaN heterojunction p-i-n photodiode," *1999 IEEE LEOS Annual Meeting Conference Proceedings. LEOS'99. 12th Annual Meeting*, p.681 (1999).

[29] Carrarro, J.C.; Li, T.; Beck, A.L.; Collins, C.; Dupuis, R.D.; Campbell, J.C.; Schurman, M.J.; Ferguson, I.A., "Improved ultraviolet quantum efficiency using a transparent recessed window AlGaN/GaN heterojunction p-i-n photodiode," *International Electron Devices Meeting 1999. Technical Digest*, p.587 (1999).

Vita

Ariane Laura Beck was born in Houston, Texas, on January 16th, 1979 to Edward (January 22, 1944 - November 29, 2000) and Beverly Beck. After completing her work at Blue Valley Northwest High School, Overland Park, Kansas, in 1997, she entered the University of Texas at Austin. While at the University of Texas, she worked as an Undergraduate Research Assistant and received her Bachelor of Science in 2000. She entered the graduate degree program at the University of Texas in September 2000 and received her Master of Science in December 2002. She and her husband, Eric Sebesta, live in Austin, Texas, where she is currently pursuing research in SiC ultraviolet single photon counting detectors for her PhD in Electrical Engineering.

Permanent Address: 404 Rio Grande #30
Austin, Texas 78701

This dissertation was typed by the author.